

Cavity QED with Single Trapped Ca^+ -Ions

Dissertation

zur Erlangung des Doktorgrades an der
naturwissenschaftlichen Fakultät
der Leopold-Franzens-Universität Innsbruck

vorgelegt von

Andreas Burghard Mundt

durchgeführt am Institut für Experimentalphysik
unter der Leitung von
o. Univ. Prof. Dr. R. Blatt

Innsbruck
Feber 2003

Abstract

This thesis reports on the design and setup of a vacuum apparatus allowing the investigation of cavity QED effects with single trapped $^{40}\text{Ca}^+$ ions. The weak coupling of ion and cavity in the ‘bad cavity limit’ may serve to inter-convert stationary and flying qubits.

The ion is confined in a miniaturised Paul trap and cooled via the Doppler effect to the Lamb–Dicke regime. The extent of the atomic wave function is less than 30 nm. The ion is enclosed by a high finesse optical cavity. The technically-involved apparatus allows movement of the trap relative to the cavity and the trapped ion can be placed at any position in the standing wave. By means of a transfer lock the cavity can be resonantly stabilised with the $S_{1/2} \leftrightarrow D_{5/2}$ quadrupole transition at 729 nm (suitable as a qubit) without light at that wavelength being present in the cavity.

The coupling of the cavity field to the $S_{1/2} \leftrightarrow D_{5/2}$ quadrupole transition is investigated with various techniques in order to determine the spatial dependence as well as the temporal dynamics. The orthogonal coupling of carrier and first-order sideband transitions at field nodes and antinodes is explored. The coherent interaction of the ion and the cavity field is confirmed by exciting Rabi oscillations with short resonant pulses injected into the cavity. Finally, first experimental steps towards the observation of cavity enhanced spontaneous emission have been taken.

Zusammenfassung

Diese Arbeit beschreibt die Konstruktion und den Aufbau einer Vakuum Apparatur zur Erforschung von ‘cavity QED’ Effekten mit einzelnen gefangenen $^{40}\text{Ca}^+$ Ionen. Die schwache Kopplung zwischen Ion und Resonatormode (‘bad cavity limit’) kann zur Übertragung von Quanteninformation von stationären auf transportable ‘Quanten-Bits’ genutzt werden.

Das Ion wird in einer miniaturisierten Paul Falle gespeichert und in das Lamb-Dicke Regime gekühlt, die Ausdehnung seiner Wellenfunktion beträgt weniger als 30 nm. Es ist von einem optischen Resonator hoher Güte umgeben und kann an beliebigem Ort in der stehenden Welle positioniert werden. Mithilfe einer Transfer-Stabilisierung kann die Resonanzfrequenz des Resonators auf den als Quanten-Bit geeigneten $S_{1/2} \leftrightarrow D_{5/2}$ Quadrupol-Übergang bei 729 nm stabilisiert werden, ohne dass Licht dieser Wellenlänge im Resonator selbst präsent ist.

Die räumliche und zeitliche Abhängigkeit der Kopplung des Resonatorfeldes an den $S_{1/2} \leftrightarrow D_{5/2}$ Quadrupol-Übergang wurde mit verschiedenen Techniken untersucht. Kohärente Kopplung zwischen Ion und Resonatorfeld wurde nachgewiesen, indem Rabi Oszillationen mit dem angeregten Resonatorfeld getrieben wurden. Letztendlich wurden erste vorläufige Schritte zur Beobachtung der durch den Resonator hervorgerufenen verstärkten spontanen Emission unternommen.

Contents

1	Introduction	1
2	Cavity QED	5
2.1	Theory	5
2.1.1	Cavity–Trapped–Atom Model	5
2.1.2	Model with Dissipation	15
2.2	Experiments on Cavity QED	18
2.2.1	Historic Overview	18
2.2.2	Cavity QED Experiments in Perspective	19
3	Realisation of the Model	21
3.1	Ca ⁺ –Ion as Quantum Mechanical System	21
3.1.1	Ca ⁺ Level Scheme and Relevant Transitions	21
3.1.2	Zeeman Splitting	23
3.2	Paul Traps	26
3.2.1	General Principle	26
3.2.2	Spherical Single Ion Trap	29
3.3	Optical Resonators	30
3.3.1	Cavity Lifetime τ and Finesse \mathcal{F}	30
3.3.2	Cavity Waist w_0 and Cavity Mode Volume	31
3.4	Realised Composite System	33
3.4.1	Strong Coupling	34
3.4.2	Weak Coupling	35
4	Experimental Setup	37
4.1	Overview	37
4.2	Cavity QED Ion Trap Apparatus	40
4.2.1	Vacuum Vessel	45
4.2.2	Maneuverable Paul Trap	45
4.2.3	Electrical Connections	46
4.2.4	Cavity Mount and Cavity	46

4.2.5	Beam Directions and Magnetic Field	48
4.3	Transfer Diode Laser	51
4.3.1	Setup	52
4.3.2	Linewidth of the Laser at 785 nm	54
4.4	Cavity Stabilisation	55
4.4.1	Setup	56
4.4.2	Establishing the Transfer Lock	57
5	Preparations for Single Ion Cavity QED	59
5.1	General Procedure of the Experiments	59
5.1.1	Preparation of a Single Ion	60
5.1.2	Pulsed Spectroscopy	61
5.2	Excitation with a Propagating Laser Beam	62
5.2.1	Spectral Components of the $S_{1/2} \leftrightarrow D_{5/2}$ Transition	62
5.2.2	Coherent Dynamics	65
5.2.3	Determination of the Vibrational State	67
6	Experiments on Ion–Cavity Coupling	71
6.1	Cavity–Scanning Technique	71
6.1.1	Temporal Variations of the Intracavity Field	72
6.1.2	Spatial Variations of the Intracavity Field	76
6.1.3	Coupling of Motional States	82
6.2	Frequency Stabilised Cavity	84
6.2.1	Coherent Ion–Cavity Coupling	84
6.2.2	Towards Cavity Enhanced Spontaneous Emission	85
7	Summary and Outlook	87
A	Quadrupole Matrix Elements	91
B	Normalised Scanrate	93
C	Coupling a Qubit to an Optical Cavity	95
D	Coherent Ion–Cavity Coupling	101
	Bibliography	111

Chapter 1

Introduction

The interest in cavity quantum electrodynamics (CQED) comes from two different directions. First, it is interesting to explore the laws of nature and describe them using physical theories. Most of the power of physical theories emerges from their focus on the simplest possible building blocks, for example, the hydrogen atom as a representative constituent of matter or the plane electro-magnetic wave as the simplest nontrivial solution to the Maxwell equations in free space. Having understood quantitatively relative simple units, the basic constituents can be combined and these may then interact, and this interaction may lead to new phenomena worth exploring. The subject of cavity quantum electrodynamics concerns the interaction of atoms with a single quantised mode of the radiation field. The basic theory (for a single atom) was developed in 1963 by Jaynes and Cummings [1] and complemented by Stehle [2] and Barton [3] in 1970. Since then a huge amount of theoretical as well as experimental work has been added to the subject as listed and discussed in chapter (2) section (2.2). Nevertheless, none of the known experiments in the optical regime allows deterministic control of the position of a single atom to an accuracy of much less than the radiation field wavelength and to couple coherently to the cavity mode. Hence it is a challenge to set-up an apparatus which allows cavity QED experiments to be performed where the position of a single atom can be freely chosen in the cavity mode.

A second and rather different motivation combining ion traps with high finesse cavities emerges from the modern field of quantum computation. As discussed by DiVincenzo [4], there are several requirements for the physical implementation of quantum computation:

- A scalable physical system with well characterised quantum bits (qubits)

- The ability to initialise the state of the qubits to a simple fiducial state, such as $|000\dots\rangle$
- Long relevant decoherence times, much longer than the gate operation
- A "universal" set of quantum gates
- A qubit-specific measurement capability

For quantum computation alone, these five requirements suffice. But as pointed out by DiVincenzo in [4], ‘the advantages of quantum information processing are not manifest solely, or perhaps even principally, for straightforward computation only’. To fully unfold the power of quantum information processing two further commandments have to be added:

- The ability to inter-convert stationary and flying qubits
- The ability to faithfully transmit flying qubits between specified locations

Whereas the research and development in fulfilling the first five requirements is very active, only minor experimental work has so far addressed the issue of inter-converting stationary and flying qubits.

One of the candidates for the realisation of a quantum computer (and therefore for the realisation of the first five requirements) are ion strings in traps [5]. The quantum information can be stored in long-lived internal states of the individual ions, e.g. by encoding a qubit of information within the coherent superposition of the $S_{1/2}$ ground state and the metastable $D_{5/2}$ excited state of $^{40}\text{Ca}^+$ [6]. One way to fulfill the last two demands, especially in transferring the stationary quantum information to a suitable flying qubit, is the coupling of the qubit transition to a cavity field mode. With this technique the stationary quantum information stored in the ion can be transferred to photons serving as flying qubits. The photons can be coupled into fibres allowing fast and reliable transport over long distances, thereby fulfilling the last of DiVincenzo’s requirements. Such an interface is the basic building block for distributed quantum networks and has many applications [7]. It requires the controlled coherent interaction of a single cavity mode and a single ion, the investigation of which forms the basis of this report.

The work detailed in this thesis is a contribution to the physical implementation of coherent quantum information transfer from a stationary qubit to a flying qubit. It is structured as follows: Chapter (2) develops the theory of a harmonically trapped two-level system coupled to a single electro-magnetic field mode. After consideration of the lossless model, dissipation is taken into account. It focuses on the parts of the theory important

for this work and which are not discussed in earlier theses [8, 9, 10, 11, 12]. The chapter closes with a short overview on cavity QED experiments performed so far by other groups and thereby demonstrates the role this experiment plays within the wider field of cavity QED research as a whole. Chapter (3) discusses the experimental realisation of the theoretical model by coupling the $S_{1/2} \leftrightarrow D_{5/2}$ quadrupole transition at 729 nm in a $^{40}\text{Ca}^+$ ion to a high finesse optical cavity. Chapter (4) describes the experimental setup, i.e. the necessary laser sources as well as the vacuum apparatus. Special attention is devoted to the transfer lock that enables the cavity to be resonantly stabilised with the qubit transition without light being present in the cavity that is resonant with the ion. Chapter (5) treats the experimental procedures. Experiments are presented that characterise the cavity-trap apparatus and show coherent dynamics on the quadrupole transition, which are necessary for more advanced cavity QED experiments. The experiments on ion-cavity coupling are discussed in chapter (6). After exploring spatial as well as temporal variations of the cavity field using the single ion as a probe, the coupling of motional states is investigated. Finally, coherent cavity-ion coupling is demonstrated by driving Rabi oscillations with the cavity field and first experimental steps towards the observation of cavity enhanced spontaneous emission are taken. The thesis closes with a summary of the results and an outline of future prospects for the experiment.

Chapter 2

Cavity QED

One of the tools of physics that is used to obtain an insight into the laws of nature is the study of physical systems on a fundamental level. In quantum optics the interest is in the interaction of light with matter. Following the above recipe leads to an investigation of the basic entity of the electro-magnetic field i.e. a single field mode interacting with the basic entity of matter i.e. an atom. To make quantum effects dominant for both, light and matter, this must be carried out at the level of a few quanta.

2.1 Theory

2.1.1 Cavity–Trapped–Atom Model

Consider first the system composed of a two–level atom trapped in a harmonic potential interacting with a single mode of the electro–magnetic field. For the moment no coupling is assumed to be present. For the free cavity field the Hamiltonian H_c is given by:

$$H_c = \hbar\omega_c(b_c^\dagger b_c + \frac{1}{2}), \quad (2.1)$$

where b_c^\dagger and b_c are the photon creation and annihilation operators respectively, obeying the relations:

$$\begin{aligned} [b_c, b_c^\dagger] &= 1, \\ b_c^\dagger |m_c\rangle &= \sqrt{m_c + 1} |m_c + 1\rangle, \\ b_c |m_c\rangle &= \sqrt{m_c} |m_c - 1\rangle, \end{aligned} \quad (2.2)$$

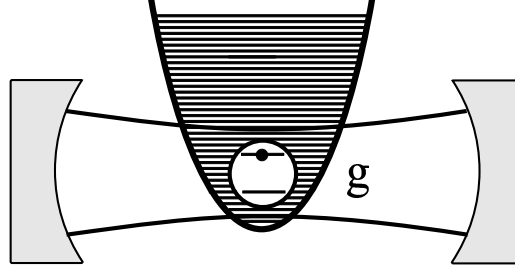


Figure 2.1: Scheme of a two-level system trapped in a harmonic potential interacting (coupling constant g) with a single electric field mode.

for the eigenstates $|m_c\rangle$, $m_c = 0, 1, 2, \dots$ of the Hamiltonian H_c . The Hamiltonian H_a for the two-level system is given by:

$$H_a = \frac{\hbar\omega_a}{2} \sigma_z, \quad (2.3)$$

where $\omega_a/(2\pi)$ is the frequency of the atomic transition and:

$$\sigma_z = \begin{pmatrix} 1 & 0 \\ 0 & -1 \end{pmatrix} \quad (2.4)$$

is one of the Pauli matrices.

The atom oscillating in its harmonic trapping potential is described by the same Hamiltonian as the free field but for reasonable potentials the vibration frequency ω_v will be much lower than the cavity resonance frequency ω_c ($\omega_v \ll \omega_c$). With the phonon creation and annihilation operators a_v^\dagger and a_v respectively, the Hamiltonian for the atom's vibrational motion can be written as:

$$H_v = \frac{p^2}{2M} + \frac{M\omega_v^2}{2}x^2 = \hbar\omega_v(a_v^\dagger a_v + \frac{1}{2}), \quad (2.5)$$

where M is the mass of the ion and the relations:

$$x = \sqrt{\frac{\hbar}{2M\omega_v}}(a_v + a_v^\dagger), \quad (2.6)$$

$$p = -i\sqrt{\frac{\hbar M\omega_v}{2}}(a_v - a_v^\dagger) \quad (2.7)$$

have been used. The annihilation and creation operators a_v and a_v^\dagger obey the corresponding relations to (2.2). The composite system is described by the sum of the individual Hamiltonians plus an interaction term H_1 . For the dynamics of interest here, the zero quantum energy leads to an overall phase but does not change the dynamics. From now on it is therefore omitted and the overall Hamiltonian is defined, without the zero quantum contribution in the cavity field and vibrational Hamiltonian, as:

$$H := \underbrace{\hbar\omega_c(b_c^\dagger b_c) + \frac{\hbar\omega_a}{2} \sigma_z + \hbar\omega_v(a_v^\dagger a_v)}_{=: H_0} + H_1. \quad (2.8)$$

Form of the Interaction Hamiltonian

The interaction of the atomic system with the electric light field can be expanded as a sum of interaction terms where the first non-vanishing term is the most relevant for the system. For the experimental system at hand this term is the electric quadrupole term given by [13]:

$$H_1 = \frac{e}{2} \sum_{i,j} r_i r_j \left(\frac{\partial E_i(x_1, x_2, x_3, t)}{\partial x_j} \right) \Big|_{\mathbf{x}}, \quad (2.9)$$

where $\mathbf{r} = (r_1, r_2, r_3)^T$ is the position vector of the valence electron relative to the atomic position $\mathbf{x} = (x_1, x_2, x_3)^T$ and the partial derivatives of the electric field are evaluated at the position of the atom. To calculate (2.9) the electric field must be known. For a Gaussian TEM₀₀ standing wave mode with waist radius w_0 and cavity length L the electric field operator \mathbf{E} near the cavity center can be taken as [10, 14]:

$$\mathbf{E}(x_1, x_2, x_3, t) = \mathbf{e} \sqrt{\frac{2\hbar\omega_c}{\epsilon_0 L \pi w_0^2}} (b_c^\dagger + b_c) e^{-\frac{\rho^2}{w_0^2}} \sin(\mathbf{k} \cdot \mathbf{x} + \phi), \quad (2.10)$$

where ρ is the radial distance from the cavity axis, ϵ_0 is the permittivity of free space and ϕ is a constant phase shift dependent on the atomic position in the standing wave. The polarisation unit vector \mathbf{e} has to be chosen perpendicular to \mathbf{k} . We assume the atom is at $\mathbf{x} = \mathbf{0}$, i.e. in the cavity center oscillating along \mathbf{k} . Inserting (2.10) in (2.9) we find:

$$H_1 = \frac{e}{2} \sqrt{\frac{2\hbar\omega_c}{\epsilon_0 L \pi w_0^2}} (b_c^\dagger + b_c) (\mathbf{r} \cdot \mathbf{e})(\mathbf{r} \cdot \mathbf{k}) \cos(\mathbf{k} \cdot \mathbf{x} + \phi). \quad (2.11)$$

To simplify (2.11) further, the matrix elements of $(\mathbf{r} \cdot \mathbf{e})(\mathbf{r} \cdot \mathbf{k})$ for the experimentally investigated $^{40}\text{Ca}^+$ quadrupole transition $S_{1/2}, m_j = -1/2 \leftrightarrow D_{5/2}, m_j = -5/2$ ($\lambda = 729$ nm) have to be calculated. Using the references [15] and [16] (see appendix A) the following result is obtained (the arbitrary phase is chosen to be zero, \mathbf{e} , \mathbf{k} and \mathbf{B} are assumed mutually orthogonal for maximal coupling):

$$\langle S_{1/2}, -1/2 | (\mathbf{r} \cdot \mathbf{e})(\mathbf{r} \cdot \mathbf{k}) | D_{5/2}, -5/2 \rangle = \frac{1}{e} \sqrt{\frac{5\gamma_{\perp} \epsilon_0 \lambda^3 \hbar}{2\pi^2}}. \quad (2.12)$$

Using the definitions:

$$|g\rangle := |S_{1/2}, -1/2\rangle, \quad (2.13)$$

$$|e\rangle := |D_{5/2}, -5/2\rangle, \quad (2.14)$$

$$\eta := k \sqrt{\frac{\hbar}{2M\omega_v}}, \quad (2.15)$$

and (2.6) we obtain:

$$H_1 = \hbar g (\sigma_+ + \sigma_-) (b_c^\dagger + b_c) \times \cos(\eta(a_v^\dagger + a_v) + \phi). \quad (2.16)$$

The coupling constant g includes the properties of the actual atomic transition (its transversal decay rate γ_{\perp}) and the properties of the cavity mode (L, w_0). Using (2.11) and (2.12), it is seen that:

$$g = \sqrt{\frac{5\gamma_{\perp} c \lambda^2}{2\pi^2 L w_0^2}}. \quad (2.17)$$

The position in the standing wave can be determined by the constant ϕ . From the identity: $\cos(\mathbf{k} \cdot \mathbf{x} + \phi) \equiv \cos(\mathbf{k} \cdot \mathbf{x}) \cos(\phi) - \sin(\mathbf{k} \cdot \mathbf{x}) \sin(\phi) \propto H_1$ we see that the interaction of the atom located at $\mathbf{x} = \mathbf{0}$ can always be decomposed in a part interacting with the antinode of the field ($\phi = \pi/2$, $H_1 \propto -\sin(\mathbf{k} \cdot \mathbf{x}) \Rightarrow \mathbf{E} \propto \cos(\mathbf{k} \cdot \mathbf{x})$) and a part interacting with the node ($\phi = 0$, $H_1 \propto \cos(\mathbf{k} \cdot \mathbf{x}) \Rightarrow \mathbf{E} \propto \sin(\mathbf{k} \cdot \mathbf{x})$). In the following both cases are therefore investigated separately.

In the experiment the ion is well cooled and resides in the Lamb–Dicke regime with a small Lamb–Dicke parameter η . Under this condition the higher orders of η can be neglected. The first non-vanishing terms are:

$$H_1 = \hbar g (\sigma_+ + \sigma_-) (b_c^\dagger + b_c) \times \begin{cases} 1 + \mathcal{O}(\eta^2), & \text{node} \\ -\eta(a_v^\dagger + a_v) + \mathcal{O}(\eta^3). & \text{antinode} \end{cases} \quad (2.18)$$

Transforming to the interaction picture and performing the rotating wave approximation (note: $\omega_v \ll \omega_c \approx \omega_a$) it follows that ($\Delta := \omega_c - \omega_a$):

$$\begin{aligned} \tilde{H}_I &:= e^{iH_0t/\hbar} H_1 e^{-iH_0t/\hbar} \\ &\simeq \hbar g \times \begin{cases} \{\sigma_+ b_c e^{-i\Delta t} + \sigma_- b_c^\dagger e^{i\Delta t} + \mathcal{O}(\eta^2)\}, & \text{node} \\ \{-\eta[\sigma_+ a_v^\dagger b_c e^{-i(\Delta-\omega_v)t} \\ + \sigma_- a_v^\dagger b_c^\dagger e^{i(\Delta+\omega_v)t} \\ + \sigma_+ a_v b_c e^{-i(\Delta+\omega_v)t} \\ + \sigma_- a_v b_c^\dagger e^{i(\Delta-\omega_v)t}] + \mathcal{O}(\eta^3)\}. & \text{antinode} \end{cases} \end{aligned} \quad (2.19)$$

Consider now the different terms in this approximation. In the node, where the $\mathcal{O}(\eta)$ terms are absent, the only coupling that exists is between states with the same vibrational quantum number ($n_v = \text{const.}$). These transitions are called ‘carrier transitions’. The $\sigma_+ b_c$ term represents the excitation of the atom by absorbing a cavity photon. $\sigma_- b_c^\dagger$ describes the emission into the cavity (see figure (2.2)). In the antinode, on the other hand, the contributing terms are of first order in η . From (2.19) it is seen that the only transitions allowed are transitions that change the vibrational quantum number by one ($\Delta n_v = \pm 1$). Transitions changing the vibrational quantum number n_v by ± 1 are called ‘first-order sideband transitions’.

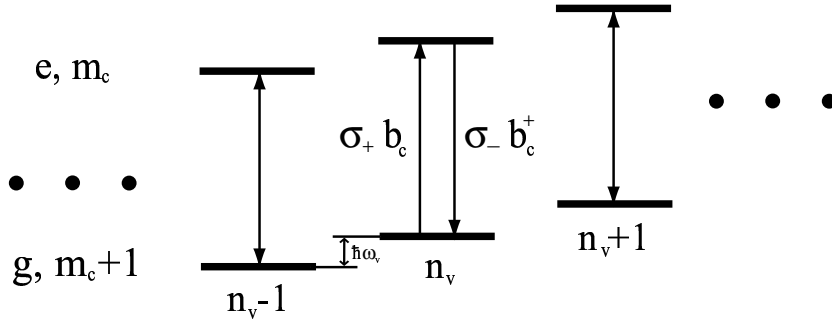


Figure 2.2: Visualisation of the energy states of the atom trapped in a harmonic potential. The atomic states $|g\rangle$ and $|e\rangle$ are dressed with the harmonic oscillator level structure. Carrier transitions ($\Delta n_v = 0$) are indicated by arrows. Starting with an arbitrary vibrational quantum number n_v , the dynamics of the system in a field node is restricted to the pair of levels keeping n_v constant.

The relevant terms are:

$\sigma_+ a_v b_c$: excitation of the atom and $\Delta n_v = -1$,
 $\sigma_- a_v^\dagger b_c^\dagger$: emission into the cavity and $\Delta n_v = +1$,
 (red sideband transitions, see figure (2.3));

$\sigma_+ a_v^\dagger b_c$: excitation of the atom and $\Delta n_v = +1$,
 $\sigma_- a_v b_c^\dagger$: emission into the cavity and $\Delta n_v = -1$,
 (blue sideband transitions, see figure (2.4)).

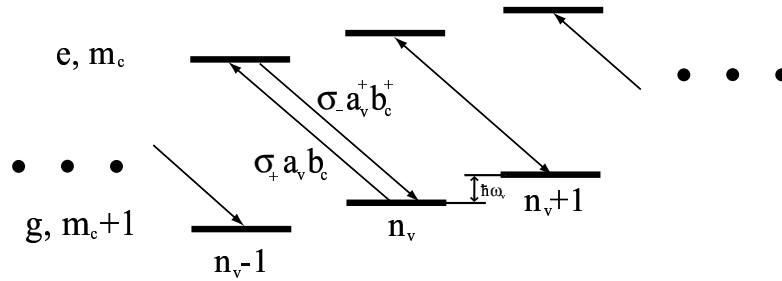


Figure 2.3: Visualisation of the states of the system involved in red sideband transitions (indicated by arrows). The dynamics of the system can be described by considering any pair of states $|e, n_v - 1, m_c\rangle$ and $|g, n_v, m_c + 1\rangle$, with arbitrary vibrational quantum number n_v and field quantum number m_c .

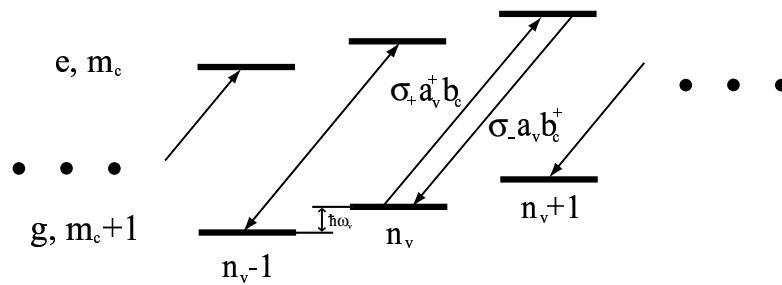


Figure 2.4: Visualisation of the states of the system involved in blue sideband transitions (indicated by arrows). The dynamics of the system can be described by considering any pair of states $|e, n_v + 1, m_c\rangle$ and $|g, n_v, m_c + 1\rangle$, with arbitrary vibrational quantum number n_v and field quantum number m_c .

Taking into account only the zeroth and first order in η terms, the main points are now summarised: **In the node coupling is to the carrier only: there is no coupling to the first-order vibrational sidebands. In the antinode only coupling to the first-order vibrational sidebands is present, so there is no excitation on the carrier.** By considering the full expansion of the harmonic functions, it is seen that in the node in general there is only coupling between states that differ by an even number of vibrational quanta ($\Delta n_v = 0, 2, 4, \dots$; carrier, second-order sidebands, fourth-order sidebands \dots), whereas in the antinode only coupling between states that differ by an odd number of vibrational quanta occurs ($\Delta n_v = 1, 3, 5, \dots$; first-order sidebands, third-order sidebands, \dots)¹.

Dynamics on the Carrier

In the node we have:

$$\tilde{H}_I \simeq \hbar g \times \{ \sigma_+ b_c e^{-i\Delta t} + \sigma_- b_c^\dagger e^{i\Delta t} + \mathcal{O}(\eta^2) \}. \quad (2.20)$$

If the terms of second order in η are neglected, \tilde{H}_I couples only states that differ in one cavity or atom excitation quantum. A choice of basis is: $\{|e, n_v, m_c\rangle, |g, n_v, m_c + 1\rangle\}$, where the vibrational quantum number n_v is the same for all states (only carrier transitions, cf. figure (2.2)). The dynamics of interest are:

$$|\psi(t)\rangle_I := e^{iH_0 t/\hbar} |\psi(t)\rangle = \tilde{C}_1(t) |e, n_v, m_c\rangle + \tilde{C}_2(t) |g, n_v, m_c + 1\rangle, \quad (2.21)$$

which is derived from:

$$i\hbar \frac{d}{dt} |\psi(t)\rangle_I = \tilde{H}_I |\psi(t)\rangle_I. \quad (2.22)$$

With the use of (2.2) the non-zero matrix elements are obtained:

$$\begin{aligned} \langle e, n_v, m_c | \sigma_+ b_c | g, n_v, m_c + 1 \rangle &= \langle g, n_v, m_c + 1 | \sigma_- b_c^\dagger | e, n_v, m_c \rangle \\ &= \sqrt{m_c + 1}, \end{aligned} \quad (2.23)$$

and for the matrix of \tilde{H}_I it is found:

$$\tilde{H}_I = \hbar g \begin{pmatrix} 0 & e^{-i\Delta t} \sqrt{m_c + 1} \\ e^{i\Delta t} \sqrt{m_c + 1} & 0 \end{pmatrix}. \quad (2.24)$$

¹For a dipole transition with $H_1 = e\mathbf{r} \cdot \mathbf{E}$, node and antinode are interchanged in their coupling character.

Equation (2.22) can now be written:

$$i\hbar \frac{d}{dt} \begin{pmatrix} \tilde{C}_1 \\ \tilde{C}_2 \end{pmatrix} = \hbar g \begin{pmatrix} 0 & e^{-i\Delta t} \sqrt{m_c + 1} \\ e^{i\Delta t} \sqrt{m_c + 1} & 0 \end{pmatrix} \begin{pmatrix} \tilde{C}_1 \\ \tilde{C}_2 \end{pmatrix}, \quad (2.25)$$

where herein the time dependence in the arguments of the coefficients is omitted. To simplify this further, a transformation into the ‘rotating’ basis is performed. This is done by a unitary ($1 = UU^\dagger = U^\dagger U \Rightarrow U^\dagger = U^{-1}$), time dependent transformation with:

$$U := \begin{pmatrix} e^{i\Delta t/2} & 0 \\ 0 & e^{-i\Delta t/2} \end{pmatrix}, \quad (2.26)$$

$$\begin{pmatrix} C_1 \\ C_2 \end{pmatrix} := \begin{pmatrix} e^{i\Delta t/2} & 0 \\ 0 & e^{-i\Delta t/2} \end{pmatrix} \begin{pmatrix} \tilde{C}_1 \\ \tilde{C}_2 \end{pmatrix}, \quad (2.27)$$

and the following familiar form is found:

$$i\hbar \frac{d}{dt} \begin{pmatrix} C_1 \\ C_2 \end{pmatrix} = \underbrace{\hbar \begin{pmatrix} \frac{-\Delta}{2} & g\sqrt{m+1} \\ g\sqrt{m+1} & \frac{\Delta}{2} \end{pmatrix}}_{=: H_I} \begin{pmatrix} C_1 \\ C_2 \end{pmatrix}. \quad (2.28)$$

This coupled differential equation takes the well-known form for the interaction of a two-level system with a laser. The solution is obtained by transforming with a time independent unitary matrix into a basis where the equations decouple and a solution is easy to find. Transforming back, the dynamics in the $\{|e, n_v, m_c\rangle, |g, n_v, m_c + 1\rangle\}$ basis are found. Rabi oscillations occur with the frequency:

$$\Omega_{carrier} := \sqrt{\Delta^2 + 4g^2(m_c + 1)}, \quad (2.29)$$

which is the quantised expression for the Rabi frequency. For zero detuning ($\Delta = 0$) and the atom initially excited ($C_1(t = 0) = 1$, $C_2(t = 0) = 0$), the coefficients have the time dependence:

$$C_1(t) = \cos\left(\frac{\Omega_{carrier}(\Delta = 0)}{2} \cdot t\right), \quad (2.30)$$

$$C_2(t) = -i \cdot \sin\left(\frac{\Omega_{carrier}(\Delta = 0)}{2} \cdot t\right). \quad (2.31)$$

The important point to make here is that as seen from (2.29), even in the case of no photons ($m_c = 0$), there are Rabi oscillations, provided that the

atom is initially in the excited state. This is usually not the case for an atom interacting with a freely propagating laser beam. Turning off the laser the excited atom decays exponentially, without any periodic re-population of the upper level. The reason for this decay is the coupling to an infinity of vacuum modes. These modes are responsible for the spontaneous emission and lead to an exponential decay (Weisskopf–Wigner Theory) [17]. The aim of this work is to realise the single mode model and work with just one particular electric field mode. To do this in the experiment, only one particular mode of the vacuum must be supported, making all others to some extent negligible. Experimentally, this is done by choosing special boundary conditions for the electric field with the help of a cavity.

Dynamics on the first-order sidebands

Consider now the dynamics in the antinode:

$$\begin{aligned} \tilde{H}_I \simeq \hbar g \times \{ & -\eta[\sigma_+ a_v^\dagger b_c e^{i(\Delta+\omega_v)t} \\ & + \sigma_- a_v^\dagger b_c^\dagger e^{-i(\Delta-\omega_v)t} \\ & + \sigma_+ a_v b_c e^{i(\Delta-\omega_v)t} \\ & + \sigma_- a_v b_c^\dagger e^{-i(\Delta+\omega_v)t}] + \mathcal{O}(\eta^3) \}. \end{aligned} \quad (2.32)$$

\tilde{H}_I couples states that differ by one cavity and by one atom excitation quantum, as well as by one vibrational quantum n_v . Consider the case where the light is red detuned by $\Delta = -\omega_v + \delta$ (figure (2.3)). Again a rotating wave approximation can be applied and the Hamiltonian becomes:

$$\tilde{H}_I \simeq \hbar g \times \{ -\eta[\sigma_+ a_v b_c e^{-i\delta t} + \sigma_- a_v^\dagger b_c^\dagger e^{i\delta t}] + \mathcal{O}(\eta^3) \}. \quad (2.33)$$

It is possible to choose as a basis: $\{|e, n_v - 1, m_c\rangle, |g, n_v, m_c + 1\rangle\}$. The dynamics of interest are:

$$|\psi(t)\rangle_I := e^{iH_0 t/\hbar} |\psi(t)\rangle = \tilde{C}_1(t) |e, n_v - 1, m_c\rangle + \tilde{C}_2(t) |g, n_v, m_c + 1\rangle, \quad (2.34)$$

which is determined from:

$$i\hbar \frac{d}{dt} |\psi(t)\rangle_I = \tilde{H}_I |\psi(t)\rangle_I. \quad (2.35)$$

With the use of (2.2) the non-zero matrix elements are obtained:

$$\begin{aligned} \langle e, n_v - 1, m_c | \sigma_+ a_v b_c | g, n_v, m_c + 1 \rangle &= \langle g, n_v, m_c + 1 | \sigma_- a_v^\dagger b_c^\dagger | e, n_v - 1, m_c \rangle \\ &= \sqrt{n_v} \sqrt{m_c + 1}, \end{aligned} \quad (2.36)$$

and for the matrix of \tilde{H}_I it is found:

$$\tilde{H}_I = -\hbar\eta g \begin{pmatrix} 0 & e^{-i\delta t} \sqrt{n_v} \sqrt{m_c + 1} \\ e^{i\delta t} \sqrt{n_v} \sqrt{m_c + 1} & 0 \end{pmatrix}. \quad (2.37)$$

Hence, (2.35) becomes:

$$i\hbar \frac{d}{dt} \begin{pmatrix} \tilde{C}_1 \\ \tilde{C}_2 \end{pmatrix} = -\hbar\eta g \begin{pmatrix} 0 & e^{-i\delta t} \sqrt{n_v} \sqrt{m_c + 1} \\ e^{i\delta t} \sqrt{n_v} \sqrt{m_c + 1} & 0 \end{pmatrix} \begin{pmatrix} \tilde{C}_1 \\ \tilde{C}_2 \end{pmatrix}, \quad (2.38)$$

where from now on the time dependence in the arguments is omitted. To simplify this further, a transformation into the ‘rotating’ basis is carried out using the unitary matrix U given in equation (2.26). The resulting expression, which is analogous to (2.28), is given by:

$$i\hbar \frac{d}{dt} \begin{pmatrix} C_1 \\ C_2 \end{pmatrix} = \underbrace{\hbar \begin{pmatrix} \frac{-\delta}{2} & -\eta g \sqrt{n_v} \sqrt{m_c + 1} \\ -\eta g \sqrt{n_v} \sqrt{m_c + 1} & \frac{\delta}{2} \end{pmatrix}}_{=: H_I} \begin{pmatrix} C_1 \\ C_2 \end{pmatrix}. \quad (2.39)$$

The solution is obtained in the same manner as for the carrier transitions. Rabi oscillations are again found, but with the Rabi frequency given by:

$$\Omega_{red-sb} := \sqrt{\delta^2 + 4(\eta g)^2 n_v (m_c + 1)}. \quad (2.40)$$

With the actual transitions on resonance ($\Delta = 0$, $\delta = 0$) it is now possible to compare expression (2.29) and (2.40). The familiar result for the Rabi frequencies is recovered:

$$\Omega_{carrier} = 2g\sqrt{m_c + 1}, \quad (2.41)$$

$$\Omega_{red-sb} = 2\eta g \sqrt{n_v (m_c + 1)} = \eta \sqrt{n_v} \Omega_{carrier}. \quad (2.42)$$

An analogous analysis can be carried out for the blue sideband transitions. The basis states $|e, n_v + 1, m_c\rangle$ and $|g, n_v, m_c + 1\rangle$ lead, for zero detuning ($\delta = 0$), to the expression:

$$\Omega_{blue-sb} := 2g\eta \sqrt{(n_v + 1)(m_c + 1)} = \eta \sqrt{n_v + 1} \Omega_{carrier}. \quad (2.43)$$

2.1.2 Model with Dissipation

In a more realistic model there will be decoherence due to coupling to the environment. For example, the atom can decay into one of the infinite modes of the free field, instead of emitting just into the cavity mode. The cavity itself can lose photons by absorption or transmission through the mirrors. Including these effects in the theoretical description leads to the density-matrix formalism. This section focuses on carrier transitions where no attention has to be paid to the harmonic trapping potential. The master equation for an atom-cavity system including the dissipative effects stated above is given by [18]:

$$\dot{\rho} = \frac{1}{i\hbar}[H_I, \rho] + L\rho, \quad (2.44)$$

$$L\rho = \gamma_{\perp}(2\sigma_{-}\rho\sigma_{+} - \sigma_{+}\sigma_{-}\rho - \rho\sigma_{+}\sigma_{-}) + \kappa(2b_c\rho b_c^{\dagger} - b_c^{\dagger}b_c\rho - \rho b_c^{\dagger}b_c). \quad (2.45)$$

Here, ρ is the atom-cavity density matrix, γ_{\perp} is the transversal decay rate of the atom into free space ($\gamma_{\perp} = \gamma_{\parallel}/2$, where γ_{\parallel} is the decay rate of the population) and κ is the decay rate of the cavity field (2κ is the photon

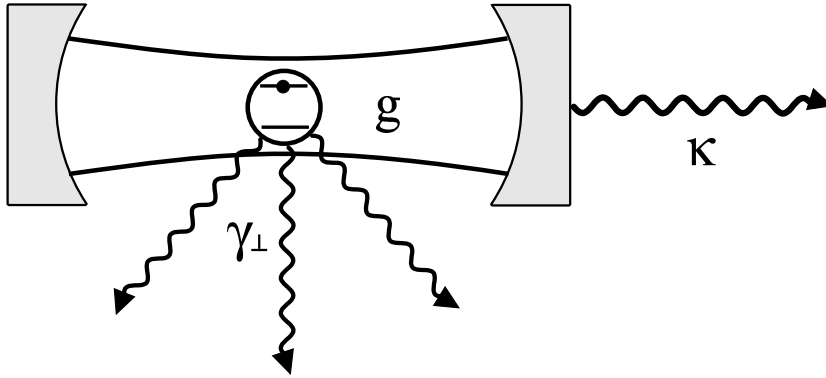


Figure 2.5: A more realistic scheme of a two-level system interacting (coupling g) with a single cavity mode. κ denotes the cavity decay rate due to imperfect mirrors, γ_{\perp} accounts for the atomic decay into the free space background.

decay rate). Defining the non-hermitian Hamiltonian H_{eff} :

$$H_{\text{eff}} := H_I + H_{\text{dis}} , \quad (2.46)$$

$$H_{\text{dis}} := -i\hbar[\gamma_{\perp}\sigma_+\sigma_- + \kappa b_c^\dagger b_c] , \quad (2.47)$$

(2.44) can be written as:

$$\dot{\rho} = \frac{1}{i\hbar}(H_{\text{eff}}\rho - \rho H_{\text{eff}}^\dagger) + 2\gamma_{\perp}\sigma_-\rho\sigma_+ + 2\kappa b_c\rho b_c^\dagger . \quad (2.48)$$

Consider only the first three lowest energy states, the zero quantum state $|g, 0\rangle$ and the two states $|e, 0\rangle$ and $|g, 1\rangle$, with either an atom or cavity excitation quantum. Any dissipative process leads the system to the $|g, 0\rangle$ state. Therefore it is possible to use the state $|\psi\rangle = C_1(t)|e, 0\rangle + C_2(t)|g, 1\rangle$ and its evolution is given by:

$$i\hbar\frac{d}{dt}|\psi\rangle = H_{\text{eff}}|\psi\rangle . \quad (2.49)$$

The norm of $|\psi\rangle$ decreases as dissipative processes occur and the system evolves into the $|g, 0\rangle$ state. The matrix formulation is given by:

$$\begin{aligned} H_{\text{eff}} &= \hbar \begin{pmatrix} \frac{-\Delta}{2} & g \\ g & \frac{\Delta}{2} \end{pmatrix} - i\hbar \begin{pmatrix} \gamma_{\perp} & 0 \\ 0 & \kappa \end{pmatrix} \\ &= \hbar \begin{pmatrix} \frac{-\Delta}{2} - i\gamma_{\perp} & g \\ g & \frac{\Delta}{2} - i\kappa \end{pmatrix} , \end{aligned} \quad (2.50)$$

and the following is obtained:

$$\frac{d}{dt} \begin{pmatrix} C_1 \\ C_2 \end{pmatrix} = \begin{pmatrix} \frac{i\Delta}{2} - \gamma_{\perp} & -ig \\ -ig & \frac{-i\Delta}{2} - \kappa \end{pmatrix} \begin{pmatrix} C_1 \\ C_2 \end{pmatrix} . \quad (2.51)$$

This is a system of first order coupled differential equations with constant coefficients. A solution is obtained by transforming into a basis where the equations decouple and can be solved easily, the solution has the form:

$$\{ \tilde{C}_1 \sim e^{\lambda_+ t} , \quad \tilde{C}_2 \sim e^{\lambda_- t} \} , \quad (2.52)$$

λ_{\pm} are the eigenvalues of the coefficient matrix. For the matrix in equation (2.51) it is obtained:

$$\lambda_{\pm} = -\frac{\gamma_{\perp} + \kappa}{2} \pm \sqrt{\left(\frac{i\Delta - \gamma_{\perp} - \kappa}{2}\right)^2 - g^2} . \quad (2.53)$$

The case for zero detuning ($\Delta = 0$) will now be considered.

Strong coupling limit

If $g \gg \gamma_{\perp}$, $g \gg \kappa$, the coupling exceeds the decay and the solution shows damped Rabi oscillations between $|e, 0\rangle$ and $|g, 1\rangle$. From the eigenvalues:

$$\lambda_{\pm} = -\frac{\gamma_{\perp} + \kappa}{2} \pm \frac{i}{2} \sqrt{4g^2 - (\kappa - \gamma_{\perp})^2} \quad (2.54)$$

the Rabi frequency can be inferred:

$$\Omega = \sqrt{4g^2 - (\kappa - \gamma_{\perp})^2} \approx 2g. \quad (2.55)$$

Weak coupling limit

In this case the eigenvalues λ_{\pm} are real ($4g^2 < (\gamma_{\perp} - \kappa)^2$) and no oscillatory behaviour occurs. In the ‘bad cavity regime’ where:

$$\gamma_{\perp} \ll g^2/\kappa \ll \kappa, \quad (2.56)$$

the following can be written:

$$\begin{aligned} \lambda_{\pm} &= -\frac{\gamma_{\perp} + \kappa}{2} \pm \frac{\kappa - \gamma_{\perp}}{2} \sqrt{1 - \frac{4g^2}{(\kappa - \gamma_{\perp})^2}} \\ &\approx -\frac{\gamma_{\perp} + \kappa}{2} \pm \frac{\kappa - \gamma_{\perp}}{2} \left(1 - \frac{4g^2}{2(\kappa - \gamma_{\perp})^2} + \mathcal{O}\left(\frac{g}{\kappa}\right)^4 \right), \\ \lambda_+ &\approx -\left(\gamma_{\perp} + \frac{g^2}{\kappa}\right) =: -\gamma_{\perp}(1 + 2C) \end{aligned} \quad (2.57)$$

$$\lambda_- \approx -\left(\kappa - \frac{g^2}{\kappa}\right), \quad (2.58)$$

where the cooperativity parameter is defined:

$$C := \frac{g^2}{2\gamma_{\perp}\kappa}. \quad (2.59)$$

Considering the eigenvectors associated with λ_+ and λ_- under the condition (2.56), the eigenvectors are found to be:

$$\lambda_+ : \quad \frac{1}{\sqrt{\kappa^2 + g^2}} \begin{pmatrix} \kappa \\ -ig \end{pmatrix}, \quad (2.60)$$

$$\lambda_- : \quad \frac{1}{\sqrt{\kappa^2 + g^2}} \begin{pmatrix} ig \\ \kappa \end{pmatrix}. \quad (2.61)$$

From (2.60) it is seen that the state associated with λ_+ has a strong contribution ($\kappa \gg g$) from $|e, 0\rangle$. λ_+ is therefore related to the atomic decay and it is seen from equation (2.57) that this decay is increased by the Purcell factor $F := (2C + 1)$ [19]. The atomic decay occurs preferentially into the cavity mode which then further decays. The fraction of emission emitted into the cavity mode is $\beta = 2C/(2C + 1)$.

The eigenvector in (2.61), on the other hand, shows that the state associated with λ_- is dominated by $|g, 1\rangle$. λ_- is therefore related to the decay of the cavity field. From equation (2.58) we see that this decay is decreased by the factor $(1 - g^2/\kappa^2)$, i.e. the cavity is ‘refilled’ by the radiating atom.

By choosing special boundary conditions for the electro-magnetic field and thereby influencing the mode structure as well as enhancing vacuum fluctuations, ‘spontaneous’ decay can be altered. By introducing the cavity we have disturbed the isotropy of space. This forces the atom to predominantly emit into the cavity mode synthesising a ‘one-dimensional’ atom [20]. In the so called ‘bad atom limit’ κ and γ_\perp are interchanged ($\kappa \ll g^2/\gamma_\perp \ll \gamma_\perp$), and the cavity decays faster via the coupled atom.

2.2 Experiments on Cavity QED

2.2.1 Historic Overview

The theoretical concept explained in the last section, especially the alteration of spontaneous emission rates for atoms subjected to electro-magnetic fields having boundary conditions differing from the conditions of free space, was first conceived by Purcell in 1946 [19]. In his short note Purcell mentioned the possible modification of spontaneous decay for a magnetic spin transition coupled to a resonant circuit. Theoretical work on quantum-electro-dynamics in confined spaces followed [21].

The first experimental verification of this concept was achieved by K. H. Drexhage [22] in 1968. He showed that the fluorescence decay time of a mono-molecular layer of excited dye molecules is influenced by the boundary imposed by a mirror surface. Regarding single atom systems, enhanced emission was first observed by S. Haroche *et al.* [23], whereas D. Kleppner *et al.* reported on inhibited spontaneous emission [24, 25]. Haroche and Kleppner used Rydberg-states with microwave transitions (for suppression of spontaneous emission in the near infrared cf. [26]), with wavelengths in the millimeter domain, where superconducting cavities can be used. A mode volume on the order of λ^3 is relatively easy to realise technically, strongly influencing the mode density and thereby enhancing the various CQED ef-

fects. Related observations were made by Dehmelt *et al.* on the decay of the cyclotron motion of an electron trapped in a Penning trap [27]. The experiments mentioned so far were performed in the weak coupling regime. With the development of high quality superconducting cavities it also became possible to achieve strong coupling. The development of the micro-maser [28] allowed a lot of interesting experiments in the strong coupling regime [29, 30] to be performed. The disadvantage of experiments in the microwave region is that measurements are limited to the atomic state because the field quanta cannot be observed. This differs from the optical regime where photons can be detected. With the development of highly reflecting mirror coatings and the resulting high finesse cavities it became possible to explore cavity QED effects with optical cavities. The first experiments in the visible regime were done by M. S. Feld *et al.* [31], who enhanced and inhibited the lifetime of Yb-atoms in an atomic beam passing through a confocal optical resonator and P. Mataloni *et al.* [32], who also observed enhanced and inhibited lifetimes, but for dye molecules in a cavity.

In recent years there were activities in several groups using slow atomic beams of rubidium [33, 34, 35, 36], cesium [37, 38] or barium [39]. In some of these experiments only a single atom (on average) can interact with the cavity mode and atoms can be trapped to some extent in the cavity field [38, 35]. The concepts of cavity QED also emerged in semiconductor physics where spontaneous emission alteration [40] and vacuum Rabi splitting [41] have been observed. More recently ‘quantum-dots’ (QDs) have been used to explore cavity QED effects in semiconductor physics. In 1998 an ensemble of QDs was coupled to the mode of a microscopic post (pillar) etched from a distributed Bragg reflector cavity [42]. With technological improvements it became possible to couple a single QD to a micro-cavity using micro disk resonators [43] and partially inhibited spontaneous emission could be demonstrated [44] as well as enhanced spontaneous emission [42, 43, 45, 46] up to a Purcell factor of $F \approx 6$. The coupling of a single QD to a micro-post cavity was demonstrated [45]. Very recently an ensemble of QDs has been coupled to a photonic crystal defect cavity [46].

2.2.2 Cavity QED Experiments in Perspective

The standard setup for cavity QED experiments in the optical regime as used in Kimble’s and Rempe’s group is now briefly discussed: there is an extremely small cavity (length $\approx 10 - 100 \mu\text{m}$) resonant with an atomic dipole transition. The atoms are provided by a magneto-optical trap and fall through the cavity [38, 36]. Alternatively an atomic fountain can be used to transport atoms to the cavity [47]. With these experiments it is relatively

easy to achieve strong coupling ($g \gg \gamma_{\perp}$, $g \gg \kappa$) provided the atoms pass through an antinode of the field. The crucial point is to satisfy the inequality $g \gg \gamma_{\perp}$. The dependence of the mode volume V on the atom–cavity coupling g is $g \propto V^{-1/2}$, so a small mode volume V has to be used to reach the strong coupling regime.

The major disadvantage of these neutral atom cavity QED experiments is obvious: the atoms are never at a fixed position but pass for some limited interaction time through the node-antinode pattern and the transversal mode structure, thereby experiencing a position dependent coupling $g = g(\mathbf{r}(t))$. Even if they are trapped to some extent to one antinode [35, 38], their actual position is never really confined so much that the position dependence of $g(\mathbf{r})$ can be ignored. In the quantum-dot experiments a different problem occurs: the experiments depend strongly on the sample. The position and the emission wavelength of a QD for example is not predetermined, a lot of micro-cavities have to be grown to find one with a single QD at the right position and with spectral overlap with one of the cavity modes. After choosing a micro-cavity and its single QD, it is not possible to adjust the coupling between QD and field-mode by a change in spatial position. It is also not possible to copy a sample with exactly the same properties. Nevertheless the technologies in semiconductor physics are well developed and highly integrated micro setups may be envisaged.

With these facts in mind, it is clear that the experimental challenge is to set up an experiment in the strong coupling regime with a single atom confined to an arbitrary fixed position inside an optical cavity (for weak coupling, g can be reduced by moving the atom from the antinode to the node or vice versa, depending on the transition). One way of achieving this goal is to use a single charged atom (i.e. an ion) confined in a Paul trap. The spatial extent of the ion's wavefunction can be made smaller than 30 nm and its position in the standing wave can be chosen freely. In addition, the trapping time at pressures of $\sim 10^{-10}$ mbar is in the range of several hours.

On the other hand, it is difficult to achieve strong coupling because the cavity cannot be made as small as in neutral atom experiments. Charges accumulating on nonconducting elements like mirror surfaces strongly influence the ion if they are close to it. Additionally, the cavity has to be built around the ion trap. One idea is to use a quadrupole transition for which the inequality $g \gg \gamma_{\perp}$ is relatively easy to fulfill. However, the problem is just shifted now and one has to satisfy $g \gg \kappa$, which requires a very high finesse \mathcal{F} in order to decrease κ . However, there are many experiments (among them the atom–photon interface i.e. the one-dimensional atom [20]) which only require weak coupling which is easier to achieve. The realisation of ion–cavity coupling is discussed in more detail in chapter (3).

Chapter 3

Realisation of the Model

This chapter describes the experimental realisation of the theoretical model developed in the last chapter, namely that of a two-level system trapped in a harmonic potential coupled to a single mode of the electro-magnetic field. In the first section the relevant physical properties of Ca^+ ions important for the implementation of the ion-cavity coupling are discussed. In the second section the principles of trapping ions in Paul traps are reviewed. The third section is devoted to the high finesse cavity which selects one particular electro-magnetic mode from the infinite number of free space background modes. In the last section these three key parts are put together and the system composed of ion, trap and cavity is investigated.

3.1 Ca^+ -Ion as Quantum Mechanical System

In the experiments described in this thesis a single $^{40}\text{Ca}^+$ -ion is confined in a miniaturised Paul-trap. It serves as a quantum mechanical system that can be, to a large extent, deterministically controlled. This section presents the techniques used to trap and interrogate the ion. Most of the topics are already described extensively in papers, diploma- and doctoral-theses [6, 9, 10, 11] and these topics are just reviewed here.

3.1.1 Ca^+ Level Scheme and Relevant Transitions

The particular isotope of calcium used for the cavity QED experiments presented in this thesis is $^{40}\text{Ca}^+$ and is the most abundant isotope, comprising 97% of naturally occurring calcium. $^{40}\text{Ca}^+$ has zero nuclear spin as do all other natural isotopes with the exception of ^{43}Ca ($I = 7/2$). Being singly ionised, a hydrogen-like level structure arises. In figure (3.1) the five lowest

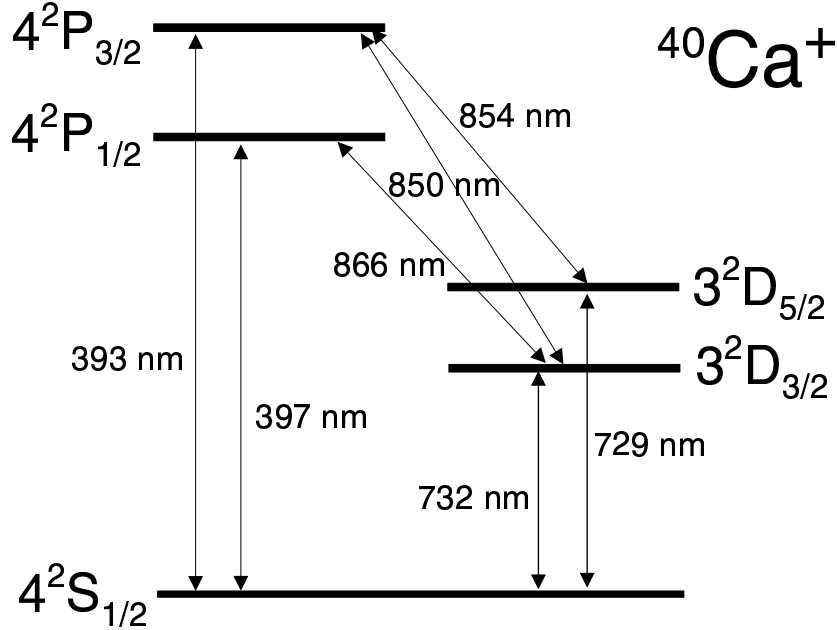


Figure 3.1: Term scheme of the five lowest lying levels of $^{40}\text{Ca}^+$.

lying levels of $^{40}\text{Ca}^+$ are shown. For Doppler cooling and fluorescence detection the $S_{1/2} \leftrightarrow P_{1/2}$ transition is used. This transition at 397 nm has a linewidth Γ of 20 MHz. To cool the ion via the Doppler effect, the driving laser is red detuned by about $\Gamma/2 = 10$ MHz. The $P_{1/2}$ level decays with a probability of $\approx 6\%$ into the metastable (lifetime $\tau \approx 1$ s) $D_{3/2}$ level. To prevent this optical pumping, a repumping laser at 866 nm drives simultaneously the $D_{3/2} \leftrightarrow P_{1/2}$ transition. The other metastable level, the $D_{5/2}$ level, is excited with a laser at 729 nm (a quadrupole transition). The $D_{5/2}$ level together with the $S_{1/2}$ ground state level form a two-level system. The long lifetime $\tau \approx 1$ s of the $D_{5/2}$ level allows for the storage of information i.e. encoding a quantum bit (qubit) of information in a superposition of $S_{1/2}$ and $D_{5/2}$ states [6]. All experiments described in chapter (5) and (6) are performed on the $S_{1/2} \leftrightarrow D_{5/2}$ qubit transition. The use of the 854 nm laser is to reset excitation of the $D_{5/2}$ level. The transition wavelengths and lifetimes [15] of relevant $^{40}\text{Ca}^+$ levels are listed in table (3.1).

Dipole transitions

		$S_{1/2} \leftrightarrow P_{1/2}$	$S_{1/2} \leftrightarrow P_{3/2}$	$P_{1/2} \leftrightarrow D_{3/2}$	$P_{3/2} \leftrightarrow D_{3/2}$	$P_{3/2} \leftrightarrow D_{5/2}$
τ_{nat}	ns	7.7(2)	7.4(3)	94.3	901	101
λ_{air}	nm	396.847	393.366	866.214	849.802	854.209

Quadrupole transitions

		$S_{1/2} \leftrightarrow D_{5/2}$	$S_{1/2} \leftrightarrow D_{3/2}$
τ_{nat}	s	1.045	1.080
λ_{air}	nm	729.147	732.389

Table 3.1: Transition wavelengths and level lifetimes of $^{40}\text{Ca}^+$ [15]. The laser sources needed to drive the relevant transitions are described in chapter (4).

3.1.2 Zeeman Splitting

Consider the levels involved in the $S_{1/2} \leftrightarrow D_{5/2}$ quadrupole transition. If a magnetic field \mathbf{B} is applied, the levels split into a number of sub-levels. The splitting from the degenerate zero magnetic field case is given by:

$$\Delta E = g_j \mu_B B m_j , \quad (3.1)$$

where m_j is the magnetic quantum number, μ_B is the Bohr magneton and the g_j are the Landé factors given in the following table:

Landé factors for relevant energy levels [48]

	$S_{1/2}$	$P_{1/2}$	$P_{3/2}$	$D_{3/2}$	$D_{5/2}$
g_j	2	$2/3$	$4/3$	$4/5$	$6/5$

When applying a magnetic field \mathbf{B} two things must be taken into account: on one hand the goal is to distinguish and resolve all spectral lines of interest. Having chosen a particular carrier transition, it is important that all associated sideband transitions are well separated from all other carrier or sideband transitions. This is the case in strong magnetic fields when the levels are more greatly separated and hence the spectral lines are more separated in frequency. On the other hand the strong magnetic field also broadens

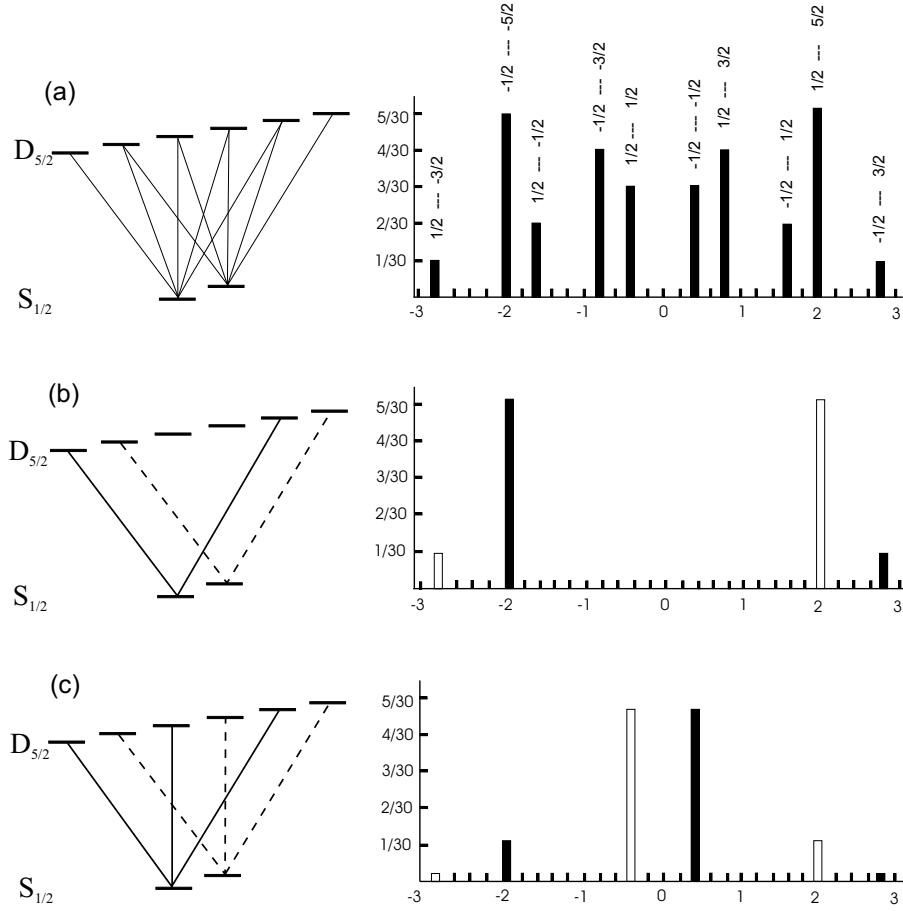


Figure 3.2: The $S_{1/2} \leftrightarrow D_{5/2}$ quadrupole transition splits into ten allowed components (a) if a magnetic field is applied (given in units of $\mu_B B$). The relative line strength is proportional to their squared Clebsch–Gordan factors [15, 16]. Optical pumping to one of the $S_{1/2}$ levels reduces this number to five. By taking the geometric configuration of polarisation \mathbf{e} , magnetic field \mathbf{B} and beam direction \mathbf{k} into account, further suppression of lines can be achieved (b,c). In (b), $\mathbf{e} \perp \mathbf{B} \perp \mathbf{k}$, after optical pumping only the strongest and the weakest transition remain, these being separated by $\approx 4.8 \times 1.4$ MHz/Gauss. In (c), the configuration is as follows: wavevector \mathbf{k} and magnetic field \mathbf{B} subtend an angle of 45° . The polarisation \mathbf{e} is chosen to lie in the plane spanned by \mathbf{k} and \mathbf{B} . This configuration is appropriate if magnetic field fluctuations are critical because their influence on the line shift is reduced by 80% compared to case (b). Figure taken from [10].

the $S_{1/2} \leftrightarrow P_{1/2}$ Doppler cooling transition thereby increasing the Doppler limit¹.

If one considers the qubit transition at 729 nm and the quadrupole selection rule $\Delta m_j = 0, \pm 1, \pm 2$, a total of ten transitions are allowed (see figure (3.2)). Optical pumping with σ_{\pm} -light on the 397 nm transition to one of the $S_{1/2}$ sub-levels reduces the number of observed transitions to five. By choosing the angle between the polarisation vector \mathbf{e} of the 729 nm light and magnetic field direction \mathbf{B} as well as the angle between magnetic field and beam direction \mathbf{k} , further suppression of transitions can be achieved (see figures (3.2) and (3.3)). An extensive discussion can be found in [10].

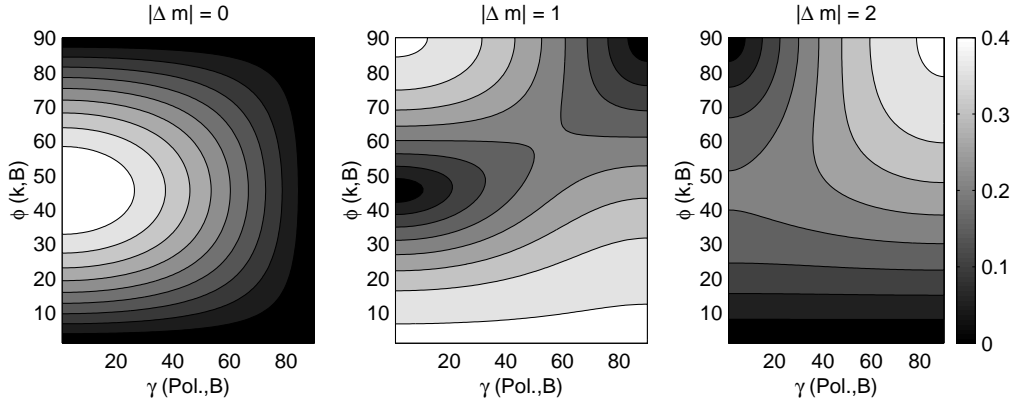


Figure 3.3: Geometrical consideration of the relative coupling strength on the $S_{1/2} \leftrightarrow D_{5/2}$ quadrupole transition in general for transitions with $|\Delta m| = 0$, $|\Delta m| = 1$ and $|\Delta m| = 2$. ϕ denotes the angle between laser beam \mathbf{k} and magnetic field \mathbf{B} . γ is the angle between polarisation \mathbf{e} and the projection of \mathbf{B} onto the plane normal to \mathbf{k} . Dark shadings correspond to low coupling. Figure taken from [10].

¹Note that the spectral components of the $S_{1/2} \leftrightarrow P_{1/2}$ transition are not resolved.

3.2 Paul Traps

The trapping of charged particles in dynamic electric fields was realised by W. Paul and coworkers in 1958 [49]. Since then Paul-type traps have been used in a variety of experiments. This section reviews the principles of Paul traps. The material can be found in every doctoral thesis prepared in our group [10, 9, 11, 12, 8] as well as in several papers [50, 51].

3.2.1 General Principle

It is obvious from the first Maxwell equation in vacuum:

$$\nabla \cdot \mathbf{E} = 0, \quad (3.2)$$

that no static potential exists that confines the motion of a charged particle in free space in all directions. However, a charged particle can be trapped if time dependent fields are used. Consider the following time dependent quadrupole potential:

$$\Phi(\vec{x}, t) = \Phi_0(t) \sum_{i=1}^3 \alpha_i \left(\frac{x_i}{\tilde{r}} \right)^2, \quad (3.3)$$

where

$$\Phi_0(t) = U + V \cos(\Omega_{RF}t), \quad (3.4)$$

and the α_i, \tilde{r} are parameters to be determined. To satisfy equation (3.2) we demand $\sum \alpha_i = 0$. The equations of motion for a charged particle in this potential are given by:

$$\ddot{x}_i + \frac{2\alpha_i Q}{m\tilde{r}^2} (U + V \cos(\Omega_{RF}t)) x_i = 0, \quad (3.5)$$

where m is the particle mass and Q its charge. This differential equation is called a Mathieu equation and is well known in mathematics. It is usually written as:

$$\frac{d^2 u}{d\zeta^2} + (a - 2q \cos(2\zeta))u = 0. \quad (3.6)$$

With the substitutions:

$$a := a_i = -\frac{8\alpha_i Q U}{m\tilde{r}^2 \Omega_{RF}^2}, \quad (3.7)$$

$$q := q_i = \frac{4\alpha_i Q V}{m\tilde{r}^2 \Omega_{RF}^2}, \quad (3.8)$$

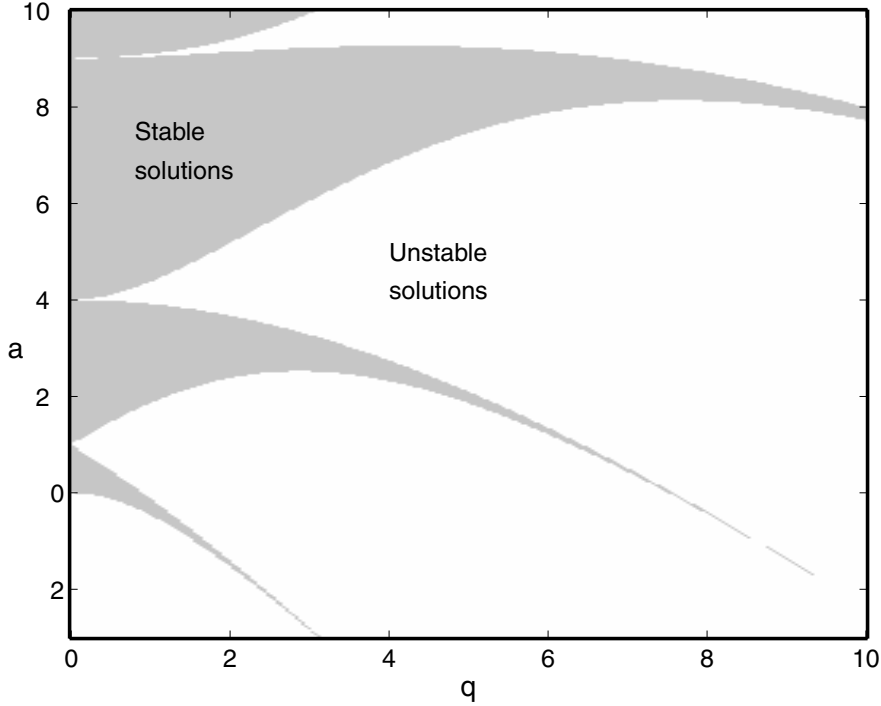


Figure 3.4: Stability diagram for the Mathieu equation (3.6). Parameter choices in the shaded areas lead to stable solutions. Figure taken from [10].

and $\zeta = \frac{1}{2}\Omega_{RF}t$ equation (3.5) is obtained. The solutions to (3.6) can be expressed as [50]:

$$u(\zeta) = A \sum_{n \in \mathbb{Z}} C_{2n} \cos((2n + \beta)\zeta) + B \sum_{n \in \mathbb{Z}} C_{2n} \sin((2n + \beta)\zeta), \quad (3.9)$$

where the C_{2n} satisfy a certain recursion relation and $\beta = \beta(a, q)$ is in general a complex number. We are interested in bounded solutions that correspond to the stable trapping of particles. Figure (3.4) shows the stability diagram related to equation (3.6). Stable trapping is only possible if the solution for any direction i with given parameters a_i, q_i is bounded. For a rotationally invariant quadrupole potential (z being the symmetry axis) the parameters a_i and q_i are given by:

$$\begin{aligned} a_x = a_y &= -\frac{8QU}{m(r_0^2 + 2z_0^2)\Omega_{RF}^2}, & a_z &= -2a_x, \\ q_x = q_y &= \frac{4QV}{m(r_0^2 + 2z_0^2)\Omega_{RF}^2}, & q_z &= -2q_x, \end{aligned} \quad (3.10)$$

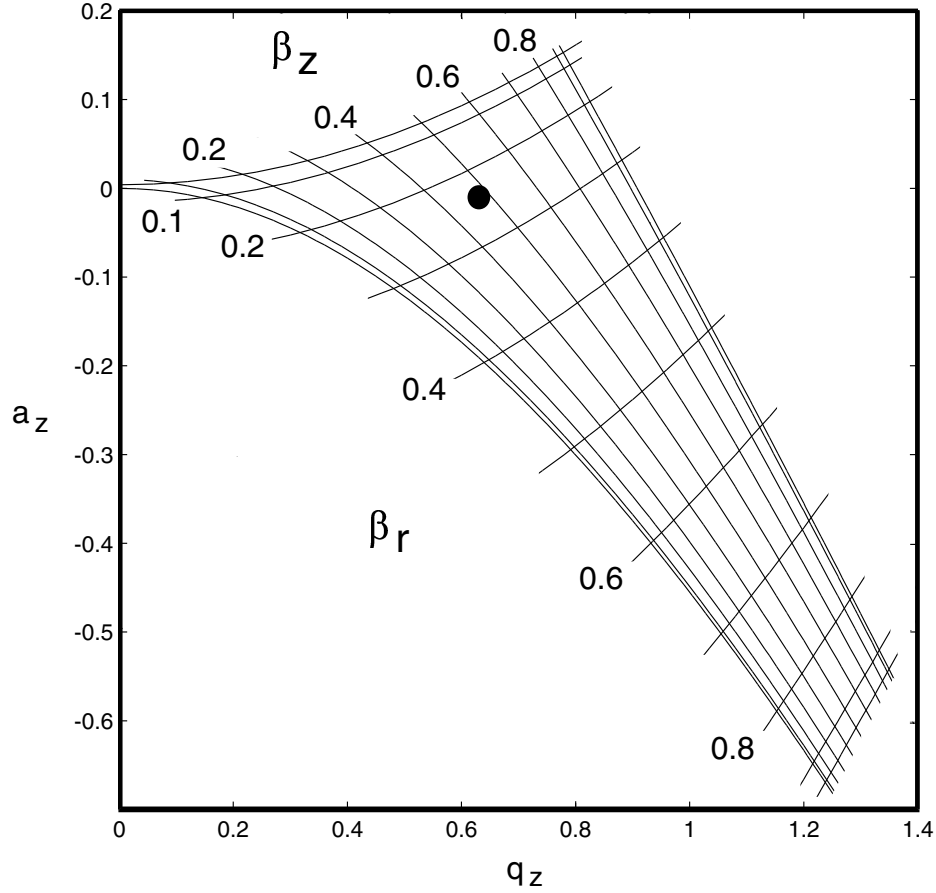


Figure 3.5: The lowest stability zone in a Paul trap with rotational symmetry. The contour lines give the values of ω_r and ω_z in units of $\Omega_{RF}/2$. The dot indicates the region our trap is operated in. Figure taken from [10].

where we have chosen: $\alpha_x = \alpha_y = 1$, $\alpha_z = -2$ and $\tilde{r}^2 = r_0^2 + 2z_0^2$. This choice ensures that $\Phi(r_0, 0, 0, t) - \Phi(0, 0, z_0, t) = U + V \cos(\Omega_{RF}t)$. The DC tip voltage is given by U and the radio frequency (RF) amplitude is described by V . Figure (3.5) shows the relevant part of the stability diagram of a trap with rotational symmetry. For $a_i \ll q_i \ll 1$ the solution to the equation of motion (3.5) can be approximated by:

$$r_i(t) = r_i^0 \cos(\omega_i t + \phi_i) \left(1 + \frac{q_i}{2} \cos(\Omega_{RF}t) \right), \quad (3.11)$$

where ω_i is given by:

$$\omega_i = \beta_i \frac{\Omega_{RF}}{2} \quad \text{and} \quad \beta_i = \sqrt{a_i + \frac{q_i^2}{2}}. \quad (3.12)$$

From (3.11) we see that the motion of the trapped particle can be decomposed into a harmonic motion (frequency ω_i , secular motion) due to the confining harmonic potential and a faster RF-driven motion (micromotion) being proportional to the distance from the trap center. For a single ion placed at the center of the trap i.e. at the node of the RF-potential, the micromotion is negligible. In practice, static stray fields often shift the ion off-center. In this case the ion must be moved back to the zero field position by static compensation fields. For the experiments outlined here we use the experimental procedure described extensively in [10]. For the following the micromotion can be neglected, and the secular motion is assumed to be generated by a static harmonic potential, the justification of which is given in [52, 53].

3.2.2 Spherical Single Ion Trap

In the experiment it is advantageous to build a ‘stiff trap’ with high secular motion frequencies ω_i and therefore a small extension of the wave packet (i.e. a small η). From (3.12) and (3.10) we see that the secular motion fre-

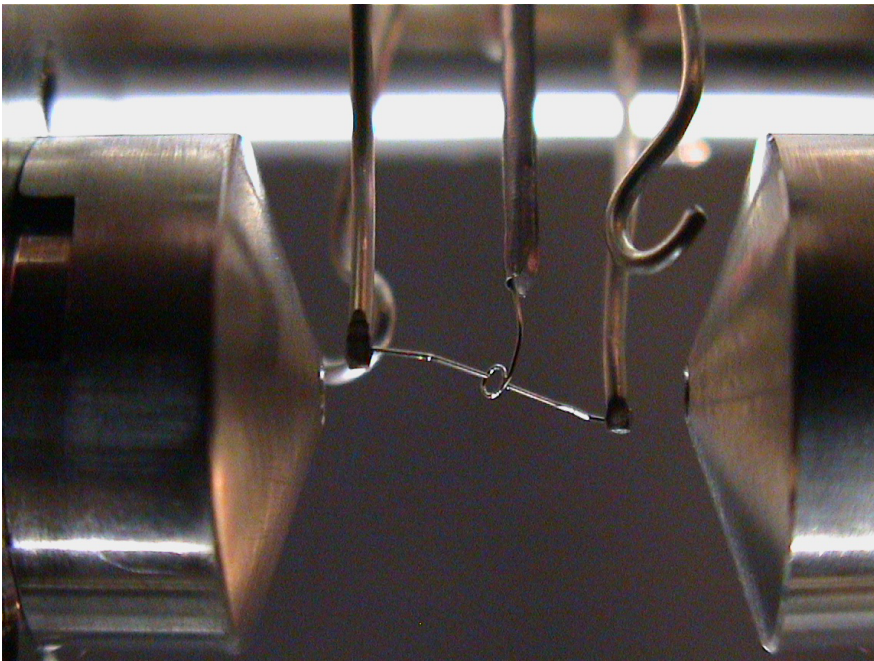


Figure 3.6: The miniaturised Paul trap. The ring electrode (diameter ≈ 1.4 mm) and the endcaps (tip electrodes) are made of molybdenum wire (diameter ≈ 0.2 mm). The hook shaped wires are the compensation electrodes used to shift the ion in the node of the RF field.

quencies ω_i can be increased by feeding the trap with a higher RF frequency Ω_{RF} , higher RF power and by decreasing its size (taking care to remain in a stable trapping region of the stability diagram). In the experiment a combination of all three possibilities has to be balanced taking technical and practical considerations into account.

For ion traps to be operated with just one ion the simplest approach is the following: a ring of wire is connected to a resonant RF circuit, two endcaps made of the same wire are added at the symmetry axis of the ring and connected to ground or some constant offset voltage. A trap of this type is shown in figure (3.6). The field pattern generated by this setup is not a pure quadrupole as can be achieved for hyperbolically shaped electrodes, nevertheless the quadrupole term is by far the leading term in the center at the position of the ion. The advantages these Paul traps offer are their simplicity and their large amount of optical access.

3.3 Optical Resonators

An optical resonator is used to couple the ion to a single mode of the electromagnetic field. To confine the electrical field to a bounded region in space, a stable resonator must be chosen. Furthermore the mode volume should be as small as possible to achieve a high electric field per photon. The position of the ion must be in the cavity waist, where the field is greatest i.e. the probability to find a photon and therefore to interact with the ion is greatest.

3.3.1 Cavity Lifetime τ and Finesse \mathcal{F}

To achieve the requirements previously stated, it is convenient to use a symmetric resonator made of two concave mirrors with equal radius of curvature. From a spectral point of view, the parameters important in characterising the resonator are the mirror distance L and the finesse \mathcal{F} defined by:

$$\mathcal{F} := \frac{\nu_f}{\delta\nu}, \quad (3.13)$$

where ν_f is given by:

$$\nu_f := \frac{c}{2L}, \quad (3.14)$$

and where $\delta\nu$ is the FWHM of the transmission peak. ν_f is called the ‘free spectral range’. Consider a single mirror with field reflectivity r , field transmission t and field losses l . The conservation of energy demands $\mathcal{R} + \mathcal{T} + \mathcal{L} = 1$

where $\mathcal{R} = r^2$, $\mathcal{T} = t^2$ and $\mathcal{L} = l^2$, i.e. the fractions of reflected, transmitted and lost intensities must sum to one. If there are no losses in the cavity volume and geometrically perfect substrates are assumed, the finesse depends only on the reflectivity of the mirrors. For a stable cavity made of two mirrors having the field reflectivity r_1 and r_2 , the finesse \mathcal{F} is given by (note: $r_i \lesssim 1$) [54]:

$$\mathcal{F} = \frac{\pi\sqrt{r_1 r_2}}{1 - r_1 r_2} \simeq \frac{\pi}{1 - r_1 r_2}. \quad (3.15)$$

For identical mirrors $r_i = r$, the product of the field reflectivities $r_1 \cdot r_2$ can be substituted by the intensity reflectivity \mathcal{R} of one of the individual mirrors and the expression further simplifies to:

$$\mathcal{F} \simeq \frac{\pi}{1 - r^2} = \frac{\pi}{1 - \mathcal{R}} = \frac{\pi}{\mathcal{T} + \mathcal{L}}, \quad (3.16)$$

which is sometimes used in the literature [55]. The finesse is related to the cavity energy storage time² by:

$$\mathcal{F} = \frac{\pi c}{L} \cdot \tau. \quad (3.17)$$

Instead of the lifetime τ often the (field-) decay rate κ defined as:

$$\kappa = \frac{1}{2\tau} \quad (3.18)$$

is used. If the finesse \mathcal{F} is divided by π a value is found for the average number of times a photon traverses the cavity before it is transmitted or absorbed by a mirror. This number is of great interest as it corresponds to the number of times the photon passes the trapped ion.

3.3.2 Cavity Waist w_0 and Cavity Mode Volume

The finesse \mathcal{F} is not the only relevant number characterising the cavity system. It is also important to focus the cavity light on the ion i.e. to achieve a small waist³ as well as a small mode volume $L \cdot \pi w_0^2$. Consider the fundamental TEM₀₀ mode in a symmetric cavity of length L . The waist size w_0 (radius of the waist at the cavity center) is given by [54]:

$$w_0^2 = \frac{\lambda}{2\pi} \sqrt{L(2R - L)}, \quad (3.19)$$

²The filled cavity decays exponentially according to $I(t) = I(0) \cdot e^{-\frac{t}{\tau}}$, $I(t)$ being the light intensity at time t .

³The focus should not be too small to reliably move and keep the ion in its center.

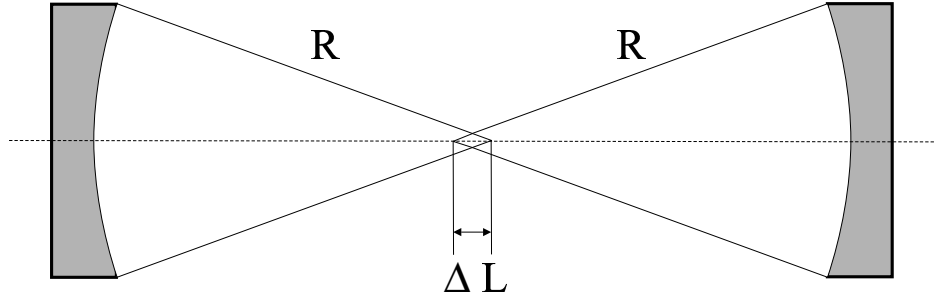


Figure 3.7: Near concentric cavity. The mirrors are separated by slightly less (ΔL) than $2R$.

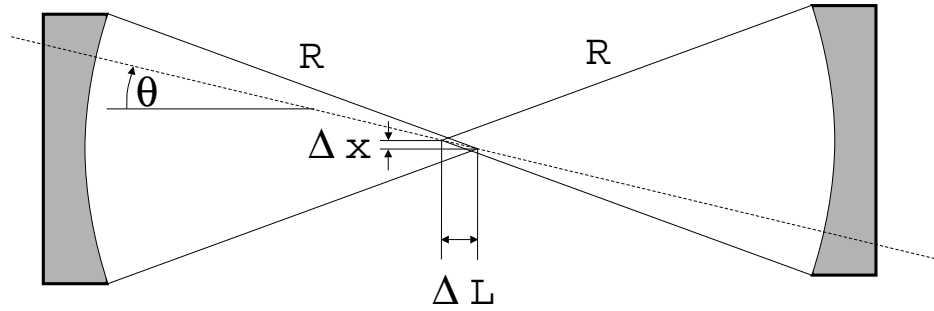


Figure 3.8: Misalignment of one mirror by Δx . The symmetry axis of the mirror curvatures and therefore the light mode is tilted by θ .

where R denotes the mirror radius of curvature. For fixed L (demanded by the size of the trap), the resonator of choice is the near concentric resonator composed of two curved mirrors with a radius of curvature slightly bigger than half the mirror distance L as shown in figure (3.7). Defining $R := (L + \Delta L)/2$, equation (3.19) can be written as:

$$w_0^2 = \frac{\lambda}{2\pi} \sqrt{L \cdot \Delta L} = \frac{L \cdot \lambda}{\pi} \sqrt{\frac{\Delta L}{4L}}. \quad (3.20)$$

For the spot size at the mirrors the expression:

$$w_{mirr}^2 = \frac{L \cdot \lambda}{\pi} \sqrt{\frac{4L}{\Delta L}} \quad (3.21)$$

is valid [54]. From these expressions it is clear that a small waist needs large mirrors and the beam diverges quite strongly. Apart from this, misalignment

of the mirrors of $\mathcal{O}(\Delta L)$ lead to disastrous consequences. Assume a small shift of Δx of one mirror about the symmetry axis shown in figure (3.8). The light mode will tilt through an angle θ :

$$\theta \approx \tan \theta = \frac{\Delta x}{\Delta L}, \quad (3.22)$$

and eventually parts of the beam will hit the edge of the high reflection coatings of the mirrors.

To gain a small mode volume the cavity length should be chosen to be as small as possible. Reduction of the cavity length $L \approx 2R$ is most stringently limited by the size of the trap and contingently by the shielding of the nonconducting mirrors⁴ as well as the necessary access of laser beams.

3.4 Realised Composite System

The parameters that are relevant for the system composed of ion, trap and cavity are the atomic decay rate $\gamma_{\perp} = 2\pi \cdot 0.076$ Hz, the cavity decay rate κ and the coupling g between cavity field mode and ion. κ and g are related to experimental design parameters L , w_0 and \mathcal{F} , the cavity length, waist radius and finesse respectively, by:

$$\kappa = \frac{\pi c}{2\mathcal{F}L}, \quad (3.23)$$

and (for the quadrupole transition $S_{1/2}, m_j = -1/2 \leftrightarrow D_{5/2}, m_j = -5/2$)

$$g = \sqrt{\frac{5c\lambda^2\gamma_{\perp}}{2\pi^2 L w_0^2}}. \quad (3.24)$$

In general κ and γ_{\perp} (or at least one of them) should be small compared to g . From the experimental point of view γ_{\perp} and the transition wavelength λ are fixed for the system at hand. κ can be tuned independently by the finesse \mathcal{F} which depends solely on the quality of the mirrors (see equation (3.15)). With the cavity geometry required to incorporate an ion trap and the resulting spot sizes on the mirrors a finesse of 300000 at 729 nm is a rather optimistic value. Consider now the dependence of g : decreasing the waist radius w_0 increases g without changing κ . As shown in section (3.3), a small cavity waist requires very good alignment of the cavity mirrors. Additionally it is more difficult to center the ion in the waist. Optimistically a waist of

⁴Nonconducting elements near the trapped ion often hold stray charges causing problems concerning the compensation of micromotion.

$w_0 \approx 10 \mu\text{m}$ may be manageable. A change in the cavity length L influences κ and g . Whereas a large $g \propto 1/\sqrt{L}$ requires a small L i.e. a small mode volume, small $\kappa \propto 1/L$ demands a long cavity.

3.4.1 Strong Coupling

In the strong coupling regime it is required that $g \gg \kappa$ and $g \gg \gamma_\perp$. Inserting (3.23) and (3.24) into the first inequality the following relationships are found:

$$\sqrt{\frac{5c\lambda^2\gamma_\perp}{2\pi^2Lw_0^2}} \gg \frac{\pi c}{2\mathcal{F}L} \quad (3.25)$$

$$\Rightarrow L \cdot \left(\frac{\mathcal{F}}{w_0}\right)^2 \gg \frac{\pi^4 c}{10\gamma_\perp\lambda^2} \cong 10^{22} \frac{1}{\text{m}}. \quad (3.26)$$

Inserting the optimistic values for w_0 and \mathcal{F} a limit on L is found:

$$L \gg 10 \text{ m}. \quad (3.27)$$

This is already much too large for a typical quantum optics experiment. For example, the spot size (radius) on the mirrors at 5 m distance is more than 10 cm assuming a 10 μm waist. Inserting (3.24) into the second inequality ($g \gg \gamma_\perp$) yields:

$$\sqrt{\frac{5c\lambda^2\gamma_\perp}{2\pi^2Lw_0^2}} \gg \gamma_\perp \quad (3.28)$$

$$\Rightarrow Lw_0^2 \ll \frac{5c\lambda^2}{2\pi^2\gamma_\perp} \cong 100 \text{ cm}^3. \quad (3.29)$$

Using the previous value for w_0 results in a requirement easy to achieve:

$$L \ll 1000 \text{ km}. \quad (3.30)$$

Combining both conditions it can be seen that it is a rather challenging task to obtain strong coupling to a cavity field on the $S_{1/2} \leftrightarrow D_{5/2}$ Ca^+ transition. The critical condition for obtaining strong coupling to the quadrupole transition is $g \gg \kappa$, whereas the condition $g \gg \gamma_\perp$ is easy to achieve due to the small transition linewidth. This is not true if a dipole transition is coupled

to the cavity field. Consider for example the $D_{5/2}$, $m_j = -5/2 \leftrightarrow P_{3/2}$, $m_j = -3/2$ dipole transition at 854 nm. The transversal decay rate is $2\pi \cdot 790$ kHz, the coupling g_{dip} on this transition is $g_{dip} = 2/\sqrt{5} \cdot g$ [15]. Using this, the equivalent inequality to condition (3.26) becomes:

$$L \cdot \left(\frac{\mathcal{F}}{w_0} \right)^2 \gg 10^{15} \frac{1}{\text{m}}, \quad (3.31)$$

which even for parameters ten times worse than previously (a finesse of 30000 and a waist of 100 μm) results in the requirement that $L \gg 11$ mm; not too difficult to fulfill. The second criterion, the equivalent condition to equation (3.29) concerning the mode volume, is:

$$Lw_0^2 \ll 9 \times 10^3 \text{ mm} \cdot \mu\text{m}^2. \quad (3.32)$$

Obviously small cavities are needed to achieve strong coupling on a dipole transition. It is assumed that the length of a conventional cavity built around a miniaturised ion trap is from around several mm [56] up to a few cm, as used in this work. Inserting $L = 2$ cm into (3.32) means a waist radius $w_0 \ll 21 \mu\text{m}$ is required. Keeping in mind all the other requirements of the entire apparatus this is still a very demanding and challenging condition.

3.4.2 Weak Coupling

If the quadrupole transition is considered as a qubit transition to store and process quantum information [6], it is worthwhile to look for methods to convert the stationary qubit information coherently to a photon that can be sent over large distances. Here, the weak coupling of qubit transition and cavity field in the ‘bad cavity regime’ comes into play. The following conditions must be met:

$$\gamma_{\perp} \ll g^2/\kappa \ll \kappa. \quad (3.33)$$

Using (3.23), (3.24) and realistic parameters for finesse \mathcal{F} , cavity length L and waist radius w_0 , we see that the long-lived quadrupole transition is a good candidate in the ‘bad cavity regime’. The relevant quantity for the system is the cooperativity C , defined in (2.59) as:

$$C := \frac{g^2}{2\gamma_{\perp}\kappa} = \frac{5\mathcal{F}\lambda^2}{2\pi^3 w_0^2}. \quad (3.34)$$

The cavity length L is seen to cancel out and can be chosen freely provided that condition (3.33) remains valid. A high but nonetheless realistic value

for the finesse is 200000, for the cavity waist a radius of 25 μm might be achieved. These values imply $C \approx 14$. The emission rate is enhanced by the Purcell factor $F = (2C + 1) \approx 29$ and the fraction of emission emitted into the cavity mode is $\beta = 2C/(2C + 1) \approx 96\%$.

The remaining case under the condition of weak coupling is defined by the criterion: $\kappa \ll g^2/\gamma_{\perp} \ll \gamma_{\perp}$, this being known as the ‘bad atom regime’. For the quadrupole transition this case is technically not realisable due to the long lifetime of the metastable state.

For the experiment presented here the parameters satisfying the criteria of the weak coupling regime are:

$$\begin{aligned} \text{atomic decay rate} \quad \gamma_{\perp} &= 2\pi \cdot 0.076 \quad \text{Hz} , \\ \text{cavity decay rate} \quad \kappa &= 2\pi \cdot 102 \quad \text{kHz} , \\ \text{ion-cavity coupling} \quad g &= 2\pi \cdot 89 \quad \text{Hz} . \end{aligned}$$

The cooperativity C and Purcell factor F are calculated to be:

$$\begin{aligned} \text{cooperativity} \quad C &\approx 0.51 , \\ \text{Purcell factor} \quad F &\approx 2 . \end{aligned}$$

These parameters are discussed thoroughly in chapter (4).

Chapter 4

Experimental Setup

In this chapter the experimental setup is described. First an overview is given of all the necessary components to trap and investigate single Ca^+ ions in a high finesse cavity. Components such as the lasers, that have been described elsewhere in great detail [11, 10, 9, 57, 58], are only discussed briefly. The parts that are specific to the cavity QED experiment are characterised extensively in the following sections.

4.1 Overview

As shown in figure (4.1), the cavity QED experiment extends over two optical tables, where on the laser table the light sources at 397 nm, 729 nm and 785 nm are mounted. The light is transmitted to the experiment table by optical fibres. The experiment table houses the diode lasers at 866 nm, 854 nm and the photo-ionisation lasers at 423 nm and 390 nm. The vacuum apparatus as the heart of the experiment and the detection devices– the PMT and the CCD-Camera– are located on that table as well.

Cooling Laser at 397 nm [10]

The UV light used for Doppler-cooling and state detection on the $S_{1/2} \leftrightarrow P_{1/2}$ dipole transition is generated by frequency doubling a 794 nm Ti:sapphire laser¹. The Ti:sapphire is locked using Pound–Drever–Hall method (PDH) [59] to a temperature stabilised reference cavity, resulting in a linewidth of about 200 kHz. Frequency doubling is achieved in a commercial LBO doubler² crystal. Pumped with ≈ 1.5 W from the Ti:sapphire it yields ≈ 200 mW UV light power at 397 nm. A power of 3 mW at the fibre output

¹CR-899-21, Coherent, Ar^+ pumped

²Spectra Physics LAS, ‘Wavetrain’

on the experiment table is sufficient for laser cooling of the trapped ion. The wavelength is measured by comparison with a He-Ne-laser (wavemeter) [60] and optionally checked with a hollow cathode Ca discharge lamp signal.

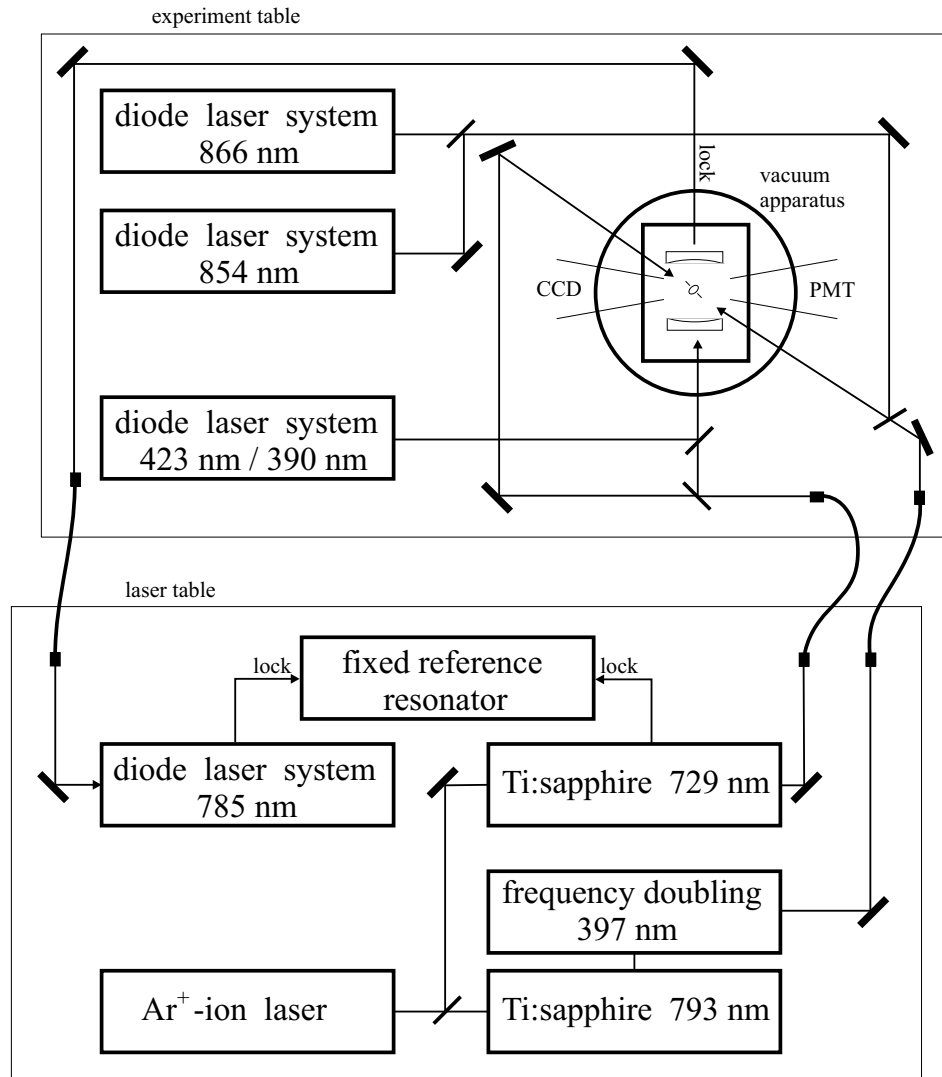


Figure 4.1: Experimental setup. The experiment extends over two optical tables. The laser sources for 397 nm, 729 nm, and 785 nm light are located on the laser table. The light is transmitted to the experiment table by fibres, where the diode laser systems at 866 nm, 854 nm and the ionisation lasers at 423 nm and 390 nm are situated. The vacuum apparatus and the detection units are also located on the experiment table.

Ultrastable laser at 729 nm [11]

For excitations on the narrow quadrupole transition $S_{1/2} \leftrightarrow D_{5/2}$, a very narrow band Ti:sapphire laser³ at 729 nm is used. Stabilisation is achieved by PDH-locking to an evacuated and extensively temperature stabilised (within sub μK , [11]) high finesse cavity ($\mathcal{F} \approx 220000$) and results in a linewidth of about 100 Hz. Typical light power at the experiment table is 25 mW. The wavelength is measured by comparison with a He-Ne-laser (wavemeter) [60] and checked on the ion ('quantum jumps', i.e. excitation to the metastable level \rightarrow no fluorescence, and decay back to the ground state \rightarrow fluorescence [61]).

Diode laser at 785 nm

With the help of the diode laser at 785 nm a transfer lock from the 729 nm cavity to the trap cavity is realised. For this the 785 nm laser is locked to the 729 nm cavity and the trap cavity in turn is locked to the 785 nm light. A double pass AOM configuration allows for fine tuning of the trap cavity length. The procedure is described in section (4.3) in detail.

Diode lasers at 866 nm and 854 nm [57, 58]

The diode lasers at 866 nm and 854 nm are used to repump occupation of the $D_{3/2}$ and the $D_{5/2}$ levels. The frequencies of the lasers are grating stabilised using the Littrow configuration [62, 63]. They are locked using the Pound-Drever-Hall method [59] to temperature stabilised cavities having a finesse of about $\mathcal{F} \approx 1000$, resulting in laser linewidths of ≈ 10 kHz. About 1 mW of light power is sufficient at the trap apparatus. The wavelengths are measured by comparison with a He-Ne-laser (wavemeter) [60] and checked optionally on a hollow cathode Ca discharge lamp (866 nm) or on the ion (854 nm).

Photoionisation lasers at 423 nm and 390 nm [64]

The two step photoionisation light source is composed of laser diodes at 423 nm and 390 nm. The laser at 423 nm excites atomic Ca to the $4p \ ^1P_1$ state (see figure (4.2)). From this level the laser at 390 nm excites further to Rydberg states near the continuum. The Rydberg ion is then field-ionised by the trapping fields. Both laser diodes are grating stabilised by the Littrow technique [62, 63]. Their wavelength is measured by comparison with a He-Ne-laser (wavemeter) [60]. Fine tuning of the more critical 423 nm laser frequency is done with the help of a hollow-cathode Ca discharge lamp. Both laser beams are superimposed on a polarising beam splitter and focused through the ring of the trap. A power of 1.3 mW at 423 nm and

³CR-899-21, Coherent

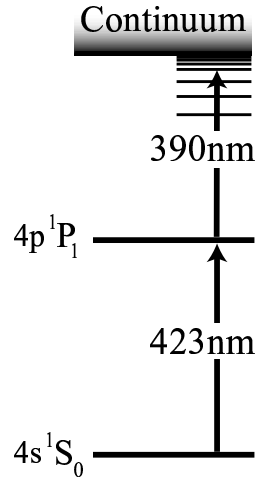


Figure 4.2: Two step photoionisation of atomic Ca. For details see text.

0.6 mW at 390 nm is sufficient to load a few ions into the trap in about one minute at an oven current of 2.1 A.

4.2 Cavity QED Ion Trap Apparatus

To couple a trapped ion to a cavity field mode two different approaches are manifest: one can try to build a miniaturised trap inside a cavity or one can build the trap around a miniaturised cavity. The latter approach demands technologies that enable the fabrication of very small cavity mirrors because the trap itself has to be small to produce sufficiently strong trapping potentials (trapping in the Lamb–Dicke regime). In addition it turned out that nonconducting elements near the ion allow charges to accumulate on their surfaces which in turn strongly disturbs the trapping potential. Taking these difficulties into account the approach adopted was to use a more or less ‘standard’ cavity set up containing a miniaturised Paul–trap. The technological know–how of building a variety of miniaturised ion traps is well–developed in the present group, what is new and demanding is the combination of trap and cavity, the coupling of atom and light mode. This approach limits the minimum cavity length to the centimeter range.

Building a high finesse cavity around a miniaturised Paul–trap in an ultra high vacuum vessel ($p \approx 10^{-10}$ mbar) is a challenging task. The trap

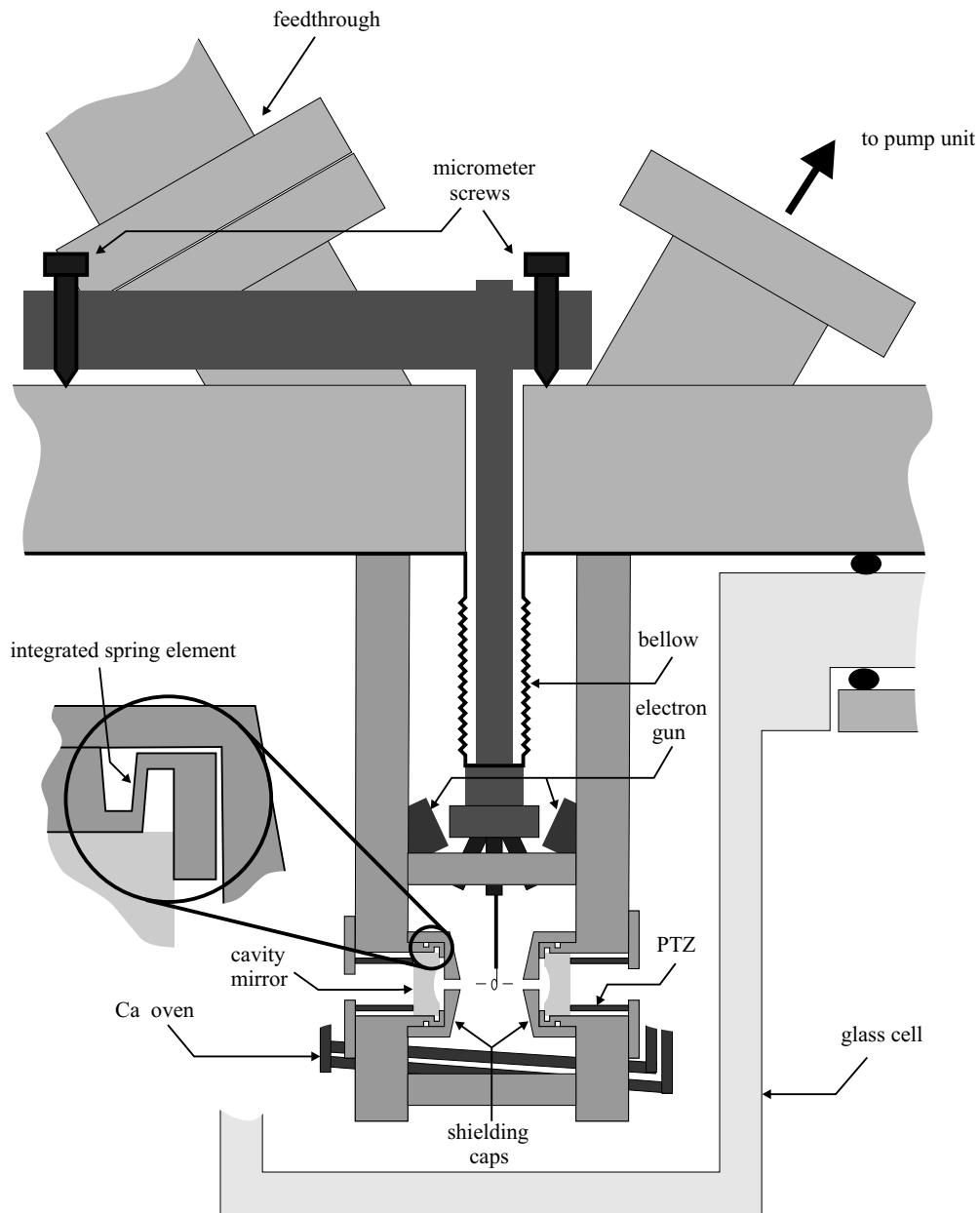


Figure 4.3: Cavity QED vacuum apparatus. All components are mounted on a stainless steel baseplate (248 mm in diameter). Two flanges are welded on the baseplate, connecting pump unit and electrical feedthrough to the vessel. The sketched trap can be moved relative to the cavity by micrometer screws. Wiring and details are omitted for clarity.

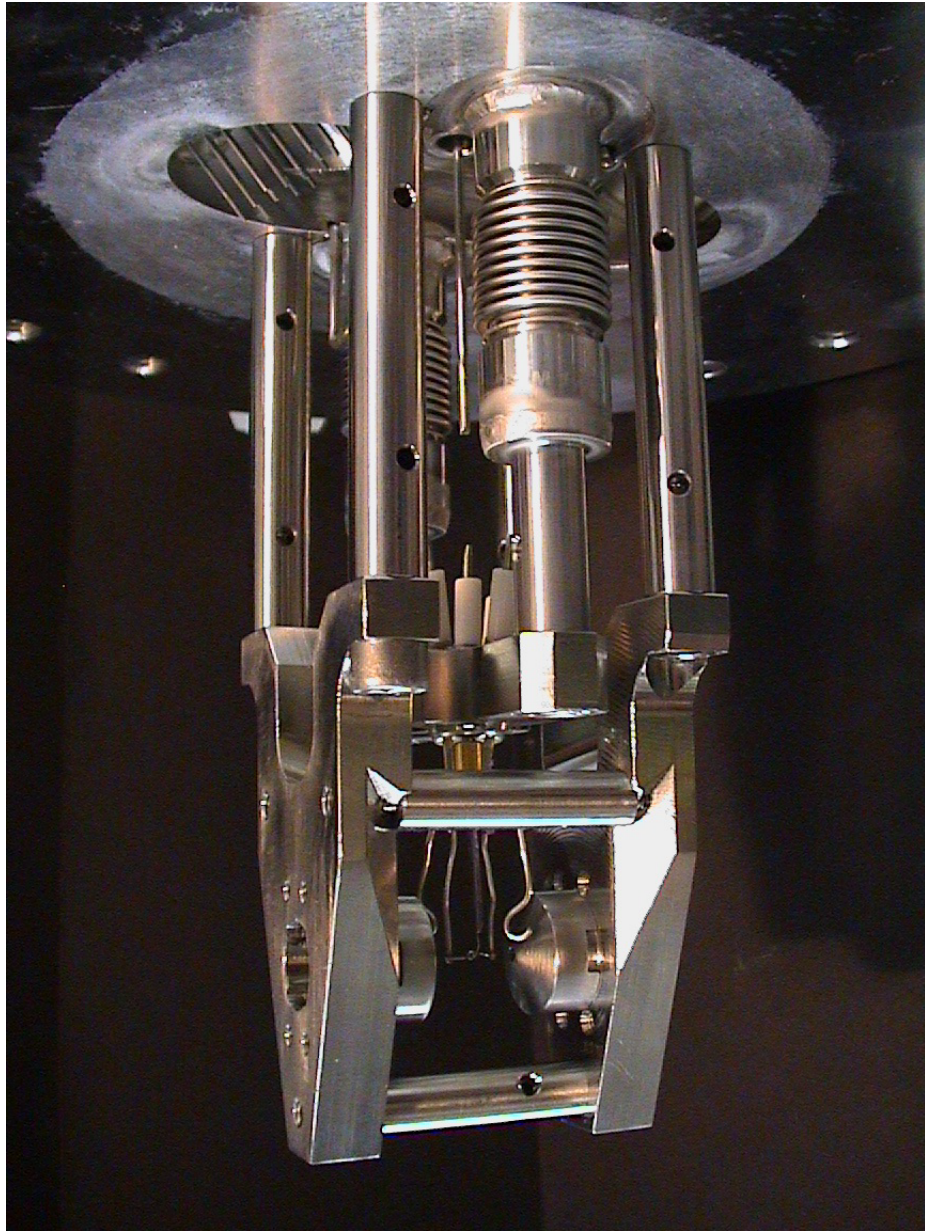


Figure 4.4: Picture of the cavity QED vacuum apparatus during the assembly. The fixed cavity (mounted on 4 posts which are 10 mm in diameter) encloses the maneuverable miniaturised Paul trap (mounted on 2 bellows). Cavity mirrors and piezos, Ca ovens, electron guns and all wiring had still to be mounted when this picture was taken.

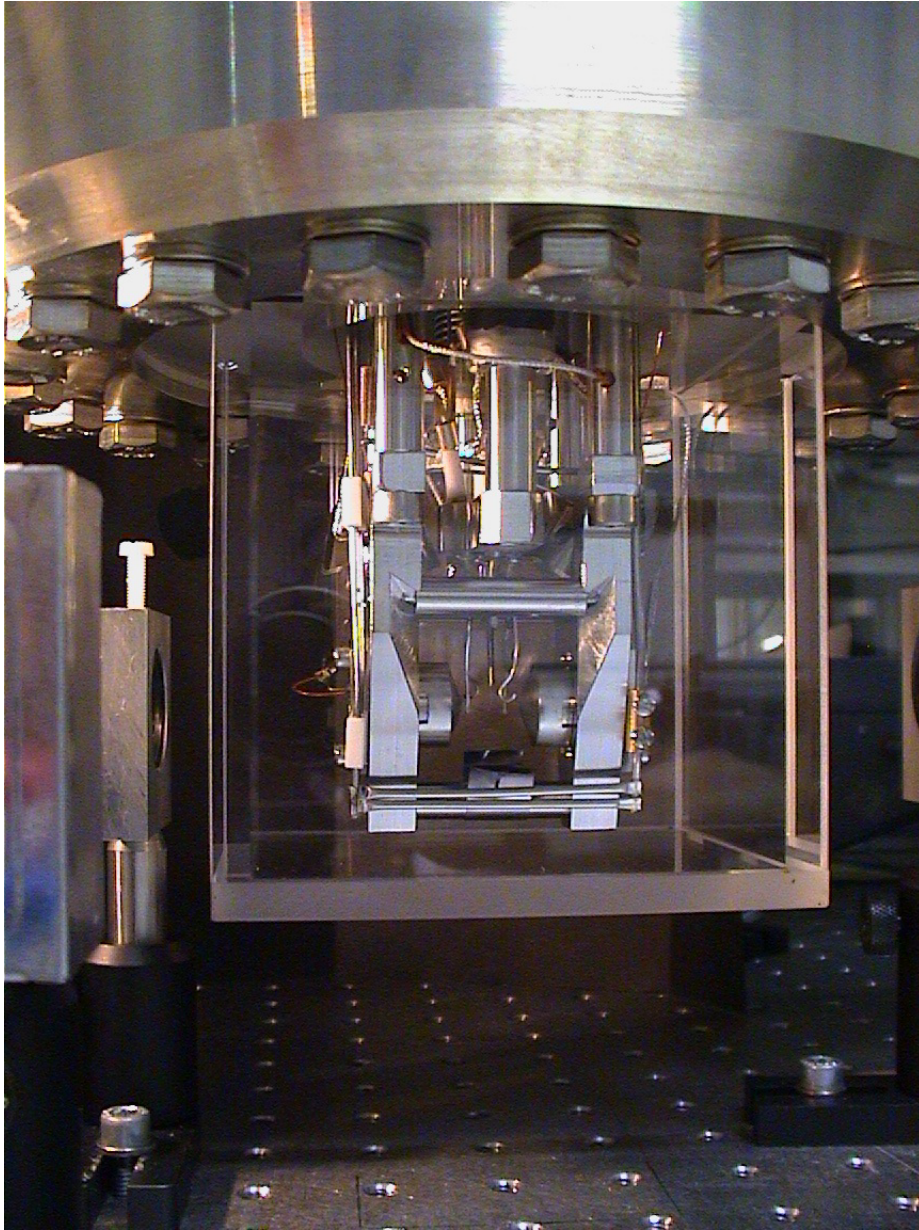


Figure 4.5: Picture of the cavity QED vacuum apparatus after evacuation and bakeout on the optical table. For good optical access, cavity axis and trap are mounted 94 mm above the optical table. The cuboid glass cell and its flange are visible. At the bottom of the cavity mount, the two Ca ovens and the aperture for the atom beam are mounted.

with compensation electrodes, atom oven and electron guns⁴ is complicated enough on its own: however, it has now to be enclosed by the cavity mirrors. Contamination of the mirror surfaces by the atom beam loading the trap has to be prevented. Both mirrors must be aligned very precisely and in order to maintain a high finesse they have to be cleaned just a few minutes before the apparatus is evacuated. Their relative distance has to be piezo controlled to at least half the wavelength. Furthermore, to lock the cavity a sufficiently fast feedback-control is necessary. In addition to that, trap or cavity must be movable to center the ion in the cavity waist. Drifts and vibration amplitudes should be kept as low as possible. Besides the complicated wiring in the vacuum itself, the control and operation of one component must not act on another or on the ion itself. Changing electro-magnetic fields due to currents, voltages and/or fluctuating charges on nonconducting parts has to be strictly avoided at the place of the ion.

In a previous experimental setup [10] as shown in figure (4.6), a quartz spacer was used to define the distance of the cavity mirrors. It was found that drifting charges on the nonconducting quartz⁵ and/or on the mirrors itself made it impossible to compensate the micromotion. In addition it was not

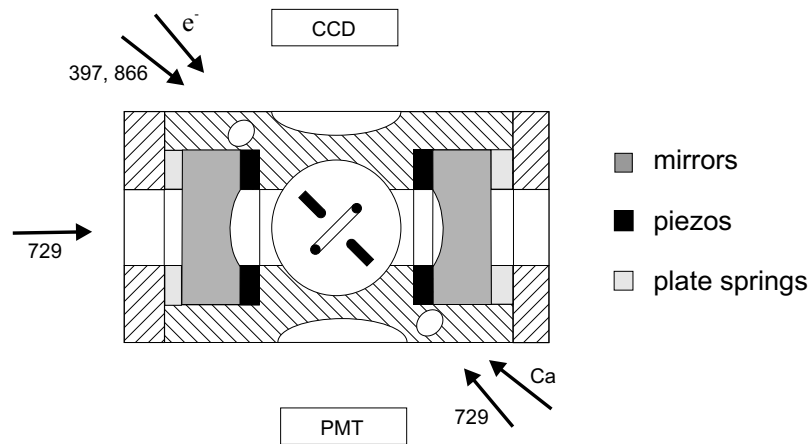


Figure 4.6: Previous experimental setup. The moveable trap (not drawn to scale, ring diameter ≈ 1.6 mm) is placed into a quartz spacer separating the cavity mirrors (mirror separation 21 mm). Piezo stacks and plate springs allow for tuning of the cavity length. Drawing taken from [10].

⁴Before the photoionisation lasers were set up, the ionisation of atomic Ca was achieved by impact ionisation.

⁵Coating the spacer with a conducting graphite solution (Aquadag, Achseson Industries) did not help.

possible to trap single ions reliably for a sufficiently long time (\sim a day) due to the maximally allowed bakeout temperature of the piezo stacks (120°C) and the resulting poor background gas pressure. Furthermore, the cavity piezos were located on the trap-facing side of the mirrors. Changing the piezo voltage (up to ≈ 400 V) resulted in a huge shift (≈ 15 μm) of the ion. Finally, the operation of atom oven, electron gun and the RF-drive of the trap strongly influenced the mirror distance i.e. the cavity resonance.

Therefore, the goal of a new setup was to overcome these experimental difficulties. The apparatus described in the following suffers from none of the drawbacks encountered with the previous setup just described.

4.2.1 Vacuum Vessel

For the vacuum apparatus a new construction was proposed consisting of a cuboid glass cell⁶, being flanged to a baseplate providing trap and cavity as well as all other necessary components. The advantages of this concept were the optical access from almost all directions (except the edges) and the idea that, first having the apparatus assembled and aligned outside vacuum, the glass cell then simply has to be mounted.

Unfortunately, the glass cell concept had serious drawbacks. The windows could not be anti-reflection coated which results in a high straylight level. Additionally, the construction, the assembly, or the wiring of trap, mechanics, oven, electron guns⁷, cavity mirrors and piezos is complicated due to the limited space of the single 80 mm diameter wide opening of the glass cell. This together with the fact that it was not possible to seal the glass cell and the base plate properly during the first attempt, led to the insight that the glass cell concept is not to be recommended in the near future.

4.2.2 Maneuverable Paul Trap

Figure (4.3) shows a schematic drawing of the apparatus, figures (4.4) and (4.5) show photos taken during the assembly. The trap (see figure (3.6)) is a slightly elliptical ring with average diameter of ≈ 1.4 mm made of 0.2 mm thick molybdenum wire. It is fabricated by bending the thin wire around a thicker wire having ≈ 1.2 mm diameter and closing the arising ring by spot-welding. It is then cleaned and smoothed by an electro-chemical process. The endcaps are also made of 0.2 mm thick molybdenum wire and are spaced by ≈ 1.2 mm. The tips are rounded, cleaned and smoothed with the same

⁶Hellma, Müllheim

⁷ES-015 BaO-Disc Cathode, tectra GmbH, Frankfurt

techniques used on the ring. Together with two compensation electrodes the trap is mounted on a bar which is flexibly connected by bellows (suitable for UHV) to the baseplate. A rigid construction outside the vacuum joins the bar to a mirror holder-like mount that can be precisely adjusted by means of three micrometer screws.

4.2.3 Electrical Connections

The RF Paul-trap is driven with a radio frequency⁸ of ≈ 28 MHz. To avoid influencing other components and to keep losses low, a single pin feedthrough is welded in the center of the baseplate connecting the ring of the trap straight to the helical resonator [65], which has a quality factor of ≈ 370 . The helical resonator is fed with a power between 0.3 W and 1 W provided by a 5 W amplifier⁹. If 1 W RF power is exceeded, stable and reliable trapping of ions seemed not to be possible, the ions are lost quickly within seconds.

Apart from the trap RF drive, all other electrical connections are established by a 20 pin feedthrough¹⁰ as there are: 4 trap compensation voltages, 2 piezo voltages and the 2 associated piezo masses¹¹ (total 4), 2 electron gun heating currents and the associated common mass (total 3), 1 electron gun acceleration voltage and 2 oven heating currents (each on two pins for less resistance). To avoid any electronics picking up the RF drive frequency, all connections except that of the piezos are low pass filtered at the feedthrough.

Inside the vacuum vessel the electrical connections are made using kapton isolated wire¹² and welding wire (stainless steel). The inner conductor of the coaxial cable is used to connect all components except the trap electrodes. These are connected with the shielding cord (inner conductor removed) because the flexibility of the cord allows the trap to be moved.

4.2.4 Cavity Mount and Cavity

To meet the criteria stated in the introduction of this chapter, the cavity mount was constructed from stainless steel. The mirrors have a separation of $L = 21$ mm and a radius of curvature of 25 mm. Initially it was planned to use mirrors with 12 mm radii of curvature resulting in a $30 \mu\text{m}$ waist radius.

⁸Synthesised function generator DS345, Stanford Research Systems

⁹ZHL-5W, Mini Circuits

¹⁰HV-10Q-20-C40 Power feedthrough, Caburn MDC

¹¹We decided to have both piezo masses isolated from each other and from ground to have more flexibility in driving the piezos (for example, to have the slow and the fast branch of the cavity lock on different cables).

¹²KAP3, kapton wire 4 kV 1/0.25 mm coaxial, Caburn MDC

Due to incorrect labelling the mirrors with 25 mm radius of curvature were used from the beginning leading to an uncritical near confocal cavity but also to a weaker coupling g . On the other hand the near concentric setup would have been much more sensitive to misalignment as discussed in chapter (3) section (3.3), so it is not clear if the error was actually beneficial. The mirrors are covered by steel caps leaving only a 2 mm diameter hole for the cavity mode, which has 54 μm waist radius. The caps ensure that electric fields due to charges on the mirror surfaces as well as from the high voltage on the piezo tubes do not extend to the position of the ion. An additional advantage is that the mirrors are shielded from the Ca oven beam. The axial position of both mirrors can be controlled via piezo ceramic tubes¹³. Increases in the lengths of the piezos move the mirrors which press against springs that themselves hold the mirrors in place (cf. encircled inset in figure (4.3)). The piezo tubes are centered and insulated on both ends with MACOR plates. A potential of up to 500 V can be applied and leads to a *contraction* of the

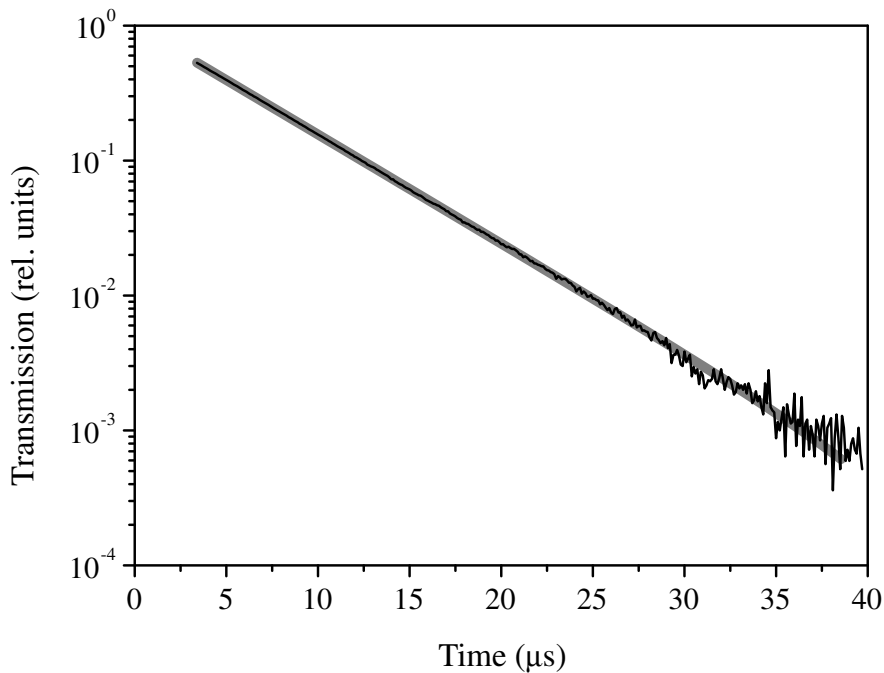


Figure 4.7: Exponential decay of the filled cavity with time constant $\tau = (5.38 \pm 0.004) \mu\text{s}$ measured after the first bakeout. The thin line is the measured transmission. The thick line is the exponential fit. Calculated finesse: $\mathcal{F} = 241300 \pm 170$.

¹³Physical Instruments Ceramic, D-07589 Lederhose, Germany

piezos. With the high voltage source providing up to ≈ 330 V, it is possible to shift each mirror about one free spectral range (≈ 400 nm). This is a third of the range one would expect from the bare piezo tubes and is probably due to the relatively high spring tension.

By measuring the decay of the filled cavity¹⁴ we calculated the finesse \mathcal{F} to be ≈ 240000 after the first bakeout (figure (4.7)). Due to sealing problems (baseplate/glasscell) the bakeout had to be repeated and unfortunately this led to a severe degradation in finesse, down to ≈ 35000 . All experiments described in this thesis were performed with this lower finesse. With a finesse $\mathcal{F} = 35000$ and waist radius $w_0 = 54 \mu\text{m}$ the parameters g and κ are calculated to be (cf. section 3.4):

$$\kappa = \frac{\pi c}{2\mathcal{F}L} = 2\pi \cdot 102 \text{ kHz}, \quad (4.1)$$

$$g = \sqrt{\frac{5c\lambda^2\gamma_{\perp}}{2\pi^2 L w_0^2}} = 2\pi \cdot 89 \text{ Hz}, \quad (4.2)$$

from which the experimentally important parameters cooperativity C and Purcell factor F can be deduced:

$$C := \frac{g^2}{2\gamma_{\perp}\kappa} = 0.51, \quad (4.3)$$

$$F := 2C + 1 \approx 2, \quad (4.4)$$

and the fraction of light emitted into the cavity mode, given by β , becomes:

$$\beta := 2C/(2C + 1) \approx 0.5. \quad (4.5)$$

Compared to the parameters planned and discussed in chapter (3), we can expect only a small effect of the cavity. Nevertheless it is sufficiently large to be measurable.

4.2.5 Beam Directions and Magnetic Field

In our experiment we generally prepare the ion in the electrical ground state by pumping into the $S_{1/2}$, $m_j = -1/2$ level (cf. chapter (3) section (3.1.2)). We choose a configuration of magnetic field \mathbf{B} , beam direction \mathbf{k} and polarisation \mathbf{e} where we get highest coupling efficiency to the cavity on the $S_{1/2}$,

¹⁴The cavity is scanned slowly over resonance and fills with light. On maximum transmission the light is switched off by an AOM and the exponential decay of the transmitted light is recorded on a sufficiently fast photodiode.

$m_j = -1/2 \leftrightarrow P_{5/2}, m_j = -5/2$ transition i.e. $\mathbf{e} \perp \mathbf{B} \perp \mathbf{k}$. All other transitions except the $S_{1/2}, m_j = -1/2 \leftrightarrow P_{5/2}, m_j = 3/2$ transition are suppressed in this case (cf. chapter (3), figures (3.2) and (3.3)). The exact geometric orientations of all optical beams and detection devices are as follows: cavity axis, symmetry axis of the trap and the photomultiplier detection channel lie in the plane of the table. The detection channel for the CCD-camera subtends an angle of $\approx 9^\circ$ with the plane of the table. Neglecting this small angle, PMT and CCD face each other. The cavity axis is perpendicular to PMT and CCD. The symmetry axis of the trap itself lies at an angle of $\approx 45^\circ$ to the cavity axis (and therefore also to PMT and CCD light channel). All light beams except the 397 nm σ -beam lie in a plane spanned by

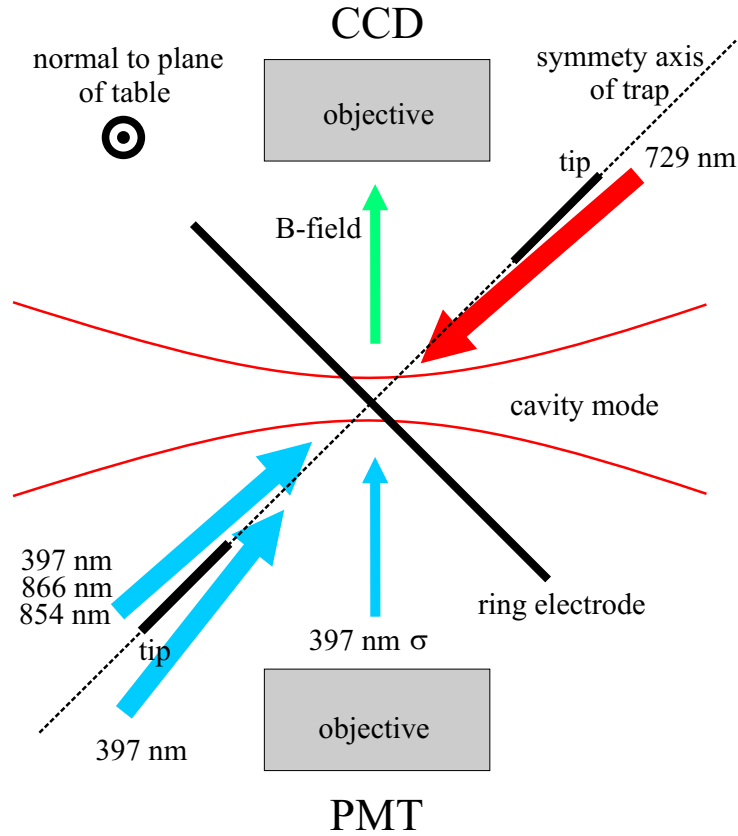


Figure 4.8: Top view of beams and trap. The cavity waist as well as ring and endcaps of the trap are sketched schematically. All beams except the 397 nm σ -beam lie approximately in a plane. The magnetic field is chosen perpendicular to the cavity axis.

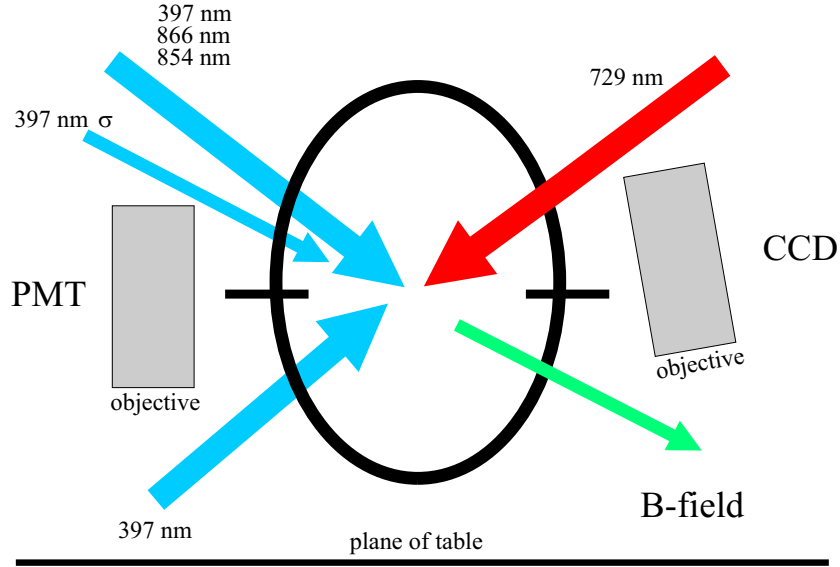


Figure 4.9: View of trap and beams in direction of the cavity axis. The CCD-camera light channel is slightly tilted off the plane of the table to save mirrors on the way to the camera which is mounted on a higher level.

the symmetry axis of the trap and the normal to the plane of the table. A cooling beam at 397 nm and the light at 866 nm and 854 nm is sent from above through the trap, at an angle of $\approx 30^\circ$ to the plane of the table. From below, a second cooling beam is focused into the apparatus at an angle of $\approx 36^\circ$ to the plane of the table. The 729 nm beam enters from the opposite direction and subtends an angle of $\approx 31^\circ$ with the plane of the table. To get coupling of the $S_{1/2}, m_j = -1/2 \leftrightarrow D_{5/2}, m_j = -5/2$ transition independent of the polarisation of the cavity mode, the magnetic field \mathbf{B} is chosen to be perpendicular to the cavity axis at an angle of $\approx 27^\circ$ to the plane of the table. This is exactly the direction of the 397 nm σ -beam.

The magnetic field \mathbf{B} at the position of the ion is generated by one main coil and two smaller coils. The field of the main coil is already aligned with the direction of the 397 nm σ -beam. The smaller coils serve to compensate static magnetic stray fields such as, for example, the earth's magnetic field which is not parallel to the field generated by the main coil. Due to the compactness of the glass cell, the coils could be mounted near the trap and therefore a current of less than 100 mA is sufficient to generate a magnetic field of ≈ 3 Gauss. Constant current sources for these low currents are easily available.

The magnetic field should be chosen in such a way that the quality of

the Doppler cooling on the $S_{1/2} \leftrightarrow P_{1/2}$ transition is not affected by the Zeeman splitting of the levels involved. At the same time however, the Zeeman splitting of the $S_{1/2} \leftrightarrow D_{5/2}$ levels should split the relevant spectral lines so that they are clearly resolved. For trap frequencies $\omega_x = 2\pi \cdot 2.9$ MHz, $\omega_y = 2\pi \cdot 3.9$ MHz and $\omega_z = 2\pi \cdot 7.4$ MHz at ≈ 1 W RF feeding power a magnetic field of ≈ 3 Gauss meets these criteria, splitting the $S_{1/2}, m_j = -1/2 \leftrightarrow D_{5/2}, m_j = -5/2$ carrier transition by ≈ 5 MHz from the $S_{1/2}, m_j = -1/2 \leftrightarrow D_{5/2}, m_j = -3/2$ carrier.

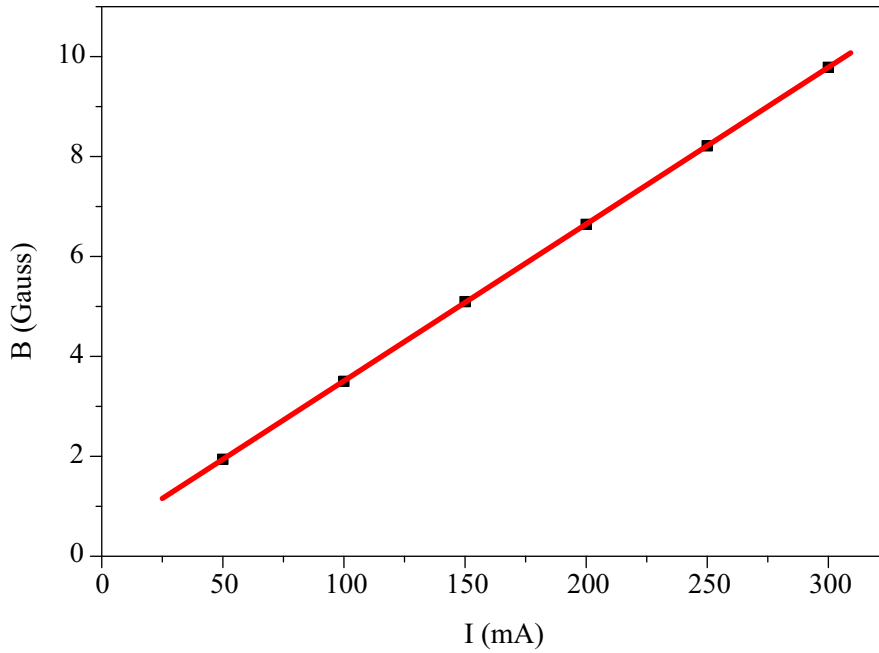


Figure 4.10: Magnetic field B at the place of the ion versus current I through main coil. The field has been measured by observing the splitting between the carriers of the $S_{1/2}, m_j = -1/2 \leftrightarrow D_{5/2}, m_j = -5/2$ and the $S_{1/2}, m_j = -1/2 \leftrightarrow D_{5/2}, m_j = -3/2$ transitions.

4.3 Transfer Diode Laser at 785 nm

In order to study stationary coherent interaction of an atom and a cavity mode it is necessary to stabilise the cavity resonance frequency to the atomic transition frequency. In order to avoid that resonant 729 nm light being present in the cavity which would perturb the controlled atom–cavity interaction, we use a 785 nm diode laser for the stabilisation since its frequency

is far off-resonance from transitions at 729 nm. This diode laser and the transfer lock are essential for experiments on coherent ion-cavity interaction and are therefore described thoroughly in the following section.

4.3.1 Setup

A sketch of the setup of the 785 nm laser is shown in figure (4.11). A single mode laser diode¹⁵ is mounted in a housing¹⁶ containing the collimation objective, Peltier elements and a temperature sensor. The laser diode is temperature stabilised to within a few millikelvin. An external holographic

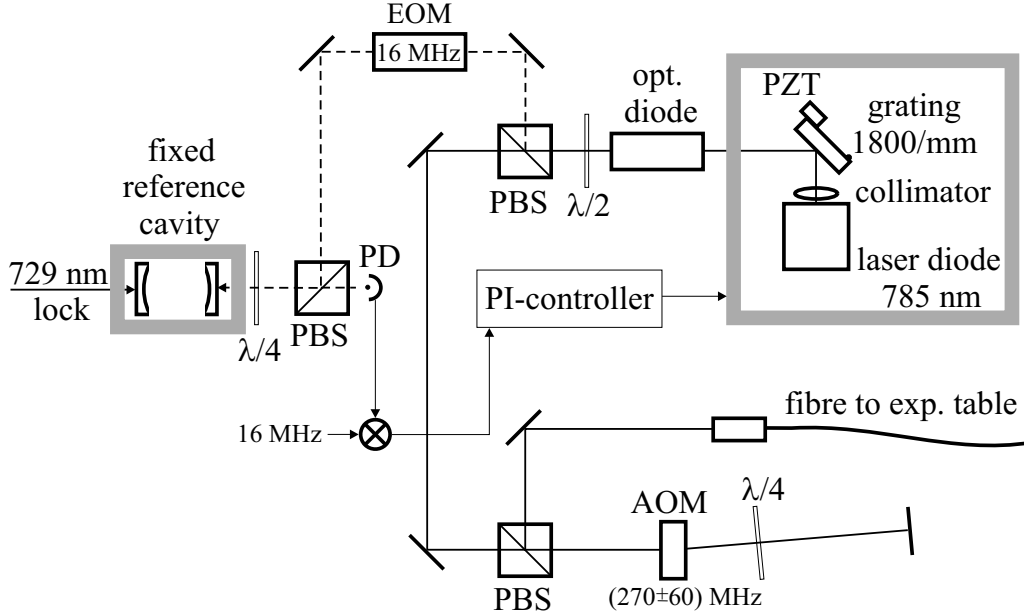


Figure 4.11: Setup of the 785 nm diode laser. Laser diode, collimator and grating (Littrow configuration [62, 63]) are mounted in a stable aluminium box. The beam (≈ 35 mW) is split into a lock beam (≈ 2 mW, dashed line) and a beam being frequency shifted in a double pass configuration and sent to the experiment (solid line). The lock beam passes through an EOM driven at 16 MHz and is coupled into the same reference cavity that is used to stabilise the 729 nm laser. A Pound–Drever–Hall error signal is obtained and processed in a PI-controller acting on laser diode current and grating piezo. Laser linewidth: $\Delta\nu_{785} = (1.8 \pm 0.1)$ kHz.

¹⁵DL-7140-001, 80 mW maximum output power, TOPTICA Photonics AG, Martinsried

¹⁶Schäfter + Kirchhoff GmbH, Hamburg

grating¹⁷ with 1800 lines/mm in Littrow configuration [62, 63] creates an extended tuneable resonator. The grating is mounted on a precision mirror holder, fine tuning is done by a piezo. The elements described so far are enclosed in a stable aluminium case kept at a constant temperature of $(20 \pm 0.1)^\circ\text{C}$ by circulating water. After passing through an optical diode¹⁸ with 60 dB isolation the light is split by a polarising beam splitter. The part of the light being used for the Pound–Drever–Hall (PDH) lock to the reference cavity is phase modulated with an EOM¹⁹ at 16 MHz and a PDH error signal is obtained [59] (see figure (4.12)). This error signal is fed to a PI-controller acting on the laser diode current (fast branch) as well as on the grating–piezo (slow branch). The light not being used for the lock is directed twice through an AOM (double pass) allowing for an overall continuous frequency shift of $\approx \pm 120$ MHz. After that it is coupled into a fibre and sent to the experiment table. Less than 1 mW of light is sufficient for stabilising the trap cavity.

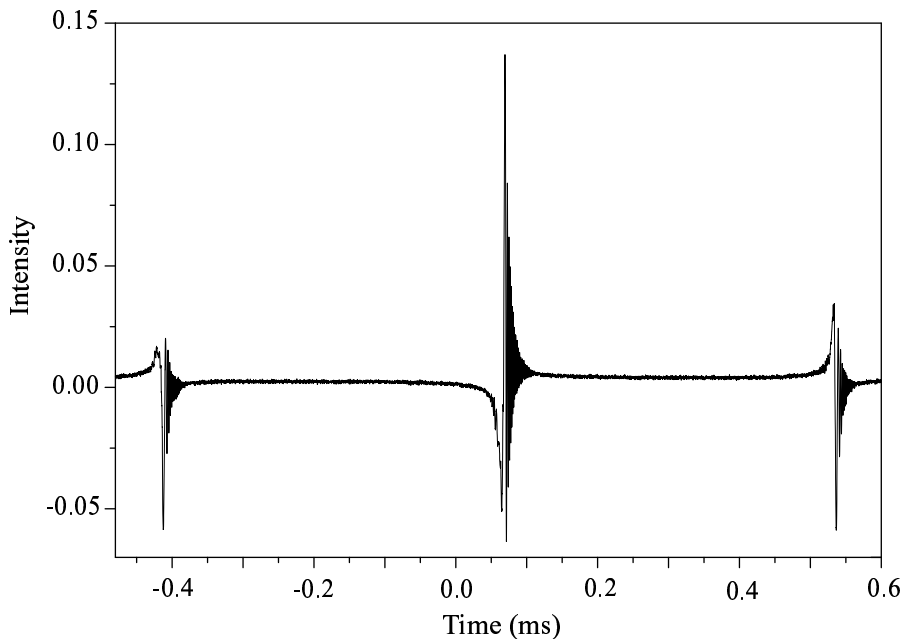


Figure 4.12: Error signal obtained by scanning the laser via the grating over the resonance of the reference cavity. Due to the fast scan rate (as compared to the cavity decay rate), incoming light interferes with the light stored in the cavity, leading to the observed ‘ringing’.

¹⁷Zeiss Optik, Jena

¹⁸LINOS Photonics GmbH, Göttingen

¹⁹KD*P, LINOS Photonics GmbH, Göttingen

4.3.2 Linewidth of the Laser at 785 nm

To determine the linewidth of the laser it is essential to know the linewidth of the cavity it is locked to. The cavity linewidth can be calculated from the cavity finesse \mathcal{F} as was measured in [11] to be roughly 14000 (@ $\lambda \approx 785$ nm) by determining the decay time of the cavity. In this thesis an accurate method for measuring the cavity linewidth using the error signal is described. By tuning the external grating, the laser is scanned over the reference cavity resonance and the error signal is recorded. By comparing the central peak of the error signal with a numerical simulation [66, 67], finesse \mathcal{F} and scanrate ν_ω [66, 67] are determined (cf. figure (4.13)) to be $\mathcal{F} = 16500 \pm 1000$ and

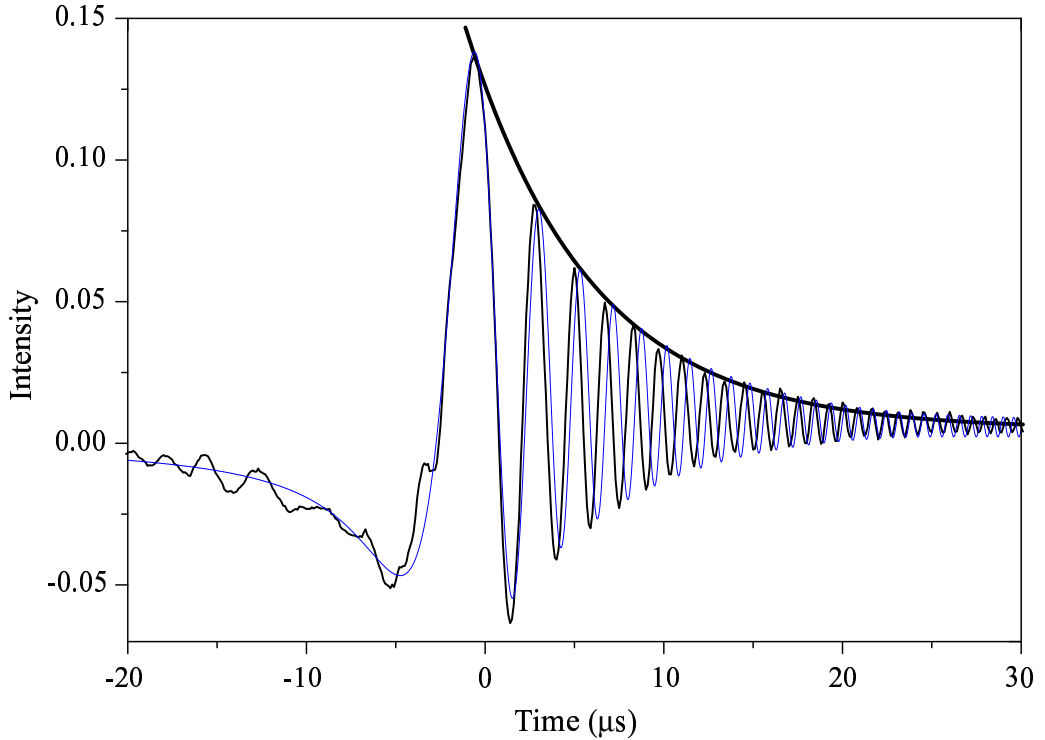


Figure 4.13: Central peak of the error signal. From the exponential decay (thick solid line) of the oscillations the finesse $\mathcal{F} = 16500 \pm 1000$ can be calculated. (This has been done for several scans to obtain the given value and its error). The simulation (thin line) uses the above finesse and a scan rate of $\nu_\omega = 15.8$. The amplitude has been normalised to fit the experimental data. Deviations of experiment and simulation are probably due to varying scan velocity caused by the grating piezo.

$\nu_\omega = 15.8 \pm 0.7$. The normalised scanrate ν_ω is defined as the scanrate in units of half of the cavity linewidth ($\Delta\nu_{cav} = c/(2\mathcal{F}L)$) per cavity energy storage time τ :

$$\nu_\omega := \frac{2\mathcal{F}L\dot{\omega}\tau}{\pi c}, \quad (4.6)$$

where L is the cavity length. From the finesse \mathcal{F} a cavity linewidth $\Delta\nu_{cav} = (45 \pm 2.5)$ kHz is calculated. From the comparison of error signal amplitude when scanning the laser slowly over the cavity resonance and rms amplitude when the laser is locked we can estimate the laser linewidth by approximating the central part of the error signal by a straight line. Usually the actual error signal is even steeper in the range where the laser is locked and therefore this analysis results in a conservative value for the linewidth. For the transfer-lock laser we obtain: $\Delta\nu_{785} = (1.8 \pm 0.1)$ kHz.

4.4 Cavity Stabilisation

The laser at 785 nm allows the trap cavity to be resonant with light at 729 nm without having this light present in the cavity. The basic scheme of the transfer lock is as follows: we frequency-lock the 785 nm diode laser to the same ultra-stable reference cavity (cf. [6]) as the 729 nm Ti:sapphire laser. By stabilising the trap cavity to the diode laser frequency, the lengths of reference and trap cavity are fixed relative to each other. Furthermore, the length of the trap cavity is fixed relative to the wavelength of the 729 nm Ti:sapphire laser. By choosing a convenient longitudinal mode of the 785 nm laser and applying an appropriate frequency shift to the diode laser light, the length of the trap cavity is adjusted until the cavity is resonant with the 729 nm light. Taking into account a thermal expansion coefficient for the trap cavity mount (steel, piezo ceramics) of $10^{-5}/\text{K}$, a temperature change of less than 2 K already results in a resonance shift of one free spectral range (≈ 7 GHz) of the trap cavity. In this case, a different longitudinal mode for the diode laser has to be found to stabilise again using this double resonance scheme. Nevertheless it turned out that a cavity drift of one free spectral range does not occur very often (about 3 times in 10 experimental runs) leaving a long enough time to perform experiments.

4.4.1 Setup

A sketch of the trap cavity setup is given in figure (4.14). The stabilised 785 nm light leaving the fibre is phase modulated by an EOM²⁰ driven at 16 MHz and is coupled into the trap cavity via a polarising beam splitter. The 729 nm light is coupled into the cavity from the opposite side. The reflected 785 nm light is dispersed by a grating (1200/mm) to separate it from the 729 nm transmission light being monitored with a CCD camera and a photodiode. The first order grating reflection at 785 nm is focused on a fast photodiode²¹ to obtain a Pound–Drever–Hall error signal after mixing with the modulation frequency. The error signal is processed in a PI-controller

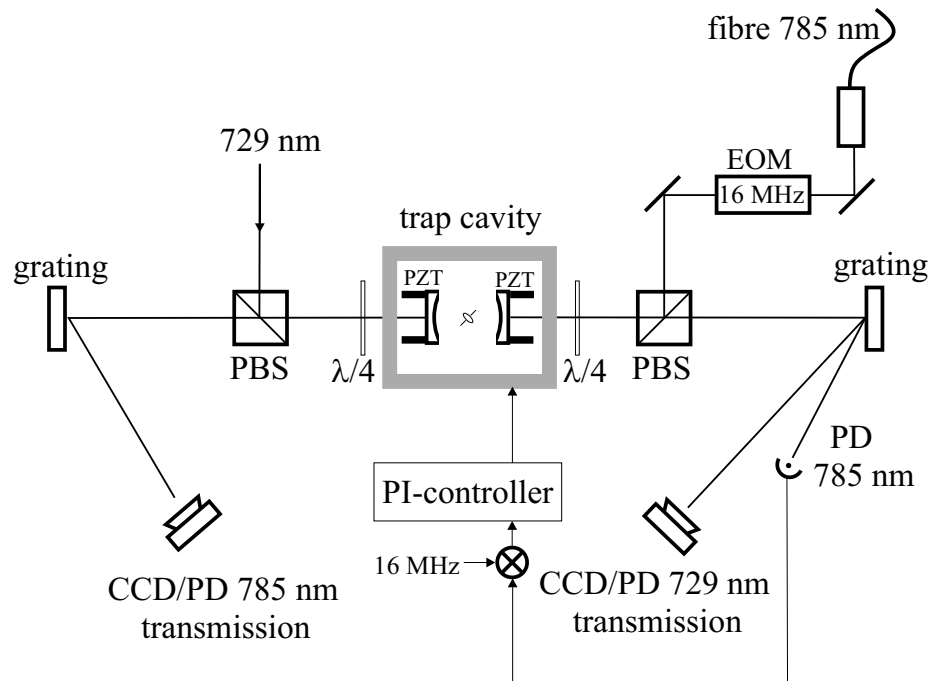


Figure 4.14: Setup of the trap cavity lock. The light at 785 and 729 nm is coupled into the cavity from opposite directions in a symmetric way. Gratings (1200/mm) on both sides separate the beams and ensure control of the transmitted power at both wavelengths without perturbation by reflections of the other light. The 785 nm light is phase modulated and with the standard techniques a Pound–Drever–Hall error signal is obtained to lock the trap cavity to the 785 nm light. Lenses are omitted for the sake of clarity.

²⁰KD*P, LINOS Photonics GmbH, Göttingen

²¹New Focus 1801-FS, 125 MHz

acting on one of the trap cavity piezos. By changing the offset-voltage of the other piezo, the standing wave pattern can be shifted relative to the ion. On the side that the 729 nm light is coupled in, a grating is again used to separate the transmitted 785 nm from reflected 729 nm light. The 785 nm transmission is monitored with a CCD as well as with a photodiode.

4.4.2 Establishing the Transfer Lock

The experimental procedure to achieve double resonance of the trap cavity with the 785 nm and the 729 nm lasers is as follows: by scanning the trap cavity, transmission on the 729 nm TEM₀₀ mode is recorded (due to the scan range of the trap cavity being limited to about one free spectral range, there is only one such mode). Now the wavelength of the diode laser has to be chosen in such a way that the 785 nm light is also resonant for both the reference and the trap cavity within the range of ± 120 MHz being covered by the double pass AOM. Usually, this can be achieved by tuning the diode current and thereby selecting one of the diode's longitudinal modes. Finding a convenient longitudinal mode is substantially aided by the robust lock of the 785 nm laser diode over a diode current range from ≈ 60 mA up to ≈ 105 mA and the ability to lock the trap cavity using a very low light level (down to ≈ 10 μ W). Having found a convenient mode, the 785 nm diode laser can be locked onto the reference cavity. The trap cavity is then locked onto the 785 nm diode laser. It is now also stabilised resonantly with the 729 nm light.

Chapter 5

Preparations for Single Ion Cavity QED

A precondition for the controlled interaction of a single ion with a single electric field mode is the mastery of the two individual systems. Whereas the operation of the cavity is explained in chapter (4) section (4.4), the focus of this chapter is on the preparation and control of the remaining constituent, the single ion. After giving a basic overview of the experimental procedures, some results are presented that characterise the trap and confirm that the trapped ion is well controlled.

5.1 General Procedure of the Experiments

The experiment is run in two different modes. In the continuous mode, all lasers can be switched on and off by hand. The fluorescence rate is measured for a fixed time (usually $100 \mu\text{s}$) and displayed continuously. This mode is used to load the trap, get rid of unwanted ions (if a cloud or too many ions are loaded) and to improve Doppler cooling. It is also used for almost all alignment procedures as well as micromotion compensation [10].

The actual experiments are performed in the pulsed mode. The general procedure for this mode is as follows:

- The ion is cooled via Doppler cooling and prepared in some ‘starting’ state (usually the electronic ground state).
- Then a pulse sequence is applied to the ion.
- After that the electronic state is detected.

This sequence is repeated 20, 100 or 200 times and the average excitation rate to the $D_{5/2}$ level is calculated. After that, changes in the excitation procedure can be applied and another set of experiments are triggered.

5.1.1 Preparation of a Single Ion

To trap ions in the first place, only the Doppler cooling laser at 397 nm and the repumper laser at 866 nm are necessary. The correct wavelength of both lasers is checked using a wavemeter [60], additionally a hollow cathode signal can be used. Whereas the 866 nm laser is tuned to be on resonance, the cooling laser at 397 nm has to be red-detuned by about 900 MHz¹ for loading. The light power in both beams should be about 1 mW to obtain sufficient signal even if the beams are slightly misaligned. The trap is switched on at about 0.5 W RF power (or even lower if one wants to trap large clouds). The RF frequency has to be checked from time to time to make sure it is still resonant with the helical resonator. This is done by ensuring the reflected power is minimised. If the ionisation laser beams are at the correct wavelength and roughly focused through the trap center, the Ca oven can be turned on at ≈ 2 A (few ions, for large clouds up to ≈ 3 A). To load ions it takes between 1 and 3 minutes. If no loading occurs in this time, the ionisation laser beams may not be centered on the trap or not be properly superimposed. If ions are trapped, the first step is to stabilise and improve the signal by choosing the right detuning for efficient Doppler cooling. The signal-to-noise ratio must be maximised by centering the laser beams on the ion. Eventually the light power should be reduced below saturation. Having trapped ions, the spatial and spectral matching of the laser beams at 729 nm and 854 nm can be checked. The number of trapped ions can now be reduced by blocking the repumper (866 nm), the ions heat up and if one is fortunate only one ion remains (in our case we always performed experiments with a single trapped ion). With the micromotion compensation techniques described extensively in [10], the ion is shifted to the trap center where the micromotion vanishes. During this procedure it is helpful to check the line-shape on the Doppler transition repeatedly and adjust the detuning as the line width narrows due to better cooling. Eventually all laser beams have to be centered again on the ion. In the end one is left with a single or few ions cooled near to the Doppler limit and one can start the pulsed spectroscopy experiments.

¹The detuning can be chosen smaller (contingently down to a few linewidths $\Gamma \approx 20$ MHz) if the beams are already aligned perfectly and only single ions are to be trapped.

5.1.2 Pulsed Spectroscopy

For the pulsed spectroscopy the ion is cooled via Doppler cooling on the $S_{1/2} \leftrightarrow P_{1/2}$ transition for 1.9 ms. During this time the 854 nm laser is switched on to remove any population in the metastable $D_{5/2}$ state. In addition, the ion is irradiated with a laser at 866 nm at all times to prevent shelving in the metastable $D_{3/2}$ state. At the end of this cooling pulse the ion is optically pumped into the $S_{1/2}$, $m_j = -1/2$ Zeeman sub-level by applying a 0.1 ms long σ -polarised pulse on the same transition. After that, all light at 397 nm is switched off.

Now the ion is excited on the qubit transition $S_{1/2}$, $m_j = -1/2 \leftrightarrow D_{5/2}$. Depending on the experiment either a freely propagating laser beam or the cavity field is used. The time window assigned to that process lies between 0.5 and 1 ms.

Finally, whether excitation happened or not is detected via the electron

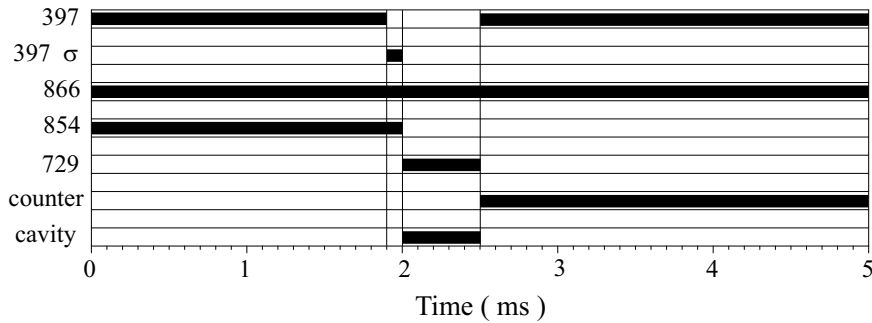


Figure 5.1: Example of a 5 ms pulse sequence. The numbers on the vertical axis denote the wavelengths in nm of the lasers. A black bar indicates the time the respective laser is switched on for. Counting the fluorescence is indicated ‘counter’, from 2.5 ms to 5 ms, as well as a possible scan of the cavity, denoted ‘cavity’, from 2 ms to 2.5 ms. In the first 2 ms a defined ‘starting’ state is prepared. This state is then manipulated (2 ms to 2.5 ms). After that the outcome is detected (excitation or not) for the remaining time. The manipulation can be just a pulse of a certain length and frequency with the 729 nm laser from either the side or through the locked cavity, or for example, it can be a 729 nm pulse on the cavity combined with ramping the non-locked cavity over resonance. The 10 ms and 20 ms pulse sequences differ only in a longer manipulation window (1 ms) and a longer detection (remaining time). The longer detection allows for the clear and uncritical setting of the threshold that is used to detect whether excitation occurred or not.

shelving technique: the blue light at 397 nm is switched on (866 nm light is on anyway) and the fluorescence is counted by the PMT for a time depending on the duration of the total pulse sequence. For a pulse sequence of total length 5 ms this is just ≈ 2.3 ms, for the 10 ms sequence it is ≈ 7 ms, and for the line triggered 20 ms sequence² it is up to 17 ms. The PMT count rate for the fluorescent ion is ≈ 16 kHz, the signal-to-background ratio around 10. By comparing the number of counts in the time interval with a threshold we can discriminate with very high probability ($> 99\%$) [61] whether excitation happened (electron shelved in $D_{5/2}$, no fluorescence) or whether the ion remained in the ground state (fluorescence). Note that although state detection happens a few ms after the ion-light interaction the ion's state is well preserved due to the long lifetime (≈ 1 s) of the $D_{5/2}$ level.

This procedure is typically repeated 100 times to yield the average excitation probability. After that, changes in the excitation window may be applied as for example: a change in the laser frequency (frequency scan) or a change in the excitation pulse length (pulse length scan). For example, to obtain an excitation spectrum, the 729 nm laser is tuned over the quadrupole transition in steps of 1 kHz.

5.2 Excitation with a Propagating Laser Beam

After having set up a new apparatus its performance and characteristics have to be explored. In this section we focus on the trap and its parameters. All light to the cavity is blocked and the cavity is tuned off-resonance from any relevant Ca^+ transition.

5.2.1 Spectral Components of the $S_{1/2} \leftrightarrow D_{5/2}$ Transition

In figure (5.2) the 729 nm laser is scanned over the $S_{1/2}$, $m_j = -1/2 \leftrightarrow D_{5/2}$ transition in steps of 20 kHz and a pulse duration of 100 μs . Every point represents 100 experiments. The separation of the Zeeman components allows the magnetic field to be placed at $B = 3.4$ Gauss. This value is chosen in order to separate all spectral lines of interest but not to broaden the cooling transition too much. The trap is driven with a radio frequency at $\omega_{RF} = 2\pi \cdot 27.3$ MHz. From the strength of the micromotional sideband of the strongest transition ($S_{1/2}$, $m_j = -1/2 \leftrightarrow D_{5/2}$, $m_j = -5/2$) at a detuning of 17.7 MHz (denoted 'mm' in figure (5.2)) we can deduce the quality of micromotion compensation at least in direction of the exciting beam.

²This sequence is triggered by the phase of the power line to get rid of periodic fluctuations which have frequencies that are multiples of the power line frequency (50 Hz).

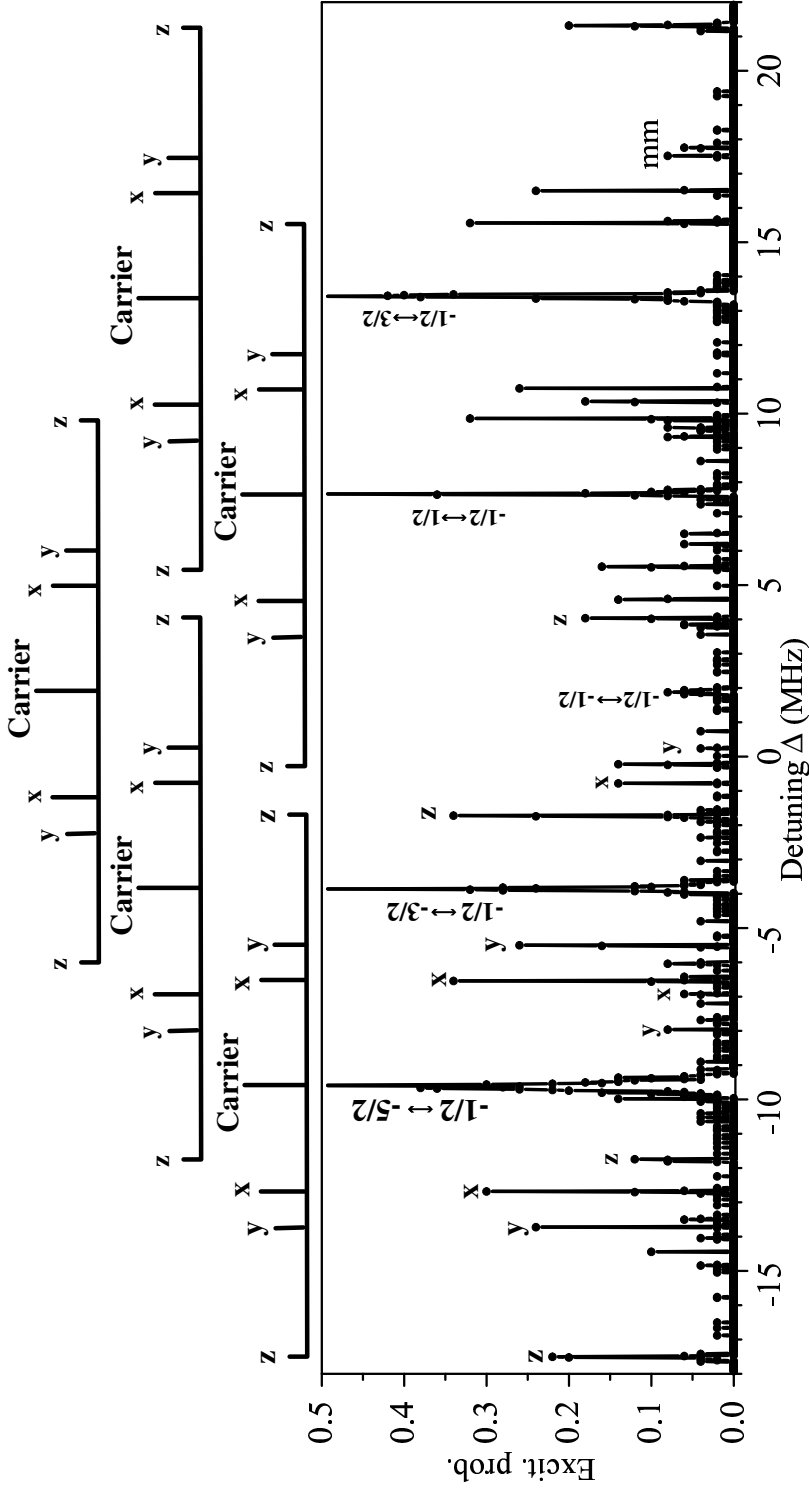


Figure 5.2: Spectrum of the $S_{1/2}, m_j = -1/2 \leftrightarrow D_{5/2}$ transition of a single $^{40}\text{Ca}^+$ ion. Magnetic field $B = 3.4$ Gauss. The carriers are indicated as well as the first-order sidebands of the $S_{1/2}, m_j = -1/2 \leftrightarrow D_{5/2}, m_j = -5/2$ and the $S_{1/2}, m_j = -1/2 \leftrightarrow D_{5/2}, m_j = -3/2$ transitions. The polarisation of the exciting beam is chosen in a way to maximise coupling to the $S_{1/2}, m_j = -1/2 \leftrightarrow D_{5/2}, m_j = -5/2$ transition. The micromotional sideband of the $S_{1/2}, m_j = -1/2 \leftrightarrow D_{5/2}, m_j = -5/2$ transition is indicated as ‘mm’.

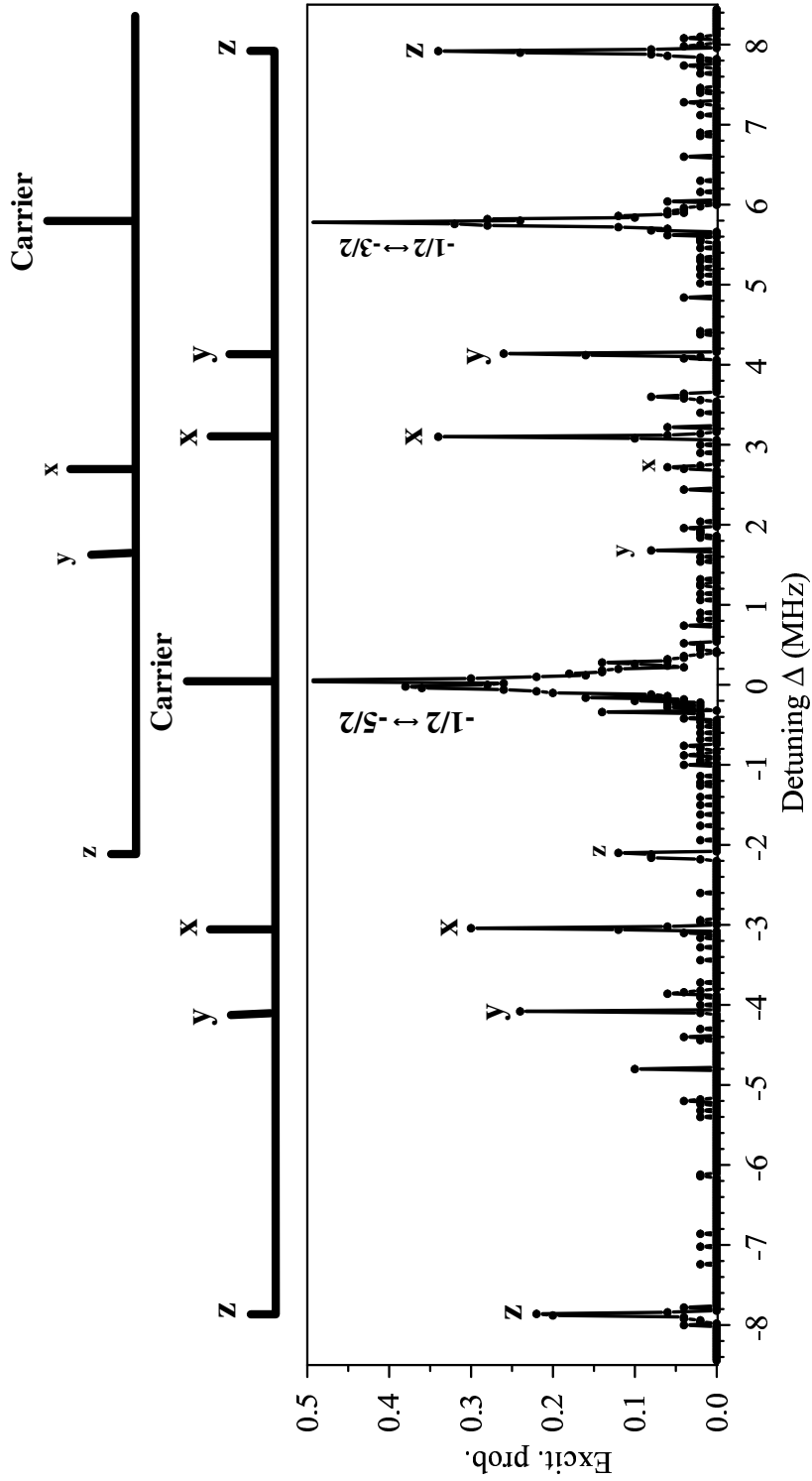


Figure 5.3: The $S_{1/2}$, $m_j = -1/2 \leftrightarrow D_{5/2}$, $m_j = -5/2$ transition and its first-order vibrational sidebands. The trap frequencies are found to be: $(\omega_x, \omega_y, \omega_z) = 2\pi \cdot (3.05, 4.1, 7.9)$ MHz.

In order to identify the spectral lines a slight change in the magnetic field can be made (carriers and the associated sidebands move according to the change in magnetic quantum number Δm of the transition) or the stiffness of the trap potential (carriers stay fixed but sidebands move). During the initial experimental runs this procedure has to be done quite often until some familiarity with the spectral lines is obtained. Figure (5.3) focuses on the transition $S_{1/2}, m_j = -1/2 \leftrightarrow D_{5/2}, m_j = -5/2$ which is of particular interest since it is used as a qubit (two-level system). The sidebands allow the trap frequencies to be read off immediately: $\omega_x = 2\pi \cdot 3.05$ MHz and $\omega_y = 2\pi \cdot 4.1$ MHz for the oscillators in the plane of the ring and $\omega_z = 2\pi \cdot 7.9$ MHz for the vibration perpendicular to this plane. The low amplitude of higher order sidebands is already an indication for good Doppler cooling.

5.2.2 Coherent Dynamics

A major ingredient for single ion experiments and the basis of any quantum operation on a qubit is the ability to perform coherent operations. Figure (5.4) shows as an example coherent Rabi-spectroscopy on the carrier of the $S_{1/2}, m_j = -1/2 \leftrightarrow D_{5/2}, m_j = -5/2$ transition. The 729 nm laser is scanned over resonance in steps of ≈ 3 kHz, exciting the ion with a short pulse of length τ . The line shape can be understood by considering Rabi oscillations with laser detuning³ Δ . For the generalised Rabi frequency Ω_Δ we have [68]:

$$\Omega_\Delta(\Delta) = \sqrt{\Omega_0^2 + (2\pi\Delta)^2}, \quad (5.1)$$

and the amplitude of the oscillations is given by:

$$\begin{aligned} p_{max}(\Delta) &= \frac{\Omega_0^2}{(2\pi\Delta)^2 + \Omega_0^2} = \frac{1}{1 + \left(\frac{2\pi\Delta}{\Omega_0}\right)^2}, \\ &= \left(\frac{\Omega_0}{\Omega_\Delta}\right)^2. \end{aligned} \quad (5.2)$$

Combining these, leads to the excitation probability $p(\Delta)$ at detuning Δ after the time τ :

$$\begin{aligned} p(\Delta) &= p_{max}(\Delta) \cdot \sin^2\left(\frac{\Omega_\Delta}{2} \cdot \tau\right), \\ &= \frac{1}{1 + \left(\frac{2\pi\Delta}{\Omega_0}\right)^2} \cdot \sin^2\left(\frac{1}{2}\sqrt{\Omega_0^2 + (2\pi\Delta)^2} \cdot \tau\right). \end{aligned} \quad (5.3)$$

³ Δ is here the laser detuning $\nu_l - \nu_a$ in the experiment, it therefore differs by a factor of 2π from the definition in chapter (2).

We see that the amplitude $p_{max}(\Delta)$ increases for smaller detuning Δ but may be dominated by the \sin^2 -function with the detuning dependent argument $\Omega_\Delta/2 \cdot \tau$. This leads to the observed line shape (cf. figure (5.4)). The example shows that the dynamics observed on the $S_{1/2} \leftrightarrow D_{5/2}$ transition is in very

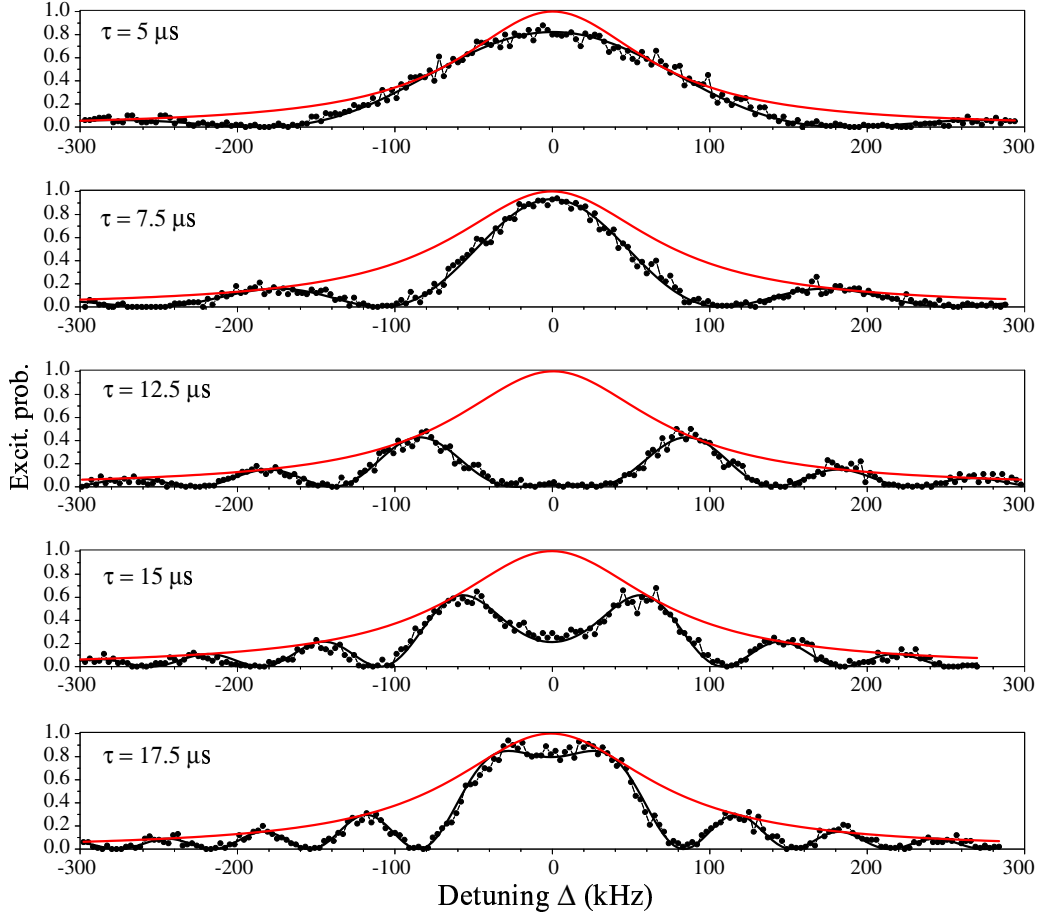


Figure 5.4: Example of coherent (Rabi-) spectroscopy on the $S_{1/2}, m_j = -1/2 \leftrightarrow D_{5/2}, m_j = -5/2$ carrier transition. The pulse length τ is increased from top ($\tau = 5 \mu\text{s}$) to bottom ($\tau = 17.5 \mu\text{s}$). Dots: experimental data, black solid line: fit of equation (5.3) to the data, taking the Rabi frequency Ω_0 as fit parameter. From top to bottom this parameter is: (455 ± 3) kHz, (482 ± 3) kHz, (482 ± 2) kHz, (483 ± 1) kHz and (485 ± 1) kHz. The variations in Ω_0 are probably due to intensity fluctuations of the exciting laser. The grey solid line shows the maximum amplitude of Rabi oscillations at a given detuning Δ (i.e. equation (5.2)) and illustrates the origin of the line shape.

good agreement with the prediction of the theoretical two-level model and it therefore confirms once more the suitability of these two levels as a qubit.

5.2.3 Determination of the Vibrational State

Figure (5.5) shows pulse length scans on the carrier and the first-order red motional sidebands after Doppler cooling. From these experiments the temperature (average phonon number \bar{n}) of the different oscillators can be calculated in the following manner: in the Lamb-Dicke regime ($\eta^2(2n+1) \ll 1$) the coupling to the carrier is approximated by [10]:

$$\Omega_{n,n} \approx \Omega(1 - \eta^2 n), \quad (5.4)$$

where Ω is the overall coupling strength. On the first-order red sideband the coupling strength is (see chapter 2):

$$\Omega_{n_i-1,n_i} \approx \Omega \eta_i \sqrt{n_i}. \quad (5.5)$$

Neglecting the term of $\mathcal{O}(\eta^2)$ and dividing expression (5.5) by (5.4) the following expression is obtained:

$$\frac{\Omega_{n_i-1,n_i}}{\Omega_{n,n}} \approx \eta_i \sqrt{n_i} + \mathcal{O}(\eta_i^2). \quad (5.6)$$

The Lamb-Dicke parameter η_i is defined by:

$$\eta_i := k \cdot \cos \phi_i \sqrt{\frac{\hbar}{2m\omega_i}}, \quad (5.7)$$

where ϕ_i is the angle between oscillator axis and laser beam. Knowing the angle ϕ_i , n_i can be calculated for a pure state from the Rabi frequencies on the carrier and on the first-order sideband. However, after Doppler cooling the trapped ion is not in a pure vibrational state. It is reasonable to assume a thermal distribution over harmonic oscillator states $|n_i\rangle$ where the probability of finding the system in state $|n_i\rangle$, for a mean phonon number

\bar{n}_i , is given by [68]:

$$p_{n_i} = \frac{1}{\bar{n}_i + 1} \left(\frac{\bar{n}_i}{\bar{n}_i + 1} \right)^{n_i}. \quad (5.8)$$

Different states $|n_i\rangle$ contribute with different Rabi frequencies on the $|S, n_i\rangle \leftrightarrow |D, n_i\rangle$ transition depending on $n_i\eta_i^2$. The thermal mixture of different oscillation frequencies washes out the Rabi oscillations which therefore appear damped. Nevertheless the expectation value \bar{n}_i for the ensemble can be determined approximately by comparing data and numerical simulations. The top diagram in figure (5.5) shows Rabi oscillations on the carrier. The theoretical curve is calculated with $\Omega = 2\pi \cdot 630$ kHz,

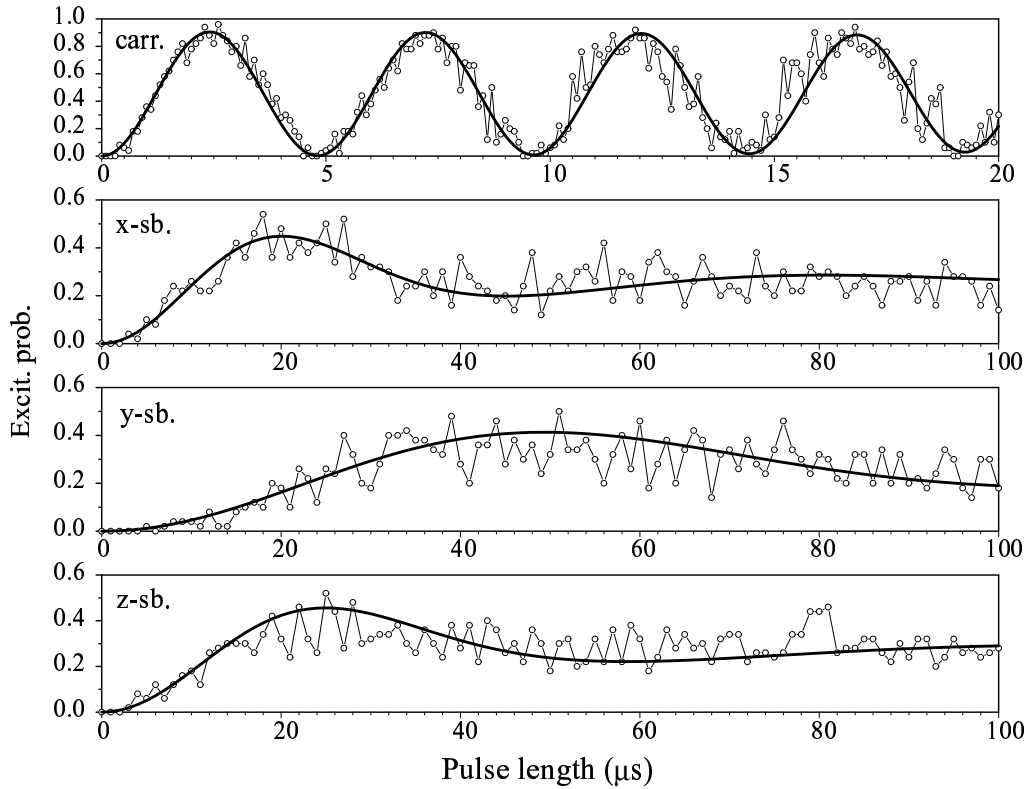


Figure 5.5: Rabi flops on carrier and red motional sidebands of the $S_{1/2}, m_j = -1/2 \leftrightarrow D_{5/2}, m_j = -5/2$ transition after Doppler cooling. Note the different time scales on the axis for carrier (top) and sidebands. Dots: experimental data; solid line: theoretical simulation, for details see text.

$\bar{n} = 4$, $\eta = 0.06$ and a laser detuning $\Delta = 200$ kHz from resonance. The x-, y- and z-sidebands oscillate much more slowly due to the factor of η_i in (5.5). Numerical simulations are calculated assuming $\Omega = 2\pi \cdot 630$ kHz, $(\bar{n}_x, \bar{n}_y, \bar{n}_z) = (20, 4, 6)$, $(\eta_x, \eta_y, \eta_z) = (0.020, 0.0175, 0.030)$ and a laser detuning $(\Delta_x, \Delta_y, \Delta_z) = (38, 16, 29)$ kHz from resonance. By varying these values and comparing simulation and data, an error can be estimated for these quantum numbers: $(\bar{n}_x, \bar{n}_y, \bar{n}_z) = (20 \pm 5, 4 \pm 1, 6 \pm 1)$. From these average values we see that the ion is sufficiently Doppler cooled. We can calculate the extensions w_i of the ion's motional wave packet along the directions of the vibration axes:

$$w_i = \frac{\eta_i}{k \cdot \cos \phi_i} \sqrt{2\bar{n}_i + 1} = \sqrt{\frac{\hbar(\bar{n}_i + \frac{1}{2})}{m\omega_i}}. \quad (5.9)$$

For our geometry we find:

$$(w_x, w_y, w_z) = (41.5 \pm 5, 17.0 \pm 2, 14.5 \pm 1) \text{ nm}. \quad (5.10)$$

Of particular interest is the rms extension of the motional wave packet along the cavity axis. We calculate:

$$w_{cav} := \sqrt{\left(\sum_i (\text{projection of } w_i \text{ on the cavity axes})^2 \right)}, \quad (5.11)$$

$$\approx (25 \pm 5) \text{ nm}.$$

This confinement is much smaller than the wavelength of the 729 nm laser. Therefore the ion can be used as a nanoscopic probe to measure the standing wave pattern between the cavity mirrors and cavity QED effects dependent on the position of the ion in the standing wave can be explored.

Chapter 6

Experiments on Ion–Cavity Coupling

To gain some experience of the cavity light field a series of experiments was started exploring the dynamics of cavity–ion coupling. We did this by scanning the cavity over resonance. The cavity fills with light and decays afterwards, the excitation probability at different laser detunings depends in general on the scanrate (i.e. on the motion of one of the mirrors) and on the position of the ion in the standing wave. After having studied the dynamics of the coupling, work was done to prove coherent interaction of cavity field and ion by exciting through the frequency stabilised cavity. Finally, first steps towards the observation of the influence of the locked cavity on the lifetime of the $D_{5/2}$ state were taken.

6.1 Cavity–Scanning Technique

The basic scheme is as described in chapter (5), except that now the excitation of the trapped ion occurs via the cavity field. The general pulse scheme is shown in figure (5.1). After Doppler cooling, light at 729 nm is injected into the TEM_{00} mode of the off resonant cavity. Simultaneously the voltage of one of the cavity piezos is ramped up thereby displacing the associated mirror and hence the cavity is scanned over resonance. When the cavity becomes resonant with the 729 nm light, it fills with light and may excite the ion to the metastable $D_{5/2}$ level. When ramping the cavity mirror down to its initial position, the light at 729 nm is switched off. At the same time the ion’s state is detected as usual. This procedure is repeated 100 times to determine the excitation probability. After that the excitation laser is detuned and the procedure as described above is repeated. Usually we record the

excitation probability as a function of the laser frequency detuning Δ from the atomic transition. Three sorts of experiments were performed. In the first, we vary the scan rate and therefore the velocity of the scanned mirror, keeping the ion's position in the standing wave fixed. In the second, we keep the mirror scanrate fixed but move the standing wave pattern relative to the ion's position with help of the offset voltages of both piezos. The third kind of experiment is basically like the second but the ion is excited on the carrier and also on the first-order sideband transition alternately to demonstrate the orthogonal coupling in the standing wave.

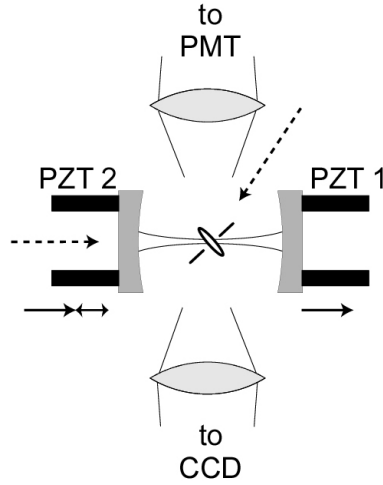


Figure 6.1: Schematic drawing of the cavity scanning technique: PZT1 denotes the offset piezo, PZT2 the scan piezo. Instead of coupling the ion to a travelling wave as usual (laser beam denoted with the dashed line on the top right from above), it is coupled to the standing wave built up in the cavity when scanned over resonance by PZT2. The position of the ion relative to nodes and antinodes can be controlled by adjusting the offsets of both piezos.

6.1.1 Temporal Variations of the Intracavity Field

The first experiment looks at probing the ion's response to temporal variations of the intracavity field by placing it close to a node of the standing wave field¹ and varying the cavity scan rate. Figure (6.2) shows the excitation probability to the $D_{5/2}$ level on the carrier transition ($S_{1/2}, m_j = -1/2 \leftrightarrow D_{5/2}, m_j = -5/2$) for different scan rates. Increasing the scan ve-

¹Remember: the coupling to a quadrupole transition is maximum at a field node.

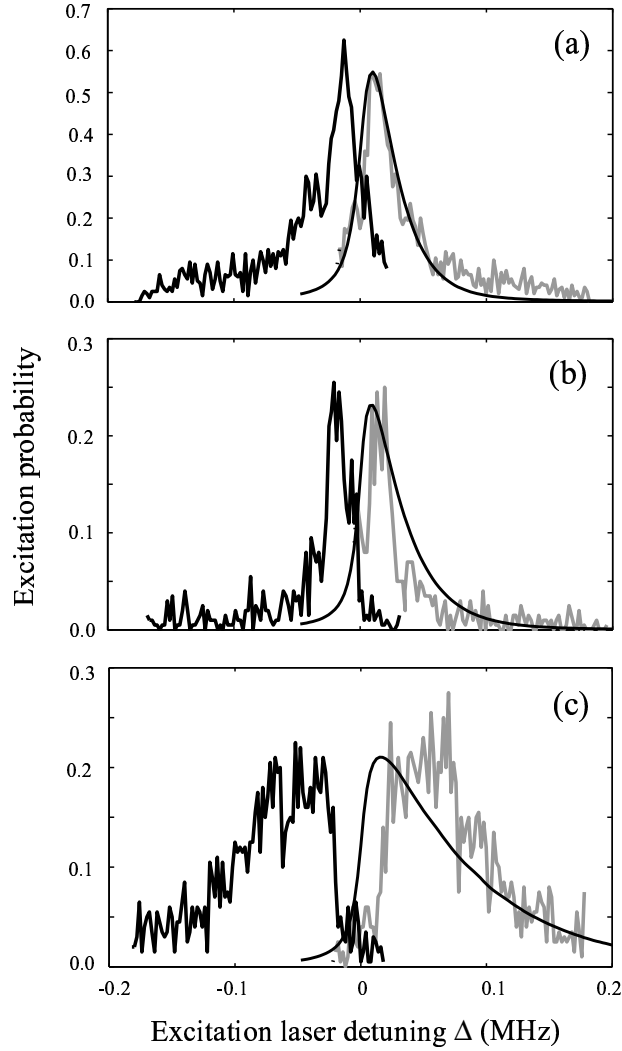


Figure 6.2: Excitation spectra for different cavity scan rates $\nu_L = \pm 0.16$ (a), ± 0.23 (b) and ± 0.69 (c). On the blue shifted spectra the theoretical simulations are superimposed (solid line). The parameters for the simulations are: laser bandwidth $\Delta\nu_{laser} = 6$ kHz, natural linewidth of the $S_{1/2} \leftrightarrow D_{5/2}$ transition $\Delta\nu_{SD} = 0.17$ Hz, Rabi frequency for zero detuning: $\Omega_0 = 15.5$ kHz (a), 11 kHz (b) and 25 kHz (c).

locity increases the shift from the line center (zero detuning) that is found by excitation with a freely propagating laser beam. For negative scan rates the mirrors move towards each other and thereby shift the light via the Doppler effect to the blue. The atomic transition appears to be red shifted in that

case. For positive scan rates the opposite situation is true: the mirrors move apart, the light in the cavity is red shifted and most excitation occurs for blue detuned light (to compensate for the red Doppler shift). In addition, faster scan velocities broaden the line because more and more frequency components are added to the light confined in the cavity. To put these observations in a more quantitative form it is convenient to define a normalised scan rate ν_L by (cf. appendix (B)):

$$\nu_L := \frac{2\mathcal{F}\omega\dot{L}\tau}{\pi \cdot c} . \quad (6.1)$$

ν_L corresponds to the resonance frequency shift of the cavity in units of the HWHM cavity linewidth ($= c/(4L\mathcal{F})$) per cavity energy storage time $\tau := \mathcal{F}L/(\pi c)$. To model the dynamics the electric field acting on the ion must first be known. This field then interacts with the ion described by the Bloch equations for a two-level system. The electric field amplitude E_{cav} in a cavity swept over resonance has been studied in [66, 67] and is a solution

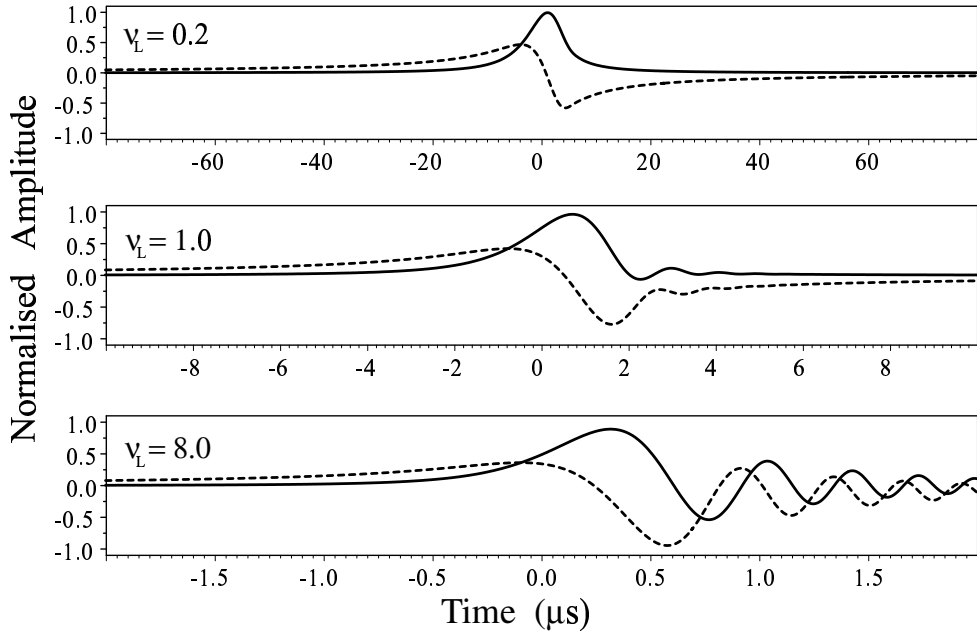


Figure 6.3: Calculated time dependent normalised electric field amplitude in the cavity for three different scan rates ν_L . The solid line is the real part, the dashed line the imaginary part of the electric field amplitude. For larger scan rates the interference of incoming and stored light becomes visible in the real as well as in the imaginary part of the complex amplitude.

of the differential equation:

$$\frac{dE_{cav}}{dt} = -(1 - i\nu_L \bar{t})E_{cav} + i\frac{\sqrt{\mathcal{T}}\mathcal{F}}{\pi}E_0, \quad (6.2)$$

where $\bar{t} := t/\tau$, $\mathcal{T} \approx \pi/\mathcal{F}$ is the transmission of the input coupling mirror and E_0 is the amplitude of the input field. Slow scan rates ($\nu_L \ll 1$) lead to the quasi static case whereas fast scan rates ($\nu_L \gg 1$) cause the incoming light to interfere with the light stored in the cavity. Figure (6.3) shows the normalised intra cavity field for three different scan rates. The interaction of this time dependent electric field with the ion can now be modelled by numerically integrating the Bloch equations for a two-level system. The result for a scanrate of $\nu_L = 1$ and a typical laser intensity is shown in figure (6.4). The electronic transition (figure (6.4 top)) is blue shifted and broadened compared to the excitation with a freely propagating laser beam as

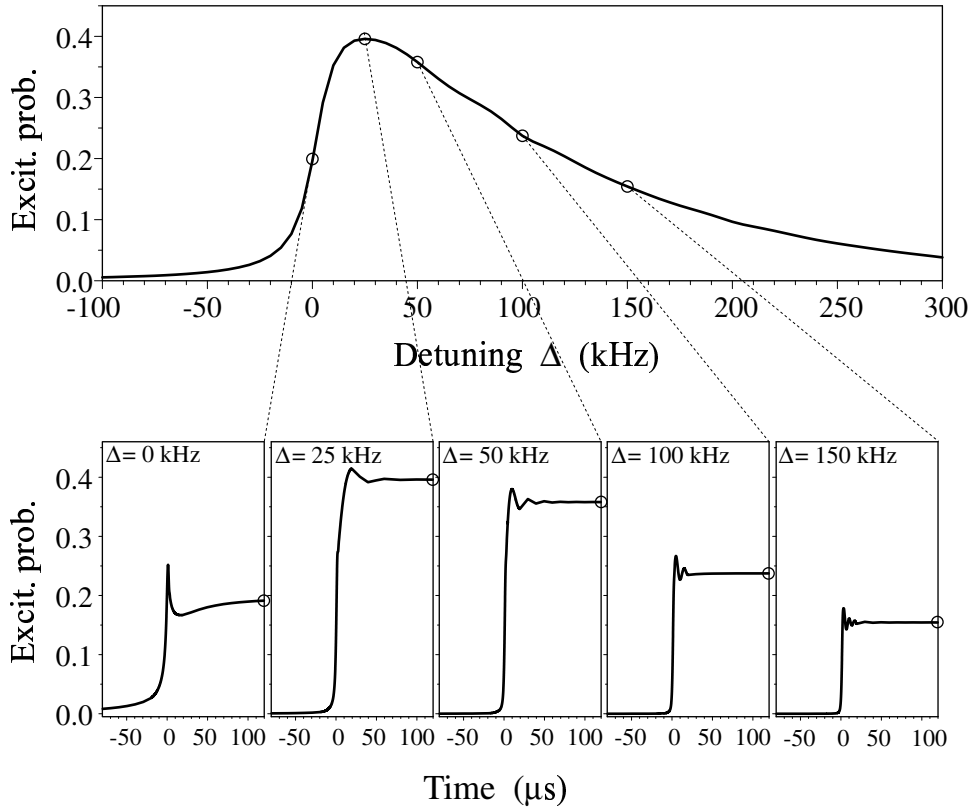


Figure 6.4: Simulated excitation line for $\nu_L = +1$ (top) and time evolution of the excitation for different detunings Δ (leading to the excitation line). For details see text.

expected. Shift and broadening increase with increasing scanrate, scanning in the opposite direction leads to an excitation spectrum that is mirrored about the zero detuning position.

Figure (6.4 bottom) illustrates the time evolution of the excitation to the $D_{5/2}$ level for five different detunings Δ as the cavity is swept over resonance. For all detunings, the excitation probability shows a steep rising edge at the moment the cavity fills with light and subsequent Rabi oscillations with a damping depending on excitation power and detuning. This excitation characteristic remains qualitatively unchanged over a large range of excitation powers and scan rates. The final stationary values of the excitation probabilities are used to determine the excitation spectrum shown in the upper diagram of figure (6.4). The results of such a theoretical simulation for positive scan rates are shown as solid lines superimposed on the blue shifted spectra in figure (6.2).

The calculated and experimental spectra show good agreement for small scan rates (figure (6.2 a,b)). For larger scan rates (figure (6.2 c)) the centers of the spectra become slightly shifted. We assume that this shift is caused by nonlinearities and hysteresis effects of the piezo motion. Although we kept the excitation power constant in the experiments, we left the Rabi frequency Ω_0 as fit parameter to account for variations in excitation due to a thermal drift of the cavity, which could shift the node of the standing wave away from the ion’s position.

The experimental investigation and theoretical understanding of the ion–cavity field coupling dynamics as previously discussed are important for the realisation of an atom–photon interface in quantum networks. The experimental implementation of such a scheme requires control over the shape of the light pulse emitted from the cavity and thus control over the dynamic atom–cavity coupling [7].

6.1.2 Spatial Variations of the Intracavity Field

The travelling wave field of a propagating laser beam or the standing wave field within a cavity gives rise to different excitation characteristics of the ion. In the case of a freely propagating laser beam a change in position along the beam corresponds to a phase shift of the light field. In the standing wave the amplitude of the field also changes as one moves from a node to an antinode or vice versa. The trapped single ion is confined to a region in space of less than 30 nm which is much less than the excitation wavelength (729 nm). It therefore can be used as a nanoscopic probe of the field variations, first shown in [56]. The ion’s position in the standing wave can be controlled to a high degree and therefore the standing wave pattern can be explored.

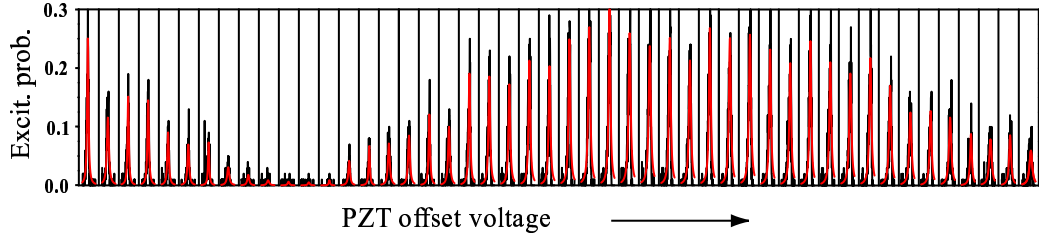


Figure 6.5: All 48 excitation spectra measured at different positions in the intracavity standing wave. Each box contains a spectral line that is 600 kHz wide, the offset voltage increases from left to right. The standing wave pattern is already visible, the total shift is roughly 1.5 half waves.

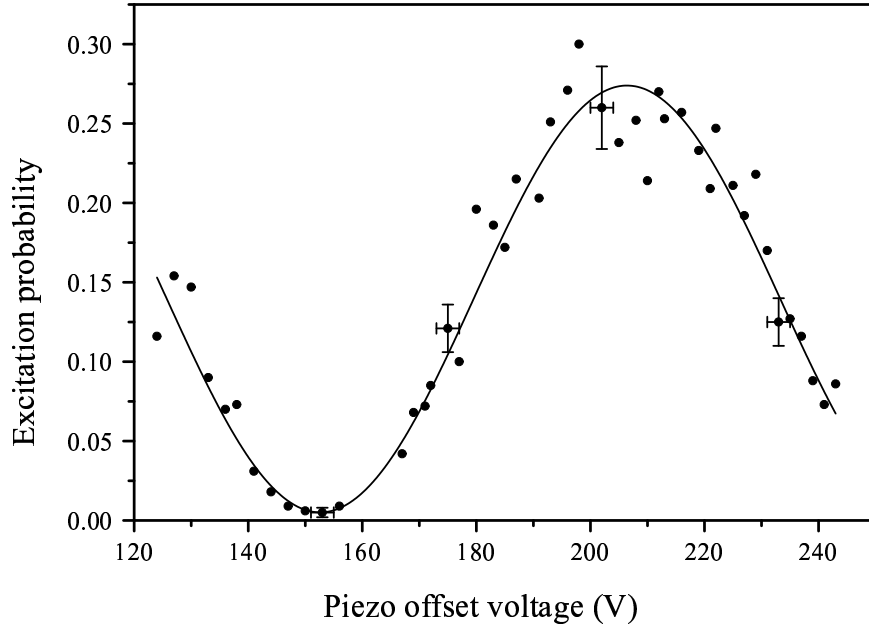


Figure 6.6: Excitation probability on the $S_{1/2} - D_{5/2}$ transition of a single trapped Ca^+ ion as function of the piezo offset voltage (corrections for piezo drift and piezo hysteresis have been applied, see text), i.e. as a function of the ion's positions in the intracavity standing wave field. The solid line represents a \sin^2 -function fitted to the data points.

To probe this spatial variation, we leave the scan rate fixed at a small value, allowing for stable scans with little perturbation of the excitation spectrum as shown in figure (6.2 a). The laser is scanned over the carrier tran-

sition in steps of ≈ 1 kHz. An excitation spectrum at some position in the standing wave is obtained. Now the offset voltages for the scan piezo and for the offset piezo (see figure (6.1)) are varied simultaneously and therefore the standing wave pattern is shifted longitudinally relative to the ion's position. The procedure is repeated and a number of excitation spectra are obtained: the results are shown in figure (6.5). To use the excitation probability as a measure for the field intensity, it is important to adjust the laser power such that the excitation is kept well below saturation at all positions in the standing wave. The position-dependent excitation probability is determined by fitting each excitation spectrum with a Lorentzian and determining the peak value. Figure (6.6) displays these values as function of the (drift corrected) piezo offset voltage. Error bars given for representative data points in figure (6.6) are due to piezo hysteresis (abscissa) and the errors of the fits to the excitation spectra (ordinate).

The way the piezo offset voltage is corrected for hysteresis effects is detailed in the following. To shift the standing wave pattern relative to the ion both piezo offset voltages have to be changed and their voltages should be proportional (assuming no hysteresis). Figure (6.7) shows that this is not always the case. Two kinds of correction have been applied to the measured voltage. On average, the proportionality factor between a change in the offset voltage of PZT2 and the offset voltage of PZT1 can be determined. A sudden step change in this proportionality factor from the average value is due to some hysteresis effect. The offset voltage of PZT2 is changed in just one direction and so it is assumed that the hysteresis effect plays no role for PZT2 (as it is expected, except for the special cases discussed below). For PZT1 however, which is shifted back and forth by hand, hysteresis does play a role. Another effect which can lead to changes in the proportionality factor is that of time delays. As noticed in the laboratory note book, a laser fell out of lock during data acquisition at -2.6 V and -2.4 V delaying the measurement. Due to the drift of the trap cavity a pause in data acquisition results in a change of position in the standing wave. To compensate for these effects, the voltage on PZT1 has been corrected by up to 3 V. The step between -1.0 V and -0.8 V in figure (6.7) can be determined as a hysteresis effect of PZT2: when adjusting the offset voltage from -1.0 V to -0.8 V, the function generator switches off completely for about half a second and then switches on again at the new value. This shifts the mirror by a large amount back and forth and explains a change in position that differs from the usual step due to the hysteresis. That this effect cannot be seen in the data when switching from 0.8 V to 1.0 V might be due to the different restoring force (spring tension) at that voltage. A change in spring tension may also be the reason for the deviation of the proportionality factor at high voltages from

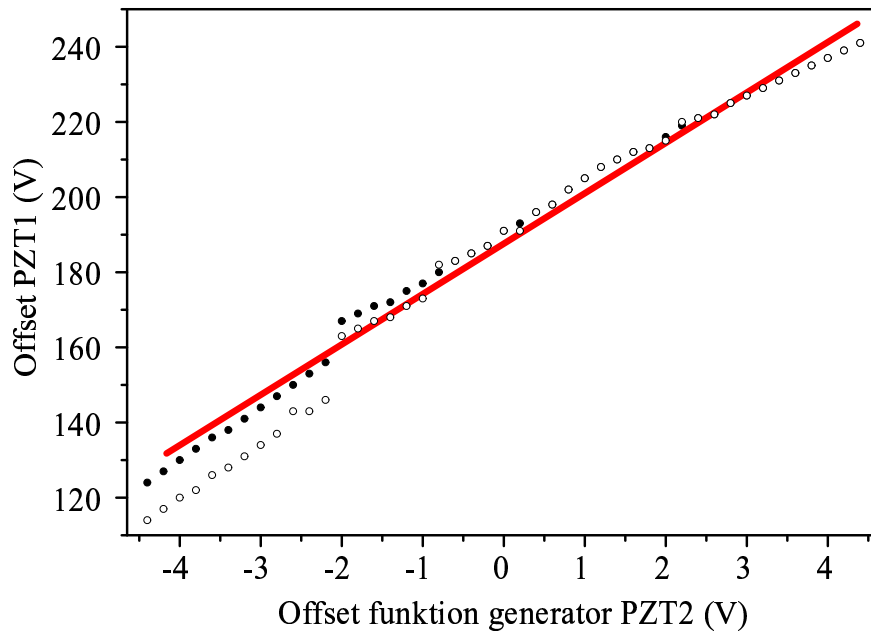


Figure 6.7: The offset voltage of PZT1 (offset piezo) as function of the function generator offset voltage of PZT2 (scan piezo) for resonant cavity length. The circles are original data; the points are the corrected data, taking known hysteresis effects into account.

the proportionality factor at low and middle voltages (note that the curve in figure (6.7), ‘bends down’ at high voltages). The step between -2.2 V and -2.0 V can be explained to some extent by a longer delay for some reason (indicated by the generation time of the data files). To correct for these shifts, the first 10 voltages up to -2.2 V have been shifted by $+10$ V, the voltages from -2.0 V up to -1.0 V have been shifted by $+4$ V. The resulting values are shown in figure (6.7) as points. As is obvious from the original data, the errors are not statistical but have mostly a systematic origin. The piezos shrink and expand in a linear fashion for parts of the total shift but this linear behavior is disrupted by steps where one of the piezos jumps or gets stuck due to mechanical friction in the guide of the mirrors (perhaps followed by a jump). Unfortunately it is not known when or which piezo behaves irregularly except for special cases where the above correction has been applied by assuming a linear behavior of the other piezo. Furthermore, it is rather difficult to account for the errors due to the individual thermal drifts of both mirror mounts, the drift of the cavity mount and the drift of the cavity relative to the trap. Taking all these arguments into account an

error for the corrected voltage values of ± 2 V can be justified.

The excitation probability varies spatially with the intensity of the standing wave. A theoretical Bloch–equation analysis as described previously predicts a nearly pure \cos^2 spatial variation as shown in the top diagram of figure (6.8). The solid line is the expected experimental excitation probability assuming a two–level system excited by a single standing wave field mode ($\mathbf{E} \propto \sin(\mathbf{k} \cdot \mathbf{x})$). It has been calculated by a two–level Bloch–equation analysis assuming $\nu_L = 0.6$. The extension of the wave packet was simulated by applying a gliding average² over the position. The number of points used for this average was chosen such that the minimum excitation agrees with the experimental data. The maximum Rabi frequency Ω_0 on the transition is determined from a fit to the experimental value of the maximum excitation at the node of the standing wave. By normalising the excitation probability amplitude, the simulation is very robust against variations in all parameters. The error of the experimental data is indicated for representative points (cf. figure (6.6)). To find the deviation of the more complex model from the simple \cos^2 –model the simulated data is fitted with a \cos^2 –function, taking the individual errors of the data points into account. The resulting \cos^2 –function is indicated in figure (6.8 top) as a dashed line. The absolute difference of the models (dashed line) as well as the statistical error of the actual experiment (solid line) is shown in figure (6.8 bottom). We see that for our experiment the statistical error is at any point at least almost three times larger than the deviation of the two models. Therefore the fitting of the experimental data to the simple \cos^2 –model is justified.

From the \cos^2 –fit to the data points the contrast ratio (visibility V) of the position-dependent excitation is found to be $V = (96.3 \pm 2.6)\%$. This very high visibility results from the strong localisation of the ion’s spatial wavefunction. The laser-cooled ion, oscillating with its secular frequencies and with thermally distributed amplitudes, has an rms spatial extension along the cavity axis of w_c . This extension leads to a reduction of the excitation contrast by a factor of $\exp(-2(2\pi w_c/\lambda)^2)$ compared to the excitation contrast experienced by a point-like atom at rest [69]. A value of $w_c = 16_{-7}^{+5}$ nm is determined from the measured visibility V . The small value of the extension w_c shows that in this experiment the ion is cooled close to the Doppler limit (13 nm).

A necessary condition for all experiments relying on ion–cavity mode coupling is the ability to place the ion at a certain position of the intracavity

²More precisely, the excitation probability for the point-like particle would have to be convoluted with the spatial probability distribution of the trapped ion. The gliding average uses a rectangular distribution, which is sufficient for this analysis, as an approximation to the more complicated thermal wave packet.

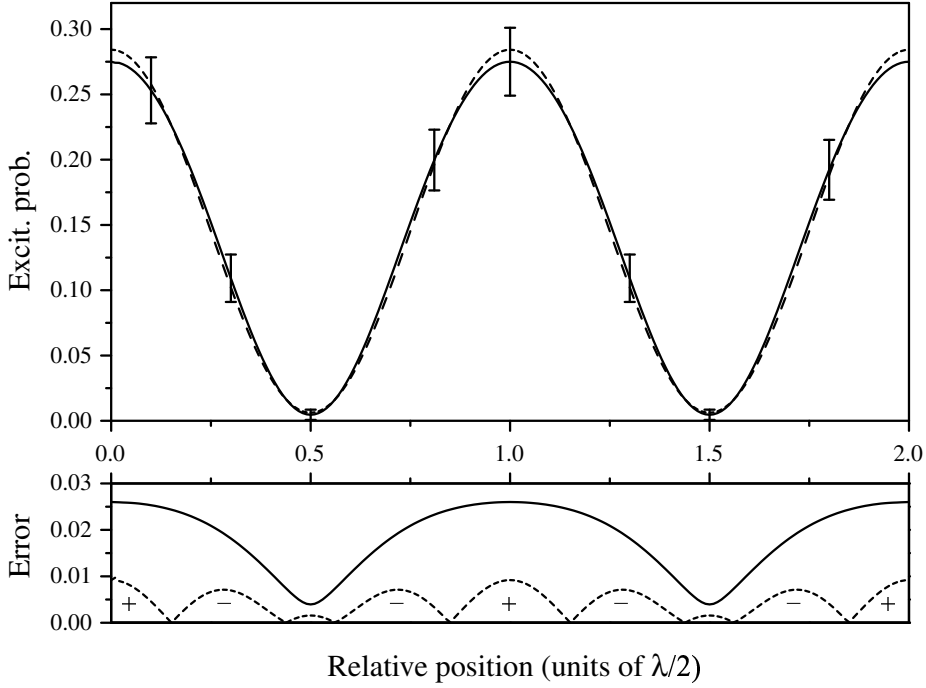


Figure 6.8: Top: the solid line is the prediction of a Bloch–equation analysis assuming a two–level system in a standing wave field. The maximum excitation was chosen to coincide with the level measured in the experiment. Error bars are indicated for the actual experimental data. The dashed line is a \cos^2 –fit to the model taking errors into account. Bottom: the dashed line shows the absolute difference of prediction by Bloch–equation simulation and simple \cos^2 –model. This error must be compared to the experimental statistical error for the actual experiment (solid line). Note the different scales on the ordinate. For details see text.

standing wave field with high precision and high reproducibility [56]. In our experiment, the precision of positioning the center of the ion’s wavefunction, using a measurement such as that in figure (6.6), is limited by the uncertainty in the measured excitation probability. This uncertainty is due to a statistical error, i.e. the finite number of state detection measurements, and systematic errors such as fluctuations of laser intensity and wavelength, drift and jitter of scan piezo etc. [70]. From the uncertainties in excitation probability (see error bars in figure (6.6)) the deduced spatial precision is 7 nm ($\approx \lambda/100$) at the position of largest slope, 12 nm at the point of minimum excitation and 36 nm at the point of maximum excitation. However, the precision can be enhanced by averaging over a larger number of state detection measurements.

6.1.3 Coupling of Motional States

Many schemes for quantum information processing with trapped ions rely on coherent interaction not only with the internal electronic state but also with the external motional degrees of freedom. The controlled coupling of atomic states dressed by vibrational modes to the cavity field is a prerequisite for realising such schemes.

Comparing the carrier ($\Delta n = 0$, no change of vibrational quantum number) and first–order vibrational sideband ($\Delta n = -1$) transition probabilities in a standing wave, both show a position dependent coupling due to the standing wave pattern as shown in section (6.1.2). However, where the coupling to the carrier is strongest, no coupling to the first–order (i.e. all odd) sidebands occurs and vice versa, i.e. carrier and odd sidebands excitations map the standing wave spatial field variation, but the traces are shifted by a phase factor of π . This phase shift arises due to symmetry characteristics of the transition matrix elements of carrier and sideband transitions in a standing wave field as discussed in chapter (2) and [13, 71]: the spatial part of the quadrupole transition matrix element is proportional to $\langle n' | \exp(ikx) | n \rangle$ for a travelling wave and $\langle n' | \cos(kx) | n \rangle$ for a standing wave with the electric field³ $E \propto \sin(kx)$. Here n and n' are the vibrational quantum numbers in the $S_{1/2}$ and $D_{5/2}$ level respectively, k is the wavenumber and x is the ion’s position in the field. For a travelling wave, all vibrational states (n, n') can be coupled as $\exp(ikx)$ contains even and odd powers⁴ of kx . In contrast, for a standing wave $\langle n' | \cos(kx) | n \rangle$ has to be expanded into even *or* odd powers of kx depending on the ion’s position, e.g. $x = 0$ close to a node or $x = \lambda/4$ close to an antinode. Thus, transitions changing the phonon number by even or odd integers can only be maximally excited at different positions in the standing wave. The first–order sideband transition ($\Delta n = \pm 1$) couples maximally at antinodes of the standing wave, whereas the carrier transition ($\Delta n = 0$) couples maximally at nodes.

In order to demonstrate this motional–mode dependent coupling, we recorded excitation probabilities of the ion at a fixed cavity scan rate ($\nu_L = -0.23$), for different positions within the standing wave, and with the laser at 729 nm now tuned to either the carrier or the red axial sideband ($\Delta n = -1$, laser detuned by $-\omega_z$) of the $S_{1/2}, m_j = -1/2 \leftrightarrow D_{5/2}, m_j = -5/2$ transition. In both cases, the intensity of the laser was adjusted such that the excitations of carrier and sideband were comparable and were kept well below saturation. In this experiment we determine the integral excitation, i.e. the area

³for a quadrupole transition

⁴Note: $kx = \eta(a_v + a_v^\dagger)$ at a node and $kx = \eta(a_v + a_v^\dagger) + \pi/4$ at an antinode of the field.

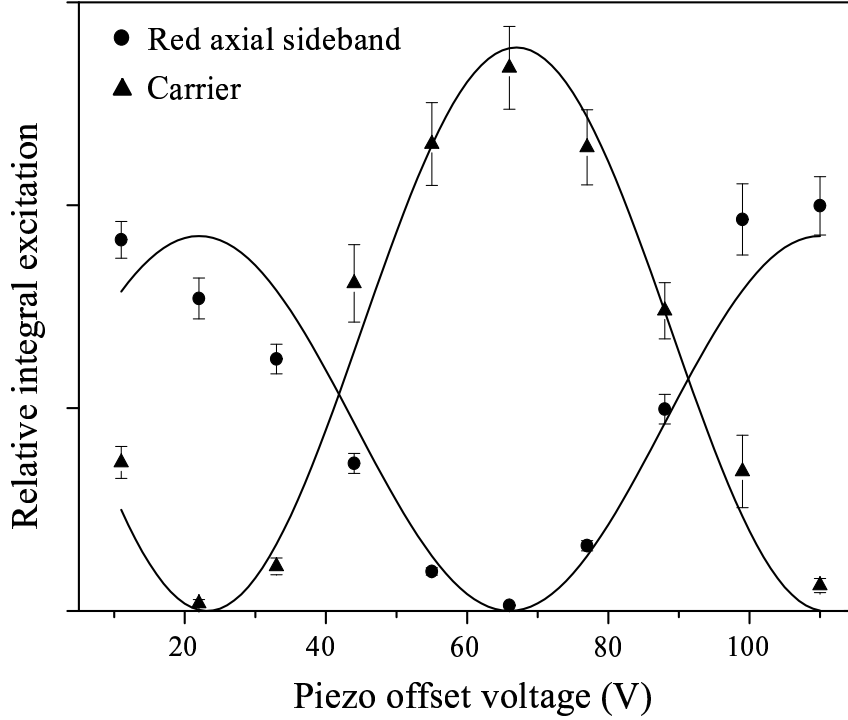


Figure 6.9: Integral excitation on the carrier (triangles) and the red axial sideband (circles) of the $S_{1/2}, m_j = -1/2 \leftrightarrow D_{5/2}, m_j = -5/2$ transition as a function of the piezo offset voltage, i.e. at various positions in the intracavity standing wave field. The solid lines represent fits of \sin^2 functions to the data points.

of the particular excitation spectrum, since the spectra show an asymmetric line shape (cf. figure (6.2 b,c)).

The high-contrast orthogonal coupling of carrier and sideband transitions to the cavity mode is shown in figure (6.9). It facilitates applications such as cavity-assisted cooling in a standing wave [71], the Cirac-Zoller quantum-computing scheme [72] and entanglement of motional and photonic states when coupling to the cavity vacuum field [73, 74]. In particular, cavity-assisted cooling in a standing wave field means that sideband-cooling [61] on a red detuned vibrational sideband is facilitated by suppression of off-resonant carrier transitions which induce motional heating. In a similar fashion, unwanted off-resonant carrier excitations are suppressed when driving sideband transitions in the Cirac-Zoller quantum-computing scheme. In this case off-resonant carrier excitations impose a limit on the attainable gate speed [75]. As electronic excitation probabilities of the ion depend on

both the vibrational state and the position within the cavity field, the internal electronic degrees of freedom are coupled to both the single mode cavity field and the vibrational degrees of freedom (both of which are quantised in general). This coupling allows, for example, the generation of an entangled state of a subsystem that can store quantum information (vibration, electronic states) with a subsystem that can be used for propagation of quantum information (light).

6.2 Frequency Stabilised Cavity

The application of the ion–cavity coupling for implementation of quantum network schemes requires a controlled coherent interaction. To demonstrate such coherent coupling to the cavity field, we stabilise the trap cavity to the $S_{1/2}$, $m_j = -1/2 \leftrightarrow D_{5/2}$, $m_j = -5/2$ carrier transition frequency as described in section (4.4).

6.2.1 Coherent Ion–Cavity Coupling

We excite the ion placed close to a node with resonant laser pulses of different duration injected into the trap cavity. Changing the pulse length from zero to a duration of $3 \mu\text{s}$ the average excitation probability is determined from 100 experiments per pulse length. The resulting coherent dynamics (Rabi oscillations) are shown in figure (6.10) together with a numerical simulation

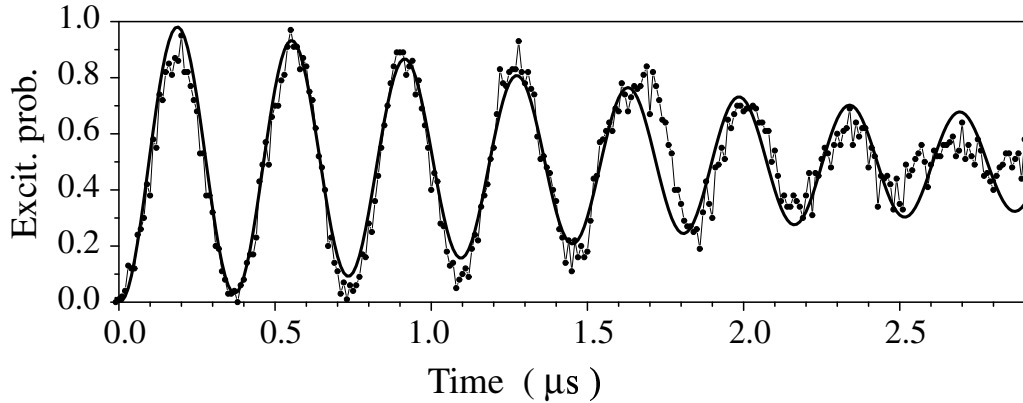


Figure 6.10: Rabi oscillations driven by the light field in the stabilised cavity. The parameters for the theoretical simulation are: Rabi frequency $\Omega_0 = 8.95 \text{ MHz}$, $\eta^2 \cdot \bar{n} = 0.049$ and laser detuning $\Delta = 0$.

(solid line). The theoretical curve is calculated assuming a thermal distribution of harmonic oscillator states $|n\rangle$ (secular ion motion) coupled to the atomic two-level system ($|S_{1/2}\rangle, |D_{5/2}\rangle$). As the Rabi frequency Ω_n of any particular transition $|S_{1/2}, n\rangle \leftrightarrow |D_{5/2}, n\rangle$ depends on the respective phonon number n times the Lamb-Dicke parameter squared η^2 , the superposition of different oscillation frequencies in a mixture of states wash out and the resulting Rabi oscillations are damped [10].

6.2.2 Towards Cavity Enhanced Spontaneous Emission

The ability to stabilise the cavity resonance on the atomic resonance frequency allows the exploration of enhanced⁵ spontaneous emission of the ion due to the Purcell effect [19]. With the present setup (cooperativity $C \approx 0.5$, Purcell factor $F \approx 2$, cf. chapter (4)) it is expected that a lifetime shortening of 50% is possible under perfect conditions (stable locks, ion in the center of the waist at a node). The experimental procedure for the lifetime measurement is now given:

The ion is Doppler cooled and prepared in the $S_{1/2}, m_j = -1/2$ state. A π -pulse on the $S_{1/2}, m_j = -1/2 \leftrightarrow D_{5/2}, m_j = -5/2$ transition excites the ion. For this we use a laser beam from the side (all 729 nm light to the cavity is blocked). The fluorescence on the $S_{1/2} \leftrightarrow P_{1/2}$ transition is measured to ensure that the ion is excited. Now we wait for up to 400 ms until the state is again determined (still excited or decayed).

This procedure is repeated and the number of total excitations and decays is recorded. This enables the lifetime to be determined. To extract cavity effects from other systematic errors we run 100 experiments with the cavity on resonance and immediately after that another 100 experiments with the cavity detuned by 1 MHz from the atomic resonance. The number of excitations and decays is recorded independently in both cases.

Up until now we could measure an effect of the cavity of about 10% lifetime reduction. A detailed analysis will be found in [76]. There are many reasons that might account for observing less than the theoretical value: the already small expected effect of 50% lifetime reduction is further decreased by bad centering of the ion in the cavity waist and the cavity node. The centering in the waist is done by comparing the frequency of Rabi oscillations driven by the cavity field as described in section (6.2.1) at different radial positions in the cavity mode. Changing the radial position cannot be done

⁵Inhibiting the transition by tuning the cavity off resonance is not observable due to the negligible solid angle subtended by the cavity.

without changing the axial position in the standing wave pattern. Therefore every time a radial change is made, again a field node has to be placed at the ion's position by changing the offset voltages of the piezos⁶. Moving the trap requires realigning the laser beams and the detection channels (CCD and PMT). Furthermore, driving Rabi oscillations as shown in figure (6.10) requires the perfect performance of two narrow band lasers (729 nm, 785 nm) and of the cavity lock. The slightest malfunction results in non-coherent excitation of the ion. All this leads to a tedious and time consuming procedure. A resulting effect of only few percent on the lifetime of about 1 s is hard to detect because the required small statistical error demands a large number of experiments i.e. the whole setup has to be stable for a long time.

Work on the detailed investigation of this topic is presently in progress and will be published in [76].

⁶This position is strongly influenced by drifts and hysteresis of the cavity piezos, making permanent checks necessary.

Chapter 7

Summary and Outlook

This thesis reports on the setup of an apparatus to perform cavity QED experiments with a single trapped $^{40}\text{Ca}^+$ ion and the subsequent measurements thereon performed. The technically involved apparatus combines a standard trap design [10, 8], moveable from several μm up to a few mm, with a high finesse cavity. To stabilise the cavity to the $S_{1/2} \leftrightarrow D_{5/2}$ quadrupole transition at 729 nm without this light in the cavity, the setup of a transfer lock is required. This is realised using a diode laser at 785 nm that is locked to the same reference cavity that the Ti:sapphire laser at 729 nm is stabilised to. After characterising the Paul-type trap and the demonstration of coherent dynamics on the quadrupole transition, more sophisticated experiments on the ion-cavity coupling have been performed. In a series of measurements the spatial variation of the standing wave cavity light field has been explored using the localised trapped ion as a nanoscopic probe. It was found that the ion's position in the standing wave could be determined with a precision of up to $\approx \lambda/100$. Additionally, the dynamics of the cavity-ion coupling has been investigated. This was achieved by exciting the ion using the cavity which is scanned to yield resonance with the driving laser. Furthermore, motional states have been coupled to the cavity field confirming the orthogonal coupling of carrier and first-order sideband transitions at field nodes and antinodes due to the opposite symmetry of the matrix elements for standing wave excitation. Finally, coherent interaction of cavity mode and ion has been demonstrated by driving Rabi oscillations with the cavity field and a lifetime reduction of the $D_{5/2}$ state by the resonant cavity of approximately 10% has been detected. The latter result will be discussed and presented thoroughly in [76].

The next experimental goal is the measurement of the dependency of the enhanced spontaneous emission on the position in the standing wave. It is made difficult by the drifts of the ion position in the standing wave during

the time that is necessary to determine a statistically significant effect [76].

The low finesse of the cavity in the present apparatus is due to sealing problems that made a second bakeout necessary: during this process the finesse decreased from 240000 to 35000. For designing a new apparatus a few changes in the setup are therefore suggested. The current glass cell design appears to have more disadvantages than advantages. Several problems were encountered in trying to obtain a proper seal to the steel base plate. In addition, the fact that the cell cannot be anti-reflection coated using standard techniques leads to a higher straylight level than in conventional vessels. The accessibility from all directions proves not to be a real advantage because it is reduced by the size and shape of inner parts anyway (such as, for example, the cavity mount). Having only one opening to the vacuum chamber leads to a compact but on the other hand rather cramped assembly that requires the precise alignment of the components.

Another part of the experiment which can be improved is the trap-cavity assembly. In the present setup the decision was made to move the trap relative to the fixed cavity. Therefore movements of trap relative to cavity have no effects on the coupling of the laser to the cavity mode. On the other hand it is a big disadvantage: by moving the trap all other laser beams, as well as the fluorescence detection beam, are influenced and misaligned. This makes it difficult to find the center of the cavity waist experimentally, because almost all beams and the detection optics have to be aligned after each adjustment of the trap position. Keeping instead the trap fixed and adjusting the cavity would appear to be a much simpler method, because the coupling of the laser beams to the cavity mode can be recovered quite easily, after some experience, if it is not completely misaligned. Most notably, the transmission signal is a clear and simple measure of the amount of light coupled into the cavity. With this scheme the ion, its cooling and the detection are not influenced at all and therefore it should be possible to find the center of the cavity waist much faster.

A final remark about a potential improvement concerns the cavity. To lock the cavity so that it is resonant with the 729 nm light without using the light itself but rather the 785 nm light, resonance on both wavelengths is necessary. Extending the scan range of one of the cavity mirrors to several free spectral ranges would increase the chance of a double resonance for 729 nm and 785 nm light making experimental life sometimes a bit easier.

The work presented in this thesis is one of the key steps in cavity QED with single trapped ions. Worldwide there are only a few experiments exploring this topic, although there are many ideas that can be implemented

in the near future. One of the uses of the new apparatus currently being designed in our group is for example the detection of the photons emitted into the cavity mode. This would allow such applications as triggered single photon emission and the realisation of the atom–photon interface. In the new apparatus a linear ion trap is going to be used and two or more ions can be coupled to a common cavity mode. Experience and technologies of the present CQED trap as well as of the linear trap operated in our group are merged in this project and allow a variety of interesting experiments to be performed.

Appendix A

Quadrupole Matrix Elements

To calculate the quadrupole matrix elements

$$\langle S_{1/2}, -1/2 | (\mathbf{r} \cdot \mathbf{e})(\mathbf{r} \cdot \mathbf{k}) | D_{5/2}, -5/2 \rangle \quad (\text{A.1})$$

we use the equalities given in [15]:

$$\Omega_0 = \left| \frac{eE}{2\hbar} \langle 1 | (\mathbf{r} \cdot \mathbf{e})(\mathbf{r} \cdot \mathbf{k}) | 2 \rangle \right| = \frac{e|E|}{\hbar} \sqrt{\frac{\gamma_{\parallel}}{c\alpha k^3}} \cdot \sigma, \quad (\text{A.2})$$

where e is the electron charge, E the electric field amplitude, \mathbf{e} and \mathbf{k} are the polarisation and wavevector, γ_{\parallel} is the population decay rate of the upper level and $\alpha \approx 1/137$ is the fine structure constant. σ is a number depending on the transition¹ $|1\rangle = |j, m_j\rangle \leftrightarrow |2\rangle = |j', m'_j\rangle$ and the geometry. It is given by:

$$\sigma := \sqrt{\frac{15(2j'+1)}{4}} \left| \sum_{q=-2}^2 \begin{pmatrix} j & 2 & j' \\ -m_j & q & m'_j \end{pmatrix} c_{ij}^{(q)} \mathbf{e}_i^{(q)} n_j \right|, \quad (\text{A.3})$$

where $\mathbf{n} := \mathbf{k}/k$ and the $c_{ij}^{(q)}$ are given in [15]. The Wigner $3-j$ symbols are defined and calculated in [16]. For maximal coupling on the $S_{1/2}, m_j = -1/2 \leftrightarrow D_{5/2}, m_j = -5/2$ transition in $^{40}\text{Ca}^+$ we find:

$$\sigma = \sqrt{\frac{5}{8}}. \quad (\text{A.4})$$

From (A.2) we find:

$$|\langle 1 | (\mathbf{r} \cdot \mathbf{e})(\mathbf{r} \cdot \mathbf{k}) | 2 \rangle| = 2 \sqrt{\frac{\gamma_{\parallel}}{c\alpha k^3}} \cdot \sigma. \quad (\text{A.5})$$

¹ j is the total angular momentum quantum number, m_j is the magnetic quantum number.

Inserting the value for σ , using the relations: $k = 2\pi/\lambda$, $\gamma_{\parallel} = 2\gamma_{\perp}$ and $\alpha = e^2/(4\pi\epsilon_0\hbar c)$, we find the result given in equation (2.12):

$$|\langle S_{1/2}, -1/2 | (\mathbf{r} \cdot \mathbf{e})(\mathbf{r} \cdot \mathbf{k}) | D_{5/2}, -5/2 \rangle| = \frac{1}{e} \sqrt{\frac{5\gamma_{\perp}\lambda^3\epsilon_0\hbar}{2\pi^2}}. \quad (\text{A.6})$$

The calculation for dipole matrix elements is analogous, confer the equations in [15].

Appendix B

Normalised Scanrate

Consider a standing wave in a two mirror cavity (mirror distance L). On resonance we have:

$$\lambda \cdot \frac{n}{2} = \frac{c}{\nu} \cdot \frac{n}{2} = L, \quad (\text{B.1})$$

where n is the number of antinodes (for optical wavelengths usually a large number) and $\lambda \cdot \nu = c$ was used. We change now the length of the resonator by ΔL in some time Δt and ask for the change of the light frequency under the condition of resonance and constant number of antinodes. We find:

$$\frac{\Delta \nu}{\Delta t} = \frac{-c}{L^2} \cdot \frac{n}{2} \cdot \frac{\Delta L}{\Delta t} = \frac{-\nu}{L} \cdot \frac{\Delta L}{\Delta t}, \quad (\text{B.2})$$

where we used (B.1). From now on we omit the minus sign. The normalised scanrate ν_L is the scanrate $\Delta \nu / \Delta t$ in units of the HWHM of the cavity linewidth $\frac{c}{4L\mathcal{F}}$ per cavity decay time τ . We obtain:

$$\nu_L := \frac{\Delta \nu}{\Delta t} \cdot \frac{\tau}{\frac{c}{4\mathcal{F}L}} = \frac{2\mathcal{F}\omega\tau}{\pi c} \cdot \dot{L}, \quad (\text{B.3})$$

with $\omega := 2\pi \cdot \nu$ and $\Delta L / \Delta t = \dot{L}$.

Appendix C

Coupling a Qubit to an Optical High Finesse Cavity

Coupling a Single Atomic Quantum Bit to a High Finesse Optical Cavity

A. B. Mundt, A. Kreuter, C. Becher,* D. Leibfried,† J. Eschner, F. Schmidt-Kaler, and R. Blatt
Institut für Experimentalphysik, Universität Innsbruck, Technikerstraße 25, A-6020 Innsbruck, Austria
 (Received 5 February 2002; published 13 August 2002)

The quadrupole $S_{1/2}$ - $D_{5/2}$ optical transition of a single trapped Ca^+ ion, well suited for encoding a quantum bit of information, is coherently coupled to the standing wave field of a high finesse cavity. The coupling is verified by observing the ion's response to both spatial and temporal variations of the intracavity field. We also achieve deterministic coupling of the cavity mode to the ion's vibrational state by selectively exciting vibrational state-changing transitions and by controlling the position of the ion in the standing wave field with nanometer precision.

DOI: 10.1103/PhysRevLett.89.103001

PACS numbers: 32.80.Pj, 03.67.-a, 42.50.Ct

The coherent coupling of a single atom or ion to one mode of the electromagnetic field inside a high finesse optical resonator is of major interest for the implementation of quantum information processing schemes: Single atoms and ions are well suited for storing quantum information in long-lived internal states, e.g., by encoding a quantum bit (qubit) of information within the coherent superposition of the $S_{1/2}$ ground state and the metastable $D_{5/2}$ excited state of Ca^+ [1]. On the other hand, fast and reliable transport of quantum information over long distances is most easily achieved by using photons as qubit carriers. The interface between static and moving qubits is represented by the controlled interaction of a single atom and a single cavity mode, being the basic building block for distributed quantum networks [2]. Deterministic ion-cavity coupling was demonstrated recently by using a single trapped ion as a nanoscopic probe of an optical field [3]. A second application of atom-cavity coupling within the field of quantum information processing is the realization of a deterministic source of single photons [4,5] or sequences of entangled single-photon wave packets [6]. More generally, trapped ions that are cooled to their lowest vibrational state [7,8] and interact with a quantized cavity field might allow for entangling three quantum subsystems [9,10], i.e., internal electronic states, quantum vibrational mode, and single-mode cavity field. Another application of coupling a trapped ion to a cavity mode is utilizing the cavity internal standing wave (SW) field [11] or the cavity-modified spontaneous emission [12] and coherent scattering [13] for cooling the ion's vibrational state well below the Doppler limit.

In this paper we demonstrate coherent coupling of the quadrupole $S_{1/2}$ - $D_{5/2}$ qubit transition of a single Ca^+ ion to a mode of a high finesse optical cavity. The ion is trapped and placed with high precision at an arbitrary position in the SW field of the cavity for several hours of interaction time. We also achieve deterministic coupling of the cavity mode to the ion's vibrational state by selectively exciting state-changing transitions with the cavity light tuned to a vibrational sideband of the $S_{1/2}$ - $D_{5/2}$ resonance. These demonstrations are important steps towards realization of the experiments discussed above.

The Ca^+ ion is stored in a spherical Paul trap [14] placed in the center of a near-confocal resonator. The ion is laser cooled to the Lamb-Dicke regime, confining its spatial wave packet to a region much smaller than the optical wavelength. We detect the coupling of ion and fundamental TEM_{00} cavity mode by injecting an external light field at 729 nm into the cavity and recording the excitation on the $S_{1/2}$ - $D_{5/2}$ transition. The excitation probability is monitored via the electron shelving technique [8,15], i.e., by probing the fluorescence on the $S_{1/2}$ - $P_{1/2}$ dipole transition (see Fig. 1).

The experimental setup is schematically shown in Fig. 1. The three-dimensional rf-Paul trap consists of an elliptical ring electrode with average diameter of 1.4 mm and two

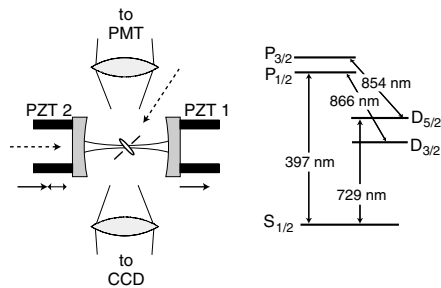


FIG. 1. Schematic experimental setup (left) and Ca^+ level scheme (right). PZT1 denotes the offset piezo, and PZT2 the scan piezo (see text). A photomultiplier tube (PMT) is used to record fluorescence on the $S_{1/2}$ - $P_{1/2}$ transition, and the CCD camera monitors the ion's position. The following stabilized laser sources are used in the experiment: two cavity-locked diode lasers at 866 and 854 nm with linewidths of ≈ 10 kHz and two Ti:Sa lasers at 729 nm (≈ 1 kHz linewidth) and 794 nm (< 300 kHz linewidth), where the 794 nm laser is resonantly frequency doubled to obtain 397 nm. The whole laser system is described in more detail elsewhere [1]. The dotted arrows indicate directions of laser beams: 729 nm excitation laser along the direction of the cavity axis and 397 nm cooling laser, 854 and 866 nm auxiliary lasers at a certain angle to the trap axis (shown only schematically).

end caps with a spacing of 1.2 mm (material: 0.2 mm molybdenum wire). The secular frequencies ($\omega_x, \omega_y, \omega_z$) are $2\pi \times (2.9, 3.9, 7.4)$ MHz at a rf drive field power of 1 W. Here z denotes the direction of the trap axis, which is 45° to the cavity axis. The x and y radial directions both include an angle of $\approx 45^\circ$ with the plane spanned by the cavity and trap axes. A magnetic field of 3 G perpendicular to the cavity axis provides a quantization axis and a frequency splitting of Zeeman components of the $S_{1/2}-D_{5/2}$ transition. Calcium ions are loaded into the trap from a thermal atom beam by a two-step photoionization process using diode lasers near 423 and 390 nm [16]. The trap is placed in the center of a near-confocal resonator with finesse $\mathcal{F} = 35000$ at 729 nm, waist radius $\omega_0 = 54 \mu\text{m}$, mirror separation $L = 21$ mm, and radius of curvature $R_M = 25$ mm. Cylindrical piezoceramics (PZT) allow fine-tuning of the cavity length across approximately 1.5 free spectral ranges.

The coherent coupling of the ion to the cavity field is measured in three steps as follows.

(i) *Preparation*: First we use Doppler cooling on the $S_{1/2}-P_{1/2}$ transition at 397 nm (see Fig. 1) to cool the ion into the Lamb-Dicke regime. A repumper laser at 866 nm inhibits optical pumping into the $D_{3/2}$ level. From coherent dynamics (Rabi oscillations) on the carrier and first motional sidebands [8] we determine typical mean vibrational quantum numbers after Doppler cooling $(\bar{n}_x, \bar{n}_y, \bar{n}_z) = (20 \pm 5, 4 \pm 1, 6 \pm 1)$. From these mean phonon numbers and the secular frequencies given above we calculate an rms extension of the ion's motional wave packet of 25 ± 5 nm in the direction of the cavity axis, much smaller than the wavelength of 729 nm. After cooling, the ion is prepared in the $S_{1/2}$ ($m = -1/2$) substate by optical pumping with σ^- radiation at 397 nm.

(ii) *Interaction*: The laser at 729 nm is set to a fixed detuning Δ from the $S_{1/2}-D_{5/2}$ ($m = -1/2$ to $m' = -5/2$) qubit transition. We inject the laser light into the TEM_{00} mode of the cavity and scan the cavity with a voltage ramp applied to one of the PZTs (scan PZT). When the cavity reaches resonance with the laser frequency, it fills with light and the ion is excited. A constant voltage is applied to the other PZT (offset PZT) that determines the ion's position relative to the SW field.

(iii) *State analysis*: The final step is state detection by electron shelving. Fluorescence on the $S_{1/2}-P_{1/2}$ dipole transition at 397 nm is used to discriminate with high efficiency ($> 99\%$) between excited state (electron shelved in $D_{5/2}$, no fluorescence) and ground state (fluorescence).

In order to obtain an excitation spectrum, the 729 nm laser is tuned over the quadrupole transition in steps of about 1 kHz. For any given laser detuning Δ the sequence (i)–(iii) is repeated 100 times to determine the excitation probability.

In our first experiment we probe the ion's response to temporal variations of the intracavity field by placing it

close to a node of the SW field [17] and varying the cavity scan rate. The sign of the voltage ramp applied to the scan PZT determines whether the scan mirror moves towards the offset mirror or away from it. For a negative (positive) scan rate, i.e., mirrors moving towards each other (apart), the intracavity field is Doppler blueshifted (redshifted), and thus the excitation spectrum will be redshifted (blue-shifted), as the excitation laser detuning has to compensate for the Doppler shift. The scan velocity is expressed in units of a normalized scan rate ν_L [18,19], corresponding to the frequency shift in units of HWHM cavity linewidths per cavity storage time: $\nu_L = 2\mathcal{F}\omega\dot{L}\tau_s/\pi c$, with laser frequency ω , cavity length variation \dot{L} , and cavity (energy) storage time $\tau_s = \mathcal{F}L/\pi c$. The experimental results for scan rates $0.16 > \nu_L > 0.69$ are shown in Fig. 2. The excitation spectra show the expected blueshift (redshift) for increasing positive (negative) scan rates and a broadening

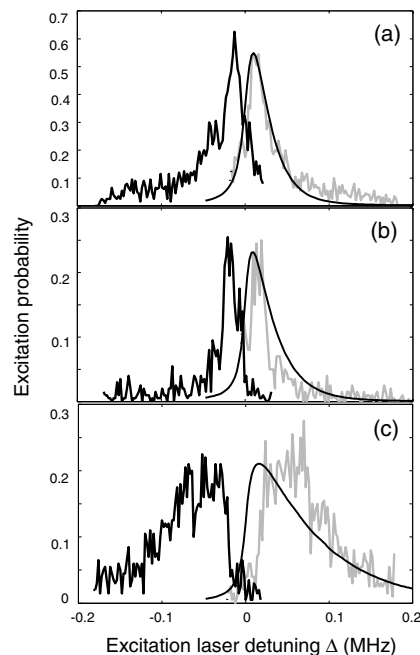


FIG. 2. Excitation spectra of the $S_{1/2}-D_{5/2}$ transition for different cavity scan rates: $\nu_L = \pm 0.16$ (a), ± 0.23 (b), and ± 0.69 (c). Blueshifted excitation spectra are drawn as gray lines on the right hand side of the diagrams, and superimposed solid lines show the theoretical simulation. The parameters used for the simulations are excitation laser bandwidth $\Delta\nu_{\text{Laser}} = 6$ kHz, natural linewidth of the $S_{1/2}-D_{5/2}$ transition $\Delta\nu_{SD} = 0.17$ Hz, maximum Rabi frequency at the transition center wavelength $\Omega_{\text{max}} = 15.5$ kHz (a), 11 kHz (b), and 25 kHz (c), and the cavity parameters given in the text.

due to the Doppler effect. An excitation probability of more than 0.5 as in Fig. 2(a) clearly demonstrates that the ion is coherently interacting with the intracavity field. We theoretically model the excitation for different laser detunings Δ by numerically integrating two-level Bloch equations using the time-dependent intracavity field calculated from the pertaining differential equations [18,19]. The results of the theoretical simulation for positive scan rates are shown as solid lines superimposed on the blue-shifted spectra in Fig. 2. The calculated and experimental spectra show good agreement for small scan rates [Figs. 2(a) and 2(b)]. For larger scan rates [Fig. 2(c)] the centers of the spectra are slightly shifted. We assume that this shift is caused by nonlinearities and hysteresis effects of the PZT motion. Although we kept the excitation power constant in the experiments, we left the Rabi frequency Ω_{\max} as a fit parameter to account for variations in excitation due to thermal drift of the cavity shifting the node of the SW away from the ion's position.

The second type of experiment probes the ion's response to spatial field variations. For this, we leave the scan rate fixed at a small value, allowing for stable scans with only little perturbations of the excitation spectrum, as in Fig. 2(a). The intensity of the 729 nm laser is adjusted such that the excitation is kept well below saturation. The offset voltage of both scan PZT and offset PZT is then varied simultaneously in such a way that the SW in the cavity is shifted longitudinally with respect to the location of the ion. The position-dependent excitation probability is determined by fitting each excitation spectrum with a Lorentzian and adopting the peak value. Figure 3 displays these values as a function of the PZT offset voltage. Error bars given for representative data points in Fig. 3 are due to PZT hysteresis (abscissa) and the errors of the fits to the excitation spectra (ordinate). The excitation probability varies spatially with the intensity of the SW [17]. A theo-

retical Bloch-equation analysis as described above predicts a nearly pure "sin²" spatial variation, deviating by less than 1%. From a sin² fit to the data points we obtain the contrast ratio (visibility V) of the position-dependent excitation, $V = (96.3 \pm 2.6)\%$. This very high visibility results from the strong confinement of the ion's wave function. The laser-cooled ion, oscillating with its secular frequencies and with thermally distributed amplitudes, has a rms spatial extension along the cavity axis of a_c , leading to a reduction of the excitation contrast by a factor of $\exp[-2(2\pi a_c/\lambda)^2]$. From the measured visibility V we find $a_c = 16^{+5}_-7$ nm. The small value of the extension a_c shows that in this experiment we cool the ion close to the Doppler limit (13 nm).

A necessary condition for all experiments relying on ion-cavity mode coupling is the ability to place the ion at a certain position of the intracavity SW field with high precision and high reproducibility [3]. In our experiment, the precision of positioning the center of the ion's wave function, using a measurement as in Fig. 3, is limited by the uncertainty in the measured excitation probability. This uncertainty is due to a statistical error, i.e., the finite number of state detection measurements, and systematic errors such as fluctuations of laser intensity and wavelength, drift, and jitter of scan PZT, etc. [20]. From the uncertainties in excitation probability (error bars in Fig. 3) we deduce a spatial precision between 7 nm ($\approx \lambda/100$) at the position of largest slope and 12 and 36 nm at minimum or maximum excitation, respectively. We note, however, that the precision can be enhanced by averaging over a larger number of state detection measurements.

Many schemes for quantum information processing with trapped ions rely on coherent interaction not only with the internal state but also with the motional degrees of freedom. A controlled coupling to the motional quantum state is a precondition for realizing such schemes. In order to demonstrate this motion-dependent coupling, we recorded excitation probabilities of the ion at a fixed cavity scan rate ($\nu_L = -0.23$), for different positions within the SW, and with the laser at 729 nm now tuned to either the carrier (no change of vibrational quantum number, $\Delta n = 0$) or the red axial sideband ($\Delta n = -1$, laser detuned by $-\omega_z$) of the $S_{1/2}-D_{5/2}$ transition. In both cases, the intensity of the laser was adjusted such that the excitations of carrier and sideband were comparable and were kept well below saturation. In this experiment we determine the integral excitation, i.e., the area of the respective excitation spectra, as the spectra show an asymmetric line shape [cf. Figs. 2(b) and 2(c)]. As displayed in Fig. 4, carrier and sideband excitations both map the SW spatial field variation, but the traces are shifted by a phase factor of π . This phase shift arises due to symmetry characteristics of the transition matrix elements of carrier and sideband transitions in a SW field [11,21]: The spatial part of the quadrupole transition matrix element is proportional to $\langle n' | \exp(ikx) | n \rangle$ for a traveling wave (TW) and $\langle n' | \cos(kx) | n \rangle$ for a SW with

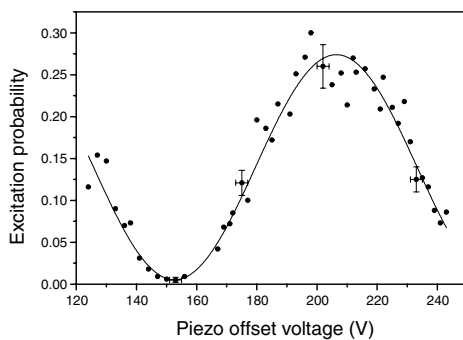


FIG. 3. Excitation probability on the $S_{1/2}-D_{5/2}$ transition of a single trapped Ca^+ ion as a function of the PZT offset voltage, i.e., at various positions in the intracavity standing wave field. The solid line represents a \sin^2 function fitted to the data points.

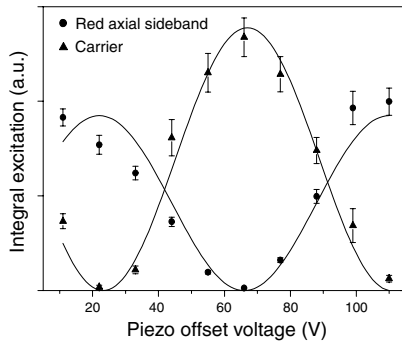


FIG. 4. Integral excitation on the carrier (triangles) and the red axial sideband (circles) of the $S_{1/2}$ - $D_{5/2}$ transition as a function of the PZT offset voltage, i.e., at various positions in the intracavity standing wave field. The solid lines represent fits of \sin^2 functions to the data points.

the electric field $E \propto \sin(kx)$ [17]. Here n and n' are the vibrational quantum numbers in the $S_{1/2}$ and $D_{5/2}$ levels, respectively, k is the wave number, and x is the ion's position in the field. For a TW, all vibrational states (n, n') can be coupled as $\exp(ikx)$ contains even and odd powers of kx . On the contrary, for a SW $\langle n' | \cos(kx) | n \rangle$ has to be expanded into even or odd powers of kx depending on the ion's position, e.g., $x = 0$ close to a node or $x = \lambda/4$ close to an antinode. Thus, transitions changing the phonon number by even or odd integers can be excited only at different positions in the SW. The red sideband transition ($\Delta n = -1$) couples maximally at antinodes of the SW, whereas the carrier transition ($\Delta n = 0$) couples maximally at nodes.

The high-contrast orthogonal coupling of carrier and sideband transitions to the cavity mode facilitates applications such as cavity-assisted cooling in a SW [11] or the Cirac-Zoller quantum-computing scheme [22]. Both schemes rely on driving vibrational sideband transitions and benefit from suppressing off-resonant carrier transitions which induce motional heating or impose a limit on the attainable gate speed [23], respectively. Furthermore, the ion-cavity coupling allows for demonstrating and utilizing cavity-modified spontaneous emission: we calculate the cooperativity parameter $C = g^2/2\kappa\gamma = 0.52$, with our experimental ion-field coupling constant $g = 2\pi \times 134$ Hz, cavity decay rate $\kappa = 2\pi \times 102$ kHz, and spontaneous emission rate $\gamma = 2\pi\Delta\nu_{SD} = 2\pi \times 0.17$ Hz. Because of the coupling, the spontaneous emission rate is enhanced by the Purcell factor $F = 2C + 1 = 2.04$, and the fraction of spontaneous emission from the $D_{5/2}$ level emitted into the cavity mode is $\beta = 2C/(2C + 1) = 51\%$. This is sufficient for demonstrating cavity-assisted cooling via destructive quantum interference of heating transitions [12], or triggered single-photon emission from the $D_{5/2}$

level. Improvement of the latter scheme and realization of the atom-photon interface [2] can readily be achieved by employing an adiabatic transfer technique [4,5] and using a cavity with higher finesse ($\geq 100\,000$).

In summary, we have demonstrated coherent coupling of electronic and motional states of a single trapped ion to a single field mode of a high finesse cavity. The position of the ion within the standing wave can be determined with a precision of up to $\lambda/100$. As the electronic quadrupole transition in Ca^+ is one of the candidates for implementing a quantum bit, our experiments are a key step towards realization of quantum-computing and communication schemes with trapped ions that require a controlled interaction of ion and cavity field.

This work is supported by the Austrian "Fonds zur Förderung der wissenschaftlichen Forschung" (SFB15), by the European Commission [TMR networks "QI" and "QSTRUCT" (ERB-FRMX-CT96-0087 and -0077), IHP network "QUEST" (HPRN-CT-2000-00121), and IST/FET program "QUBITS" (IST-1999-13021)], and by the "Institut für Quanteninformation GmbH".

*Electronic addresses: Christoph.Becher@uibk.ac.at,
http://heart-c704.uibk.ac.at/Welcome.html

[†]Present address: Time and Frequency Division, National Institute of Standards and Technology, Boulder, CO 80305.

- [1] H. C. Nägerl *et al.*, Phys. Rev. A **61**, 023405 (2000).
- [2] J. I. Cirac *et al.*, Phys. Rev. Lett. **78**, 3221 (1997).
- [3] G. R. Guthöhrlein *et al.*, Nature (London) **414**, 49 (2001).
- [4] C. K. Law and H. J. Kimble, J. Mod. Opt. **44**, 2067 (1997).
- [5] M. Hennrich *et al.*, Phys. Rev. Lett. **85**, 4872 (2000).
- [6] K. M. Gheri *et al.*, Phys. Rev. A **58**, R2627 (1998).
- [7] D. M. Meekhof *et al.*, Phys. Rev. Lett. **76**, 1796 (1996).
- [8] Ch. Roos *et al.*, Phys. Rev. Lett. **83**, 4713 (1999).
- [9] V. Bužek *et al.*, Phys. Rev. A **56**, 2352 (1997).
- [10] F. L. Semião, A. Vidiella-Barranco, and J. A. Roversi, Phys. Rev. A **64**, 024305 (2001).
- [11] J. I. Cirac *et al.*, Phys. Rev. A **46**, 2668 (1992).
- [12] J. I. Cirac, M. Lewenstein, and P. Zoller, Phys. Rev. A **51**, 1650 (1995).
- [13] V. Vuletić, H. W. Chan, and A. T. Black, Phys. Rev. A **64**, 033405 (2001).
- [14] W. Paul, Rev. Mod. Phys. **62**, 531 (1990).
- [15] H. Dehmelt, Bull. Am. Phys. Soc. **20**, 60 (1975).
- [16] S. Gulde *et al.*, Appl. Phys. B **73**, 861 (2001).
- [17] Note that the atomic quadrupole moment couples to the gradient of the electric field. The maximum excitation thus occurs at the nodes of the standing wave.
- [18] H. Rohde *et al.*, J. Opt. Soc. Am. B **19**, 1425 (2002).
- [19] M. J. Lawrence *et al.*, J. Opt. Soc. Am. B **16**, 523 (1999).
- [20] J. Eschner *et al.*, Nature (London) **413**, 495 (2001).
- [21] M. Šašura and V. Bužek, quant-ph/0112041.
- [22] J. I. Cirac and P. Zoller, Phys. Rev. Lett. **74**, 4091 (1995).
- [23] A. Steane *et al.*, Phys. Rev. A **62**, 042305 (2000).

Appendix D

Coherent Coupling of a Single Ion to a High Finesse Cavity

A. B. MUNDT
 A. KREUTER
 C. RUSSO
 C. BECHER[✉]
 D. LEIBFRIED*
 J. ESCHNER
 F. SCHMIDT-KALER
 R. BLATT

Coherent coupling of a single $^{40}\text{Ca}^+$ ion to a high-finesse optical cavity

Institut für Experimentalphysik, Universität Innsbruck, Technikerstraße 25, 6020 Innsbruck, Austria

Received: 23 August 2002

Published online: 8 January 2003 • © Springer-Verlag 2003

ABSTRACT We demonstrate coherent coupling of the quadrupole $S_{1/2} \leftrightarrow D_{5/2}$ optical transition of a single trapped $^{40}\text{Ca}^+$ ion to the standing wave field of a high-finesse cavity. The dependence of the coupling on temporal dynamics and spatial variations of the intracavity field is investigated in detail. By precisely controlling the position of the ion in the cavity standing wave field and by selectively exciting vibrational state-changing transitions the ion's quantized vibration in the trap is deterministically coupled to the cavity mode. We confirm coherent interaction of ion and cavity field by exciting Rabi oscillations with short resonant laser pulses injected into the cavity, which is frequency-stabilized to the atomic transition.

PACS 32.80.Pj; 03.67.-a; 42.50.Ct

1 Introduction

Laser-cooled trapped atoms or ions are ideally suited systems for the investigation and implementation of quantum information processing [1]. The combination of a Paul-type ion trap [2] with laser cooling leads to unique properties of trapped cold ions, such as localization of the single particle to less than a few tens of nanometers, control of the motional state down to the zero-point of the trapping potential and a high degree of isolation from the environment and thus a very long time available for manipulations and interactions at the quantum level. The very same properties make single trapped atoms and ions well suited for storing quantum information in long-lived internal states, e.g. by encoding a quantum bit (qubit) of information within the coherent superposition of the $S_{1/2}$ ground state and the metastable $D_{5/2}$ excited state of Ca^+ [3]. However, this stored information is 'spatially static' with respect to transport of quantum information over distances exceeding the trap dimensions. A much better suited carrier of quantum information for fast and reliable transport over long distances are photons. An interface between static and moving qubits requires the controlled coherent interaction of a single atom and a single cavity mode, this being the basic

building block for distributed quantum networks [4]. For an experimental implementation of such a scheme one needs to understand and control the dynamics of the atom–cavity coupling. Thus, the demonstration of deterministic *coherent* coupling of a single ionic qubit to one mode of the electromagnetic field inside a high-finesse optical resonator and the detailed investigation of this coupling [5] are of major interest for the implementation of quantum information processing with trapped ions. Deterministic excitation of cavity-induced fluorescence on the short-lived $S_{1/2}$ – $P_{1/2}$ dipole transition in Ca^+ was demonstrated recently, thereby utilizing a single trapped ion as a nanoscopic probe of an optical field [6].

Another application closely related to the atom–photon interface is the triggered emission of single photons from the coupled atom–cavity system [7, 8] or sequences of entangled single-photon wave packets [9]. Efficient deterministic emission of single photons into a well-defined spatial mode is a prerequisite for quantum key distribution [10] and linear optics quantum computation [11].

The ability to precisely place an ion at an arbitrary position within a standing wave (SW) field and the highly orthogonal coupling of different vibrational-state-changing transitions to the SW field can be utilized for cooling the ion's vibrational state well below the Doppler limit [12]. If, in addition, the coupling of atom and cavity mode is strong enough to induce a modification of the atom's spontaneous emission properties [13], one can demonstrate cavity-assisted cooling via destructive quantum interference of heating transitions [14].

Finally, the strong coupling of trapped ions that are cooled to their lowest vibrational state [15, 16] with a quantized cavity field might allow for entangling three quantum subsystems [17, 18], i.e. internal electronic states, quantum vibrational mode and single-mode cavity field.

In this paper we demonstrate important first steps towards the above experiments by coherently coupling the quadrupole $S_{1/2} \leftrightarrow D_{5/2}$ transition of a single trapped Ca^+ ion to a mode of a high-finesse optical cavity. We investigate the coupling by probing the ion's response to dynamical and spatial variations of the intracavity field. The ion can be placed with high precision at an arbitrary position in the SW field of the cavity. We achieve deterministic coupling of the cavity mode to the ion's vibrational state by selectively exciting state-changing transitions with the cavity light tuned to a vibrational sideband of the $S_{1/2} \leftrightarrow D_{5/2}$ resonance. We prove that the interaction of

✉ E-mail: christoph.becher@uibk.ac.at

*Present address: Time and Frequency Division, National Institute of Standards and Technology, Boulder, CO 80305, USA

ion and cavity field is coherent by exciting Rabi oscillations through the field in the frequency-stabilized cavity.

2 Experimental setup

2.1 Trap and cavity setup

The $^{40}\text{Ca}^+$ ion is stored in a spherical Paul trap [2] placed in the center of a near-confocal resonator. The ion is laser-cooled to the Lamb–Dicke regime, confining its spatial wave packet to a region much smaller than the optical wavelength. We detect the coupling of ion and fundamental TEM_{00} cavity mode by injecting a light field at 729 nm into the cavity and recording the excitation on the $S_{1/2} \leftrightarrow D_{5/2}$ transition. The excitation probability is monitored via the electron-shelving technique [16, 19], i.e. by probing the fluorescence on the $S_{1/2} - P_{1/2}$ dipole transition (see Fig. 1).

The following stabilized laser sources are used in the experiment: two cavity-locked diode lasers at 866 nm and 854 nm with line widths of ≈ 10 kHz and two Ti:Sa lasers at 729 nm (≈ 1 -kHz line width) and 794 nm (< 300 -kHz line width), of which the 794-nm laser is resonantly frequency-doubled to obtain 397 nm. The whole laser system is described in more detail elsewhere [3].

The experimental setup of trap and cavity is schematically shown in Fig. 2. The three-dimensional RF Paul trap consists of an elliptical ring electrode with average diameter of 1.4 mm and two end caps with a spacing of 1.2 mm (material: 0.2-mm molybdenum wire). The secular frequencies ($\omega_x, \omega_y, \omega_z$) are $2\pi \times (2.9, 3.9, 7.4)$ MHz at a RF drive field power of 1 W. Here, z denotes the direction of the trap axis, which is at 45° to the cavity axis. The x and y radial directions both include an angle of $\approx 45^\circ$ with the plane spanned by the cavity and the trap axis. A magnetic field of 3 G perpendicular to the cavity axis provides a quantization axis and a frequency splitting of Zeeman components of the $S_{1/2} \leftrightarrow D_{5/2}$ transition. Calcium ions are loaded into the trap from a thermal atom beam by a two-step photoionization process using diode lasers near 423 nm and 390 nm [20]. The trap is placed in the center of a near-confocal resonator with finesse $\mathcal{F} = 35\,000$ at 729 nm, waist radius $\omega_0 = 54 \mu\text{m}$, mirror separation $L = 21$ mm and radius of curvature $R_M = 25$ mm. Cylindrical piezoceramics (PZTs) allow fine tuning of the cavity length across approximately 1.5 free spectral ranges. In the following this cavity is denoted as the ‘trap cavity’.

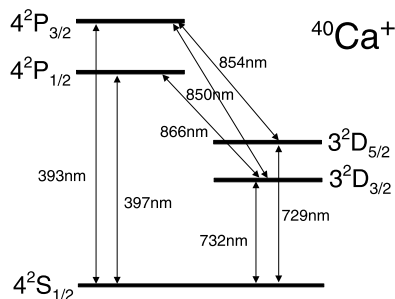


FIGURE 1 $^{40}\text{Ca}^+$ level scheme

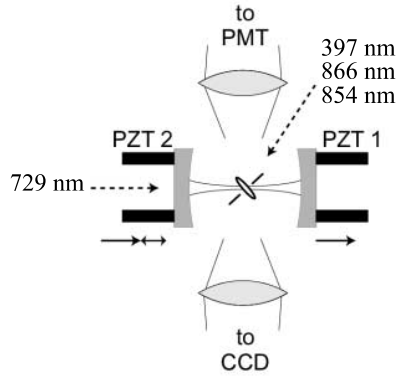


FIGURE 2 Schematic experimental setup. PZT1 denotes the offset piezo, PZT2 the scan piezo. A photomultiplier tube (PMT) is used to record fluorescence on the $S_{1/2} - P_{1/2}$ transition and the CCD camera monitors the ion's position. The dotted arrows indicate directions of laser beams: a 729-nm excitation laser along the direction of the cavity axis and a 397-nm cooling laser, 854-nm and 866-nm auxiliary lasers at a certain angle to the trap axis (only shown schematically)

The ion can be excited by a traveling wave using a free 729-nm laser beam at a certain angle to the cavity axis or by the SW built up in the cavity after injecting a 729-nm laser beam into the cavity mode. The position of the ion relative to nodes and anti-nodes of the SW can be controlled by adjusting the offsets of both PZTs.

2.2 Frequency stabilization of the trap cavity

In order to study stationary coherent interaction of an atom and a cavity mode it is necessary to stabilize the cavity resonance frequency to the atomic transition frequency. In order to avoid that resonant light present in the cavity perturbs the controlled atom–cavity interaction, we use a 785-nm diode laser for the stabilization, this being far off-resonant to transitions at 729 nm. The basic scheme of the transfer lock is as follows: we frequency lock the 785-nm diode laser to the same ultra-stable reference cavity (see [3]) as the 729-nm Ti:Sa laser. By stabilizing the trap cavity to the diode laser frequency, the lengths of the reference and the trap cavity are fixed relative to each other. Furthermore, the length of the trap cavity is fixed relative to the wavelength of the 729-nm Ti:Sa laser. By applying an appropriate frequency shift to the diode laser, the length of the trap cavity is adjusted to achieve resonance for 729 nm.

Figure 3 illustrates the setup of the diode laser at 785 nm and its stabilization to the reference cavity. The single-mode laser diode (80-mW maximum output power) is temperature-stabilized to a few millikelvin. An external holographic grating with 1800 lines/mm in Littrow configuration creates an extended tuneable resonator. The grating is mounted on a precision mirror holder; fine tuning is achieved by a PZT. The elements described so far are enclosed in a stable aluminum case kept at a constant temperature of $(20 \pm 0.1)^\circ\text{C}$ by circulating water. After passing through an optical diode with 60-dB isolation the light is split by a polarizing beam splitter. The part of the light being used for the Pound–Drever–

MUNDT et al. Coherent coupling of a single $^{40}\text{Ca}^+$ ion to a high-finesse optical cavity

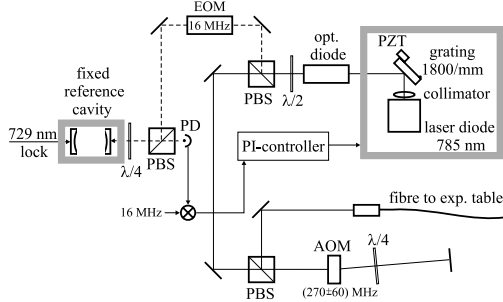


FIGURE 3 Setup of the 785-nm diode laser with extended cavity (Litrow configuration) and frequency stabilization to the reference cavity. The laser beam (≈ 35 mW) is split into a lock beam (≈ 2 mW, *dashed line*) and an experiment beam that is frequency-shifted in a double-pass configuration (*solid line*). Laser line width: $\Delta\nu_{785} = (1.8 \pm 0.1)$ kHz. For more details see text

Hall lock [21] to the reference cavity (FSR = 750 MHz) is phase-modulated with an electro-optical modulator (EOM) at 16 MHz. The error signal is fed to a PI controller acting on the laser diode current (fast branch) as well as on the grating PZT (slow branch). The light not used for the lock is directed through an acousto-optical modulator (AOM) (double pass), allowing for a continuous frequency shift of approximately ± 120 MHz, and is sent to the trap cavity via an optical fiber.

Figure 4 shows the setup of the trap cavity lock to the diode laser at 785 nm. The stabilized 785-nm light leaving the optical fiber is phase-modulated by an EOM at 16 MHz and is coupled into the trap cavity (from the right in Fig. 4) via a polarizing beam splitter. The 729-nm light is coupled into the cavity from the opposite side (left in Fig. 4). On the right-hand side of the cavity, the light is dispersed by a grating (1200 lines/mm) to separate the 785-nm reflected light from the 729-nm transmitted light, which is monitored by a CCD camera and a photodiode. The first-order grat-

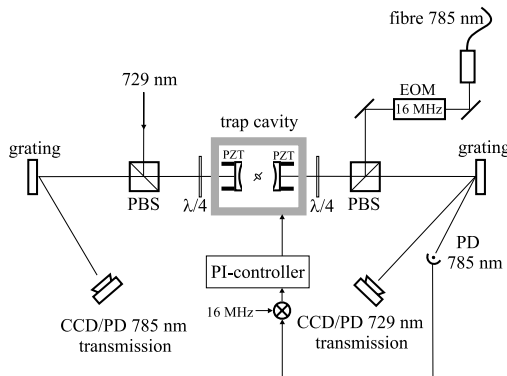


FIGURE 4 Setup of the trap-cavity lock. The light at 785 and 729 nm is coupled into the cavity from opposite directions. Gratings (1200 lines/mm) on both sides separate the beams and ensure clear control of the transmissions on both wavelengths without perturbation by reflections of the other light. For more details see text

ing reflection at 785 nm is focused onto a fast photodiode to obtain a Pound–Drever–Hall error signal after mixing with the modulation frequency. The error signal is processed in a PI controller acting on one of the trap-cavity PZTs. On the left-hand side, again a grating is used to separate the transmitted 785-nm light from the reflected 729-nm light. The 785-nm transmission is monitored on a CCD as well as on a photodiode.

The experimental procedure to achieve double resonance of the trap cavity is as follows: by scanning the trap cavity, transmission on the 729-nm TEM₀₀ mode is recorded. Now the wavelength of the diode laser has to be chosen in such a way that the 785-nm light is also resonant for both the reference and the trap cavities within the range of ± 120 MHz, this being covered by the double-pass AOM. Usually, this can be achieved by current tuning the diode to one of its longitudinal modes.

3 Experiments on ion–cavity coupling

In the following, we report four different experiments exploring various aspects of the ion–cavity coupling: First, we probe the ion’s response to temporal variations of the cavity internal field by scanning the cavity over the resonance with the incident laser light, thus imprinting a phase and amplitude modulation on the cavity field [22, 23]. Second, using the same scanning excitation technique we detect the ion’s response to spatial variations of the intracavity SW field (mapping of the longitudinal field distribution). Third, we investigate coupling of the ion’s vibrational modes to the cavity field by comparing the excitation on the carrier transition and on the first vibrational sideband at different positions in the SW. Finally, we observe coherent interaction of ion and cavity field by exciting Rabi oscillations with short resonant laser pulses coupled into the frequency-stabilized cavity.

3.1 Measurement procedures

The general procedure for all experiments is the following:

- The ion is Doppler-cooled and prepared in the electronic ground state.
- A sequence of laser pulses is applied to the ion.
- The final electronic state is detected.

These three steps are described in detail in the following (cf. Fig. 5).

First, the ion is Doppler-cooled for 1.9 ms on the $S_{1/2} - P_{1/2}$ transition. During cooling the 854-nm laser is switched on to remove any population in the metastable $D_{5/2}$ state. In addition, we irradiate the ion with a laser beam at 866 nm at all times to prevent shelving in the metastable $D_{3/2}$ state. From coherent dynamics (Rabi oscillations) on the carrier and first motional sidebands [16], we determine typical mean vibrational quantum numbers after Doppler cooling $(\bar{n}_x, \bar{n}_y, \bar{n}_z) = (20 \pm 5, 4 \pm 1, 6 \pm 1)$. From these mean phonon numbers and the secular frequencies given in Sect. 2.1 we calculate a rms extension of the ion’s motional wave packet of (25 ± 5) nm in the direction of the cavity axis, much smaller than the wavelength of 729 nm. At the end of the cooling sequence the ion is optically pumped into the $S_{1/2}$ ($m = -1/2$) Zeeman sub-level

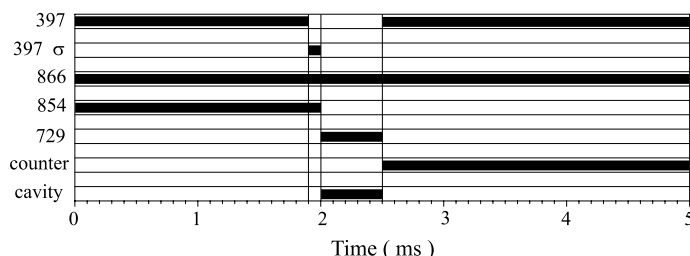


FIGURE 5 Example of a 5-ms pulse sequence. In the first 2 ms a defined ‘starting’ state is prepared. Then this state is manipulated (2 ms to 2.5 ms). Finally the outcome is detected (excitation or not) for the remaining time. The 10-ms and 20-ms pulse sequences differ only in a longer manipulation window (up to 3 ms) and a longer detection time

by applying a 0.1-ms σ^- -polarized pulse at 397 nm. After that, all light at 397 nm is switched off.

Second, the ion is excited on the $S_{1/2} \leftrightarrow D_{5/2}$ ($m = -1/2$ to $m' = -5/2$) transition by a free laser beam or by light resonant in the trap cavity. A time window of 0.5 to 3 ms is assigned to this process. Interaction of the ion and light within the trap cavity can be achieved by either frequency locking the cavity to the quadrupole transition or by a cavity scanning technique. In the first case we inject short resonant laser pulses with variable pulse length into the frequency-stabilized cavity in order to study coherent ion–field interaction. The second technique is used for investigating the ion’s response to dynamical or spatial variations of the intracavity field. Here, the laser at 729 nm is set to a fixed detuning Δ from the $S_{1/2} \leftrightarrow D_{5/2}$ transition. We inject the laser beam into the cavity TEM₀₀ mode (cf. Fig. 4) and apply a voltage ramp to the scan PZT in order to scan the cavity length. When the cavity reaches resonance with the laser frequency it fills with light and may excite the ion to the $D_{5/2}$ level. Then the light at 729 nm is switched off and the cavity mirror is ramped down to its initial position.

Third, we determine the excitation probability via the electron-shelving technique. The blue light at 397 nm is switched on (866-nm light is on anyway) and the fluorescence is counted by the PMT for a time interval between 2.3 ms and 17 ms depending on the duration of the total pulse sequence (5, 10 or 20 ms). The PMT count rate for the fluorescent ion is ≈ 16 kHz; the signal-to-background ratio ~ 10 . By comparing the number of counts in the time interval with a threshold we can discriminate with very high probability ($> 99\%$) [16] whether excitation happened (electron shelved in $D_{5/2}$, no fluorescence) or the ion remains in the ground state (fluorescence). Note that although state detection happens a few ms after the ion–light interaction the ion’s state is well preserved due to the long lifetime (1 s) of the $D_{5/2}$ level.

All three steps are typically repeated 100 times to yield the average excitation probability. After that, changes in the excitation window may be applied, such as a change in the laser frequency (frequency scan) or a change in the excitation pulse length (pulse-length scan). For example, to obtain an excitation spectrum, the 729-nm laser is tuned over the quadrupole transition in steps of 1 kHz.

3.2 Temporal variation of the intracavity field

In our first experiment we probe the ion’s response to temporal variations of the intracavity field by placing it close to a node of the SW field [24] and varying the cavity scan rate.

Figure 6 shows the excitation probability on the $S_{1/2} \leftrightarrow D_{5/2}$ transition for different scan rates. For negative (positive) scan rates the mirrors move towards each other (apart) and thereby Doppler shift the light to the blue (red). The atomic transition then seems to be red (blue)-shifted as the excitation laser detuning has to compensate for the Doppler shift. Increasing scan rate increases the shift from the line center (detuning zero), which is found by excitation with a free laser beam. In addition, faster scan rates broaden the line because more and more frequency components are added to the light confined in the cavity.

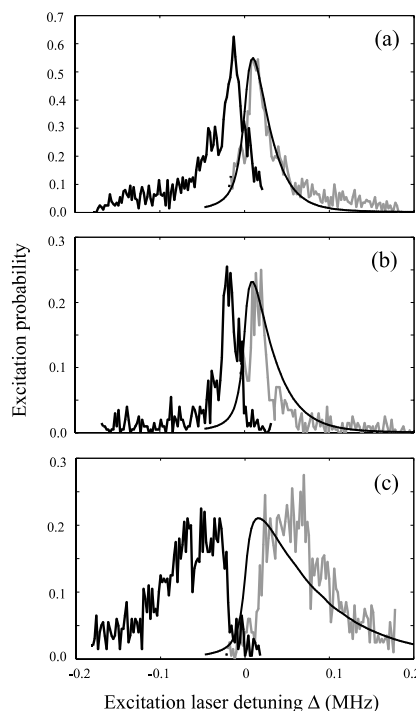


FIGURE 6 Excitation spectra for different cavity scan rates $v_L = \pm 0.16$ (a), ± 0.23 (b) and ± 0.69 (c). On the blue-shifted spectra (gray lines), theoretical simulations are superimposed (solid line). The parameters for the simulations are: laser bandwidth $\Delta\nu_{\text{laser}} = 6$ kHz, natural line width of the $S_{1/2} \leftrightarrow D_{5/2}$ transition $\Delta\nu_{\text{SD}} = 0.17$ Hz, Rabi frequency for zero detuning: $\Omega_0 = 15.5$ kHz (a), 11 kHz (b) and 25 kHz (c)

MUNDT et al. Coherent coupling of a single $^{40}\text{Ca}^+$ ion to a high-finesse optical cavity

To put these observations in a more quantitative form it is convenient to define a normalized scan rate $\nu_L = 2\mathcal{F}\omega_L\tau/(\pi c)$. It corresponds to the resonance frequency shift of the cavity in units of the HWHM cavity line width $c/(4L\mathcal{F})$ per cavity energy storage time $\tau = \mathcal{F}L/(\pi c)$. To model the coupling dynamics we first have to know the electric field acting on the ion. The electric field amplitude E_{cav} in a cavity swept over resonance is a solution of the differential equation [22, 23]:

$$\frac{dE_{\text{cav}}}{d\bar{t}} = -(1 - i\nu_L\bar{t})E_{\text{cav}} + i\frac{\sqrt{T}\mathcal{F}}{\pi}E_0,$$

where $\bar{t} = t/\tau$, $T \approx \pi/\mathcal{F}$ is the transmission of the input coupling mirror and E_0 is the amplitude of the input field. For slow scan rates ($\nu_L \ll 1$) we obtain the quasi-static case, whereas for fast scan rates ($\nu_L \gg 1$) the incoming light interferes with the light stored in the cavity. Figure 7 shows the normalized intracavity field amplitude for three different scan rates.

The interaction of this time-dependent electric field with the ion can now be modeled by numerically integrating the Bloch equations for a two-level system. The result for a scan rate of $\nu_L = 1$ and a typical laser intensity is shown in Fig. 8. The electronic transition (Fig. 8, top) is blue-shifted and broadened compared to the excitation with a free laser beam, as expected.

Figure 8 (bottom) illustrates, for five different detunings Δ , the time evolution of the excitation to the $D_{5/2}$ level as the cavity is swept over resonance. For all detunings, the excitation probability shows a steep rising edge at the moment the cavity fills with light and subsequent Rabi oscillations with a damping depending on excitation power and detuning. This excitation characteristic remains qualitatively unchanged over a large range of excitation powers and scan rates. The final stationary values of the excitation probabilities are taken to compose the excitation spectrum (Fig. 8, top).

The results of the theoretical simulation for positive scan rates are shown as solid lines superimposed on the blue-shifted spectra in Fig. 6. The calculated and experimental spectra show good agreement for small scan rates (Fig. 6a,b).

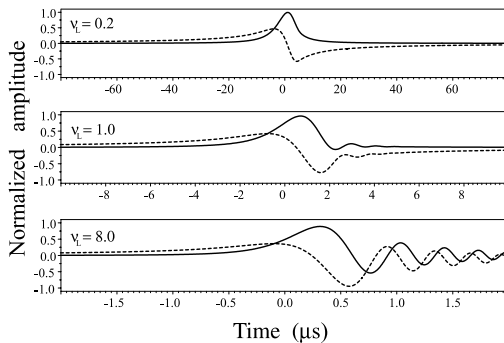


FIGURE 7 Calculated time-dependent normalized electric field amplitude in the cavity for three different scan rates ν_L . The *solid line* is the real part; the *dashed line* the imaginary part of the electric field amplitude. For large scan rates the interference of incoming and stored light becomes visible

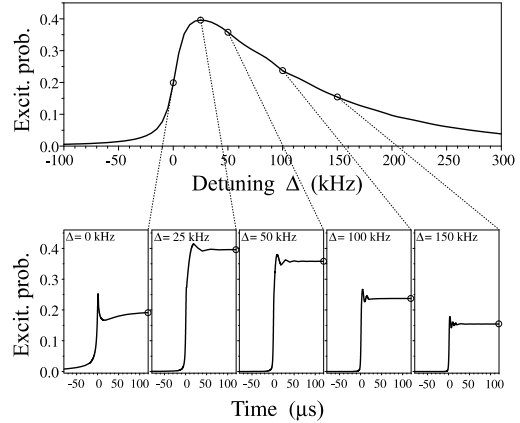


FIGURE 8 Simulated excitation spectrum for $\nu_L = 1$ (top) and time evolution of the excitation probability for different detunings Δ (bottom). More details are given in the text

For larger scan rates (Fig. 6c) the centers of the spectra are slightly shifted. We assume that this shift is caused by nonlinearities and hysteresis effects of the PZT motion. Although we kept the excitation power constant in the experiments, we left the Rabi frequency Ω_0 as a fitting parameter to account for variations in excitation due to thermal drift of the cavity shifting the node of the SW away from the ion's position.

The investigation and theoretical understanding of the ion–cavity field coupling dynamics as discussed above are important for realization of the atom–photon interface in quantum networks. The experimental implementation of such a scheme requires control over the shape of the light pulse emitted from the cavity and thus control over the dynamic atom–cavity coupling [4].

3.3 Spatial variation of the intracavity field

The trapped single ion is confined to a region in space of less than 30 nm, which is much less than the excitation wavelength (729 nm). It thus can be used as a nanoscopic probe of the SW field spatial variation as first shown in [6, 25]. To probe this spatial variation, we again use the cavity scanning technique and leave the scan rate fixed at a small value, allowing for stable scans with only a little perturbation of the excitation spectrum as in Fig. 6a. The laser is scanned over the quadrupole transition in steps of ~ 1 kHz to obtain an excitation spectrum at a certain position in the SW. To use the excitation probability as a measure of the field intensity, it is important to adjust the laser power such that the excitation is kept well below saturation at all positions in the SW. The offset voltage of both scan PZT and offset PZT is then varied simultaneously in such a way that the SW in the cavity is shifted longitudinally with respect to the location of the ion. Repetition of the procedure yields a number of excitation spectra shown in Fig. 9. The position-dependent excitation probability is determined by fitting each excitation spectrum with a Lorentzian and adopting the peak value. Figure 10 displays these values as a function of the PZT offset voltage.

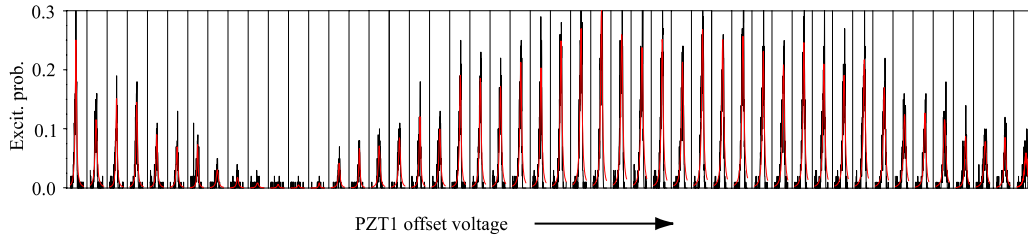


FIGURE 9 All 48 excitation spectra measured at different positions in the intracavity SW. Every box (width: 600 kHz) contains a spectral line as in Fig. 6; the offset voltage increases from *left to right*. The SW pattern is already visible; the total shift is ~ 1.5 half-waves

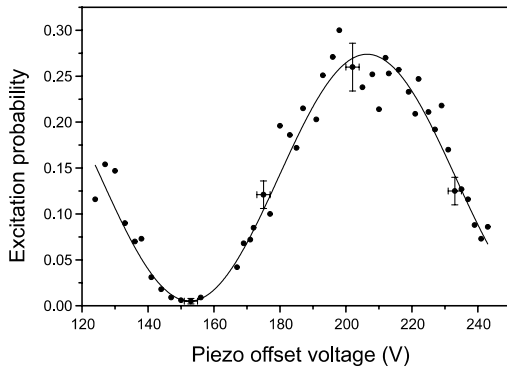


FIGURE 10 Excitation probability on the $S_{1/2} \leftrightarrow D_{5/2}$ transition of a single trapped Ca^{+} ion as a function of the PZT offset voltage, i.e. at various positions in the intracavity standing wave field. The *solid line* represents a \sin^2 function fitted to the data points

Error bars given for representative data points in Fig. 10 are due to PZT hysteresis (abscissa) and the errors of the fits to the excitation spectra (ordinate). The excitation probability varies spatially with the intensity of the SW [24]. A theoretical Bloch-equation analysis as described above predicts a nearly pure \sin^2 spatial variation, deviating by less than 1%. From a \sin^2 fit to the data points we obtain the contrast ratio (visibility V) of the position-dependent excitation, $V = 96.3 \pm 2.6\%$. This very high visibility results from the strong confinement of the ion's wavefunction. The laser-cooled ion, oscillating with its secular frequencies and with thermally distributed amplitudes, has a rms spatial extension along the cavity axis of a_c . This extension leads to a reduction of the excitation contrast by a factor of $\exp(-2(2\pi a_c/\lambda)^2)$ compared to the excitation contrast experienced by a point-like atom at rest. From the measured visibility V we find $a_c = 16_{-7}^{+5}$ nm. The small value of the extension a_c shows that in this experiment we cool the ion close to the Doppler limit (13 nm).

A necessary condition for all experiments relying on ion-cavity mode coupling is the ability to place the ion at a certain position of the intracavity SW field with high precision and high reproducibility [6]. In our experiment, the precision of positioning the center of the ion's wavefunction, using a measurement as in Fig. 10, is limited by the uncertainty in the measured excitation probability. This uncertainty is due to a statistical error, i.e. the finite number of state-detection

measurements, and systematic errors such as fluctuations of laser intensity and wavelength, drift and jitter of the scan PZT, etc. [25]. From the uncertainties in excitation probability (error bars in Fig. 10) we deduce a spatial precision between 7 nm ($\approx \lambda/100$) at the position of largest slope and 12 nm and 36 nm at minimum or maximum excitation, respectively. We note, however, that the precision can be enhanced by averaging over a larger number of state-detection measurements.

3.4 Coupling of motional states

Many schemes for quantum information processing with trapped ions rely on coherent interaction not only with the internal state but also with the motional degrees of freedom. A controlled coupling of atomic states dressed by vibrational modes to the cavity field is a precondition for realizing such schemes.

If one compares carrier (no change of vibrational quantum number, $\Delta n = 0$) and first vibrational sideband ($\Delta n = -1$) transition probabilities in a SW, both show a position-dependent coupling due to the SW pattern as shown in Sect. 3.3. But where the coupling to the carrier is strongest, no coupling to the first (i.e. all odd) sidebands occurs and vice versa, i.e. carrier and odd sideband excitations map the SW spatial field variation, but the traces are shifted by a phase factor of π . This phase shift arises due to symmetry characteristics of the transition matrix elements of carrier and sideband transitions in a SW field [1, 12]: the spatial part of the quadrupole transition matrix element is proportional to $\langle n' | \exp(ikx) | n \rangle$ for a traveling wave (TW) and $\langle n' | \cos(kx) | n \rangle$ for a SW with the electric field $E \propto \sin(kx)$ [24]. Here n and n' are the vibrational quantum numbers in the $S_{1/2}$ and $D_{5/2}$ levels, respectively, k is the wavenumber and x is the ion's position in the field. For a TW, all vibrational states (n, n') can be coupled since $\exp(ikx)$ contains even and odd powers of kx [26]. In contrast, for a SW $\langle n' | \cos(kx) | n \rangle$ has to be expanded into even or odd powers of kx depending on the ion's position, e.g. $x = 0$ close to a node or $x = \lambda/4$ close to an anti-node. Thus, transitions changing the phonon number by even or odd integers can only be excited at different positions in the SW. The first-sideband transition ($\Delta n = \pm 1$) couples maximally at anti-nodes of the SW, whereas the carrier transition ($\Delta n = 0$) couples maximally at nodes. In order to demonstrate this motion-dependent coupling, we recorded excitation probabilities of the ion at a fixed cavity scan rate ($v_L = -0.23$), for different positions within the SW, and with the laser at 729 nm now tuned to either the carrier or the red axial side-

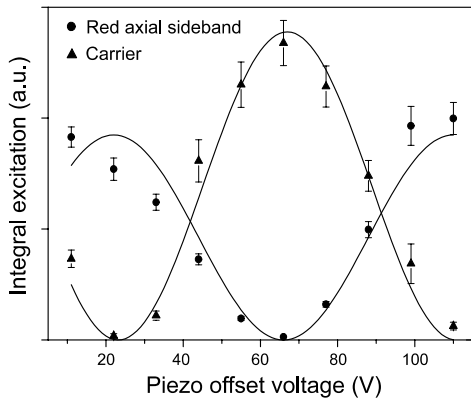
MUNDT et al. Coherent coupling of a single $^{40}\text{Ca}^+$ ion to a high-finesse optical cavity

FIGURE 11 Integral excitation on the carrier (triangles) and the red axial sideband (circles) of the $S_{1/2} \leftrightarrow D_{5/2}$ transition as a function of the PZT offset voltage, i.e. at various positions in the intracavity standing wave field. The solid lines represent fits of \sin^2 functions to the data points

band ($\Delta n = -1$, laser-detuned by $-\omega_z$) of the $S_{1/2} \leftrightarrow D_{5/2}$ transition. In both cases, the intensity of the laser was adjusted such that the excitations of carrier and sideband were comparable and were kept well below saturation. In this experiment we determine the integral excitation, i.e. the area of the respective excitation spectra, as the spectra show an asymmetric line shape (cf. Fig. 6b,c). The high-contrast orthogonal coupling of carrier and sideband transitions to the cavity mode is demonstrated in Fig. 11.

This coupling facilitates applications such as cavity-assisted cooling in a SW [12], the Cirac–Zoller quantum-computing scheme [27] and entanglement of motional and photonic states when coupling to the cavity vacuum field [17, 18]. In particular, cavity-assisted cooling in a SW field means that sideband cooling [16] on a red-detuned vibrational sideband is facilitated by suppression of off-resonant carrier transitions which induce motional heating. In a similar fashion, unwanted off-resonant carrier excitations are suppressed when driving sideband transitions in the Cirac–Zoller quantum-computing scheme. Here, off-resonant carrier excitations impose a limit on the attainable gate speed [28]. As electronic excitation probabilities of the ion depend on both the vibrational state and the position within the cavity field, the internal electronic degrees of freedom are coupled to both the (in general: quantized) single-mode cavity field and the vibrational degrees of freedom. This coupling allows e.g. for generation of an entangled state of a subsystem that can store quantum information (vibration, electronic states) with a subsystem that can be used for propagation of quantum information (light).

3.5 Coherent ion-cavity coupling

The application of the ion–cavity coupling for implementation of quantum network schemes requires a controlled *coherent* interaction. To demonstrate such coherent coupling to the cavity field we stabilize the trap cavity to the $S_{1/2} \leftrightarrow D_{5/2}$ carrier transition frequency as described in

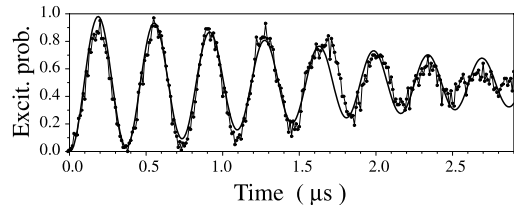


FIGURE 12 Rabi oscillations driven by the light field in the stabilized cavity. The parameters for the theoretical simulation are: Rabi frequency $\Omega_0 = 8.95$ MHz, $\eta^2 \bar{n} = 0.049$ and laser detuning $\Delta = 0$

Sect. 2.2. We excite the ion with resonant laser pulses of different pulse lengths injected into the trap cavity. Starting from a pulse length of zero up to a pulse of 3- μs duration we determine the average excitation probability from 100 experiments per pulse length. The resulting coherent dynamics (Rabi oscillations) are shown in Fig. 12 together with a numerical simulation (solid line). The theoretical curve is calculated assuming a thermal distribution over harmonic oscillator states $|n\rangle$. The Rabi frequency of any particular $|S, n\rangle \leftrightarrow |D, n\rangle$ transition depends on $n\eta^2$, where η is the Lamb–Dicke parameter. The thermal mixture of different oscillation frequencies washes out the Rabi oscillations, which therefore appear damped.

4 Summary and outlook

In summary, we have demonstrated coherent coupling of electronic and motional states of a single trapped ion to a single field mode of a high-finesse cavity. The position of the ion within the standing wave can be determined with a precision of up to $\lambda/100$. As the electronic quadrupole transition in Ca^+ is one of the candidates for implementing a quantum bit, our experiments are a key step towards realization of quantum computing and communication schemes with trapped ions that require a controlled coherent interaction of ion and cavity field. Future experiments aim at demonstrating and utilizing cavity-modified spontaneous emission for applications such as triggered single-photon emission and realization of the atom–photon interface. Another route is the extension of the current configuration towards trapping of two or more ions coupled to a common cavity mode, thus allowing for implementation of quantum logical gate operations.

ACKNOWLEDGEMENTS This work is supported by the Austrian ‘Fonds zur Förderung der wissenschaftlichen Forschung’ (SFB15), by the European Commission (TMR networks ‘QI’ and ‘QSTRUCT’ (ERB-FRMX-CT96-0087 and -0077), IHP network ‘QUEST’ (HPRN-CT-2000-00121) and IST/FET program ‘QUBITS’ (IST-1999-13021)) and by the ‘Institut für Quanteninformation GmbH’. C.R. acknowledges support by Fundação para a Ciência e a Tecnologia (Portugal) under the grant SFRH/BD/6208/2001.

REFERENCES

- 1 M. Šašura, V. Bužek: J. Mod. Opt. **49**, 1593 (2002)
- 2 W. Paul: Rev. Mod. Phys. **62**, 531 (1990)
- 3 H.C. Nägerl, Ch. Roos, D. Leibfried, H. Rohde, G. Thalhammer, J. Eschner, F. Schmidt-Kaler, R. Blatt: Phys. Rev. A **61**, 023405 (2000)

-
- 4 J.I. Cirac, P. Zoller, H.J. Kimble, H. Mabuchi: Phys. Rev. Lett. **78**, 3221 (1997)
- 5 A.B. Mundt, A. Kreuter, C. Becher, D. Leibfried, J. Eschner, F. Schmidt-Kaler, R. Blatt: Phys. Rev. Lett. **89**, 103001 (2002)
- 6 G.R. Guthöhrlein, M. Keller, K. Hayasaka, W. Lange, H. Walther: Nature **414**, 49 (2001)
- 7 C.K. Law, H.J. Kimble: J. Mod. Opt. **44**, 2067 (1997)
- 8 A. Kuhn, M. Hennrich, G. Rempe: Phys. Rev. Lett. **89**, 067901 (2002)
- 9 K.M. Gheri, C. Saavedra, P. Törmä, J.I. Cirac, P. Zoller: Phys. Rev. A **58**, R2627 (1998)
- 10 N. Lütkenhaus: Phys. Rev. A **61**, 052304 (2000)
- 11 E. Knill, R. Laflamme, G.J. Milburn: Nature **409**, 46 (2001)
- 12 J.I. Cirac, R. Blatt, P. Zoller, W.D. Phillips: Phys. Rev. A **46**, 2668 (1992)
- 13 E.M. Purcell: Phys. Rev. **69**, 681 (1946)
- 14 J.I. Cirac, M. Lewenstein, P. Zoller: Phys. Rev. A **51**, 1650 (1995)
- 15 D.M. Meekhof, C. Monroe, B.E. King, W.M. Itano, D.J. Wineland: Phys. Rev. Lett. **76**, 1796 (1996)
- 16 Ch. Roos, Th. Zeiger, H. Rohde, H.C. Nägerl, J. Eschner, D. Leibfried, F. Schmidt-Kaler, R. Blatt: Phys. Rev. Lett. **83**, 4713 (1999)
- 17 V. Bužek, G. Drobný, M.S. Kim, G. Adam, P.L. Knight: Phys. Rev. A **56**, 2352 (1997)
- 18 F.L. Semião, A. Vidiella-Barranco, J.A. Roversi: Phys. Rev. A **64**, 024305 (2001)
- 19 H. Dehmelt: Bull. Am. Phys. Soc. **20**, 60 (1975)
- 20 S. Gulde, D. Rotter, P. Barton, F. Schmidt-Kaler, R. Blatt, W. Hogervorst: Appl. Phys. B **73**, 861 (2001)
- 21 R.W. Drever, J.L. Hall, F.V. Kowalski, J. Hough, G.M. Ford, A. Munley, H. Ward: Appl. Phys. B **31**, 97 (1983)
- 22 H. Rohde, J. Eschner, F. Schmidt-Kaler, R. Blatt: J. Opt. Soc. Am. B **19**, 1425 (2002)
- 23 M.J. Lawrence, B. Willke, M.E. Husman, E.K. Gustafson, R.L. Byer: J. Opt. Soc. Am. B **16**, 523 (1999)
- 24 Note that the atomic quadrupole moment couples to the gradient of the electric field. The maximum excitation thus occurs at the nodes of the standing wave
- 25 J. Eschner, C. Raab, F. Schmidt-Kaler, R. Blatt: Nature **413**, 495 (2001)
- 26 Note that $kx = \eta(a + a^\dagger)$, for the ion oscillating around $x = 0$, where η is the Lamb-Dicke parameter and a^\dagger and a are the phonon creation and annihilation operators, respectively
- 27 J.I. Cirac, P. Zoller: Phys. Rev. Lett. **74**, 4091 (1995)
- 28 A. Steane, C.F. Roos, D. Stevens, A. Mundt, D. Leibfried, F. Schmidt-Kaler, R. Blatt: Phys. Rev. A **62**, 042305 (2000)

Bibliography

- [1] E. T. Jaynes, and F. W. Cummings, IEEE J. Quant. Elec. **51**, 89 (1963)
- [2] P. Stehle, Phys. Rev. A **2**, 102 (1970)
- [3] G. Barton, Proc. Royal Soc. London A **320**, 251 (1970)
- [4] D. P. DiVincenzo, Fortschritte der Physik **48**, special issue, Eds. H.–K. Lo and S. Braunstein 771 (2000)
- [5] H. C. Nägerl, W. Bechter, J. Eschner, F. Schmidt–Kaler, and R. Blatt, Appl. Phys. B **66**, 603 (1998)
- [6] H. C. Nägerl, Ch. Roos, D. Leibfried, H. Rohde, G. Thalhammer, J. Eschner, F. Schmidt–Kaler, R. Blatt, Phys. Rev. A **61**, 023405 (2000)
- [7] J. I. Cirac, P. Zoller, H. J. Kimble, and H. Mabuchi, Phys. Rev. Lett. **78**, 3221 (1997)
- [8] J. Bolle, Ph. D. thesis, Universität Innsbruck (1998)
- [9] H. C. Nägerl, Ph. D. thesis, Universität Innsbruck (1998)
- [10] C. F. Roos, Ph. D. thesis, Universität Innsbruck (2000)
- [11] H. F. Rohde, Ph. D. thesis, Universität Innsbruck (2001)
- [12] C. Raab, Ph. D. thesis, Universität Innsbruck (2001)
- [13] M. Šašura, and V. Bužek, J. Mod. Opt. **49**, 1593 (2002)
- [14] P. Meystre, and M. Sargent III, Elements of quantum optics, Springer University Press, third edition (1998)
- [15] D. F. V. James, Appl. Phys. B **66**, 181 (1998)

- [16] R. D. Cowan, *The theory of atomic structure and spectra*, University of California Press (1981)
- [17] V. Weisskopf, and E. Wigner *Z. Phys.* **63**, 54 (1930)
- [18] H. J. Carmichael, R. J. Brecha, M. G. Raizen, H. J. Kimble, and P. R. Rice, *Phys. Rev. A* **40**, 5516 (1989)
- [19] E. M. Purcell, *Phys. Rev.* **69**, 681 (1946)
- [20] Q. A. Turchette, R. J. Thompson, and H. J. Kimble, *Appl. Phys. B* **60**, 1 (1995)
- [21] H. B. G. Casimir, and D. Polder, *Phys. Rev.* **73**, 360 (1948)
- [22] K. H. Drexhage in *Progress in Optics XII*, ed. E. Wolf North-Holland, Amsterdam (1974)
- [23] P. Goy, J. M. Raimond, M. Gross, and S. Haroche, *Phys. Rev. Lett.* **50**, 1903 (1983)
- [24] D. Kleppner, *Phys. Rev. Lett.* **47**, 233 (1981)
- [25] R. G. Hulet, E. S. Hilfer, and D. Kleppner, *Phys. Rev. Lett.* **55**, 2137 (1985)
- [26] W. Jhe, A. Anderson, E. A. Hinds, D. Meschede, L. Moi, and S. Haroche, *Phys. Rev. Lett.* **58**, 666 (1987)
- [27] G. Gabrielse, and H. Dehmelt, *Phys. Rev. Lett.* **55**, 67 (1985)
- [28] D. Meschede, H. Walther, and G. Müller, *Phys. Rev. Lett.* **54**, 551 (1985)
- [29] G. Rempe, H. Walther, N. Klein, *Phys. Rev. Lett.* **58**, 353 (1987)
- [30] F. Bernadot, P. Nussenzveig, M. Brune, J. M. Raimond, and S. Haroche, *Europhys. Lett.* **17**, 33 (1992)
- [31] D. J. Heinzen, J. J. Childs, J. E. Thomas, and M. S. Feld, *Phys. Rev. Lett.* **58**, 1320 (1987)
- [32] F. De Martini, G. Innocenti, G. R. Jacobovitz, and P. Mataloni, *Phys. Rev. Lett.* **59**, 2955 (1987)

- [33] W. P. Smith, J. E. Reiner, L. A. Orozco, S. Kuhr, and H. M. Wiseman
Phys. Rev. Lett. **89**, 133601 (2002)
- [34] P. Münsterman, T. Fischer, P. Maunz, P. W. H. Pinsky, and
G. Rempe, Phys. Rev. Lett. **82**, 3791 (1999)
- [35] P. W. H. Pinkse, T. Fischer, P. Maunz, and G. Rempe,
Nature **404**, 365 (2000)
- [36] A. Kuhn, M. Hennrich and G. Rempe
Phys. Rev. Lett. **89**, 067901 (2002)
- [37] R. J. Thompson, G. Rempe, and H. J. Kimble,
Phys. Rev. Lett. **68**, 1132 (1992)
- [38] C. J. Hood, T. W. Lynn, A. C. Doherty, A. S. Parkins, and
H. J. Kimble, Science **287**, 1457 (2000)
- [39] K. An, J. J. Childs, R. R. Dasari, and M. S. Feld,
Phys. Rev. Lett. **80**, 4157 (1994)
- [40] E. Yablonovitch, T. J. Gmitter, and R. Bhat,
Phys. Rev. Lett. **61**, 2546 (1988)
- [41] C. Weisbuch, M. Nishioka, A. Ishikawa, and Y. Arakawa
Phys. Rev. Lett. **69**, 3314 (1992)
- [42] J. M. Gérard, B. Sermage, B. Gayral, B. Legrand, E. Costard, and
V. Thierry-Mieg, Phys. Rev. Lett. **81**, 1110 (1998)
- [43] A. Kiraz, P. Michler, C. Becher, B. Gayral, A. Imamoglu, L. Zhang,
E. Hu, W. V. Schoenfeld, and P. M. Petroff,
Appl. Phys. Lett. **78**, 3932 (2001)
- [44] C. Becher, A. Kiraz, P. Michler, A. Imamolu, W. V. Schoenfeld,
P. M. Petroff, L. Zhang, and E. Hu,
Phys. Rev. B **63**, 121312(R) (2001)
- [45] G. S. Solomon, M. Pelton, and Y. Yamamoto,
Phys. Rev. Lett. **86**, 3903 (2001)
- [46] T. D. Happ, I. I. Tartakovskii, V. D. Kulakovskii, J.-P. Reithmaier,
M. Kamp, and A. Forchel, Phys. Rev. B **66**, 041303(R) (2002)
- [47] P. Münstermann, T. Fischer, P. W. H. Pinkse, and G. Rempe,
Opt. Comm. **159**, 63 (1999)

- [48] C. Cohen–Tannoudji, B. Diu, and F. Laloë, Quantum mechanics, volume 2. John Wiley & Sons (1977)
- [49] W. Paul, O. Osberghaus, and E. Fischer, Forschungsberichte des Wirtschafts– und Verkehrsministeriums Nordrhein–Westfalen 415, Westfälischer Verlag (1958)
- [50] P. K. Ghosh, Ion Traps, Clarendon Press (1995)
- [51] W. Paul, Rev. Mod. Phys. **62**, 531 (1990)
- [52] M. Combescure, Ann. Inst. Henri Poincaré **44** (3), 293 (1986)
- [53] L. S. Brown, Phys. Rev. Lett. **66**, 527 (1991)
- [54] A. E. Siegman, Lasers, University Science Books, Mill Valley, California (1986)
- [55] C. J. Hood, H. J. Kimble, and J. Ye, Phys. Rev. A **64**, 033804 (2001)
- [56] G. R. Guthöhrlein, M. Keller, K. Hayasaka, W. Lange, and H. Walther, Nature **414**, 49 (2001)
- [57] W. Bechter, Diploma–thesis, Universität Innsbruck (1998)
- [58] G. Thalhammer, Diploma–thesis, Universität Innsbruck (1999)
- [59] R. W. Drever, J. L. Hall, F. V. Kowalski, J. Hough, G. M. Ford, A. Munley, and H. Ward, Appl. Phys. B **31**, 97 (1983)
- [60] G. Blasbichler, Diploma–thesis, Universität Innsbruck (2000)
- [61] Ch. Roos, Th. Zeiger, H. Rohde, H. C. Nägerl, J. Eschner, D. Leibfried, F. Schmidt–Kaler, and R. Blatt, Phys. Rev. Lett. **83**, 4713 (1999)
- [62] C. E. Wieman and L. Hollberg, Rev. Sci. Instr. **62**, 1 (1991)
- [63] L. Ricci, M. Weidemüller, T. Esslinger, A. Hemmerich, C. Zimmermann, V. Vuletic, W. König, and T. W. Hänsch, Opt. Comm. **117**, 541 (1995)
- [64] S. Gulde, D. Rotter, P. Barton, F. Schmidt–Kaler, R. Blatt, Appl. Phys. B **73**, 861 (2001)
- [65] W. W. Macalpine, R. O. Schildknecht, Proc. IRE **47**, 2099 (1959)

- [66] H. Rhode, J. Eschner, F. Schmidt–Kaler, R. Blatt,
J. Opt. Soc. Am. B **19**, 1425 (2002)
- [67] M. J. Lawrence, B. Willke, M. E. Husman, E. K. Gustafson, and
R. L. Byer, J. Opt. Soc. Am. B **16**, 523 (1999)
- [68] R. Loudon, The quantum theory of light, Oxford University Press,
second edition (1983)
- [69] J. Eschner, Eur. Phys. J. D (2002)
DOI: 10.1140/epjd/e2002-00235-7
- [70] J. Eschner, Ch. Raab, F. Schmidt–Kaler, and R. Blatt,
Nature **413**, 495 (2001)
- [71] J. I. Cirac, R. Blatt, P. Zoller, and W. D. Phillips,
Phys. Rev. A **46**, 2668 (1992)
- [72] J. I. Cirac, and P. Zoller, Phys. Rev. Lett. **74**, 4091 (1995)
- [73] V. Bužek, G. Drobný, M. S. Kim, G. Adam, and P. L. Knight,
Phys. Rev. A **56**, 2352 (1997)
- [74] F. L. Semião, A. Vidiella–Barranco, and J. A. Roversi,
Phys. Rev. A **64**, 024305 (2001)
- [75] A. Steane, C. F. Roos, D. Stevens, A. Mundt, D. Leibfried,
F. Schmidt–Kaler, and R. Blatt, Phys. Rev. A **62**, 042305 (2000)
- [76] A. Kreuter, Ph. D. thesis, Universität Innsbruck, in preparation